Eidgenössische Technische Hochschule Zürich

Master's Thesis

CFD Simulation of Single Phase Mixing in a 4x4 Rod Bundle with Different Spacers

Lluís Santolaria Pérez

Professor: Prof. Dr. Horst-Michael Prasser
Supervisor: Ms. Xiaorong Li

September 2018

This page is intentionally left blank.

ETH

Eidgenössische Technische Hochschule Zürich
Swiss Federal Institute of Technology Zurich

Declaration of originality

The signed declaration of originality is a component of every semester paper, Bachelor's thesis, Master's thesis and any other degree paper undertaken during the course of studies, including the respective electronic versions.

Lecturers may also require a declaration of originality for other written papers compiled for their courses.

I hereby confirm that I am the sole author of the written work here enclosed and that I have compiled it in my own words. Parts excepted are corrections of form and content by the supervisor.

Title of work (in block letters):

CFD SIMULATION OF SINGLE PHASE MIXING IN A 4x4 ROD BUNDLE WITH DIFFERENT SPACERS

Authored by (in block letters):

For papers written by groups the names of all authors are required.

Name(s):	**First name(s):**
LLUÍS	SANTOLARIA PÉREZ

With my signature I confirm that

- I have committed none of the forms of plagiarism described in the 'Citation etiquette' information sheet.
- I have documented all methods, data and processes truthfully.
- I have not manipulated any data.
- I have mentioned all persons who were significant facilitators of the work.

I am aware that the work may be screened electronically for plagiarism.

Place, date	**Signature(s)**
Zürich, 21.09.2018	

For papers written by groups the names of all authors are required. Their signatures collectively guarantee the entire content of the written paper.

This page is intentionally left blank.

Acknowledgements

I would like to thank Ms. Xiaorong Li and Prof. Dr. Horst-Michael Prasser for giving me the opportunity to work with them in the Laboratory of Nuclear Energy Systems. Ms. Li accompanied me during the whole project and she was always there when I needed her help, offering interesting comments and guiding me towards the right direction.

I would also like to thank the rest of Ph.D. students in the lab, who were there during the group meetings, and helped me by asking questions and suggesting different approaches to the problem.

Besides, I would like to highlight the efforts made by the mobility departments in both my home university, UPC Barcelona Tech - ETSEIB, and ETH Zürich for making this exchange programme possible.

Last but not least, to my parents, who have always desired the best for me and have helped me achieve it with their support, patience and understanding throughout my years of study.

This page is intentionally left blank.

Abstract

Enhancing heat transfer between fuel rods and coolant is one of the main goals of nuclear engineering. Spacer grids equipped with mixing vanes are placed inside nuclear fuel assemblies to enhance the lateral velocities of the flow inside the sub-channels and, also, increase the lateral mixing between different sub-channels and, consequently, the heat transfer.

For the design and analysis of these spacer grids, Computational Fluid Dynamics (CFD) tools, able to compute flow structures taking into account effects such as wall friction, turbulent mixing or heat transfer, are commonly used. In this project, CFD methodologies have been developed to simulate flow field inside bare rod bundle and bundles equipped with 4 types of spacers, testing different mesh strategies and turbulence models.

Behaviour of different methodologies are studied and results are compared against experimental data, and promising options are identified.

This page is intentionally left blank.

Contents

1 Introduction **1**
- 1.1 Swiss electrical energy system . . . 2
  - 1.1.1 Swiss Energy Policy 2050 . . . 5
- 1.2 Nuclear Power Plants . . . 5
  - 1.2.1 Types of nuclear power plants . . . 8
  - 1.2.2 Pressurized Water Reactors . . . 11
- 1.3 What to expect from this project . . . 14
  - 1.3.1 PSI Experimentation . . . 14
  - 1.3.2 CFD model creation importance . . . 14

2 State of the art **15**
- 2.1 Previous work . . . 15
- 2.2 Current work . . . 17

3 Theoretical background **18**
- 3.1 Mathematical model of the flow . . . 18
- 3.2 Numerical methods . . . 19
  - 3.2.1 Direct Numerical Simulation . . . 19
  - 3.2.2 Large Eddy Simulation . . . 20
  - 3.2.3 Reynolds Averaged Navier-Stokes . . . 21

4 CFD Model **26**
- 4.1 Geometry . . . 26
- 4.2 Bare bundle case . . . 27
  - 4.2.1 Physical models - Boundary conditions . . . 27
  - 4.2.2 Mesh sensitivity analysis . . . 28
  - 4.2.3 Turbulence models analysis . . . 30
  - 4.2.4 Conclusions . . . 31
- 4.3 Spacer-vane case . . . 31
  - 4.3.1 Physical models - Boundary conditions . . . 31
  - 4.3.2 Mesh sensitivity analysis . . . 32
  - 4.3.3 Turbulence model analysis . . . 40
  - 4.3.4 Conclusions . . . 56
- 4.4 Different spacer grids . . . 57
  - 4.4.1 Spacer 1 - Standard 30° . . . 57
  - 4.4.2 Spacer 2 - Alternate 30° . . . 62
  - 4.4.3 Spacer 3 - Standard 15° . . . 67
  - 4.4.4 Spacer 4 - Alternate 15° . . . 72

5 Summary and outlook **77**

Appendix A Extra figures **79**
A.1 Trimmed mesh study - 2^{nd} part 80
A.2 Polyhedral mesh study - 2^{nd} part 83
A.3 Polyhedral mesh study - 3^{rd} part 86
A.4 Turbulence analysis 92

References **98**

Chapter 1

Introduction

Nowadays, it is very difficult to think of a life in which electricity is not present. From the moment the day starts until it ends, many devices and services that need electricity to work are used: household appliances, lights, trains or subways, smartphones, computers...

It is a fact that, year by year, the total amount of electrical energy produced worldwide is growing, and this tendency is not expected to change during the next decade. Among the different reasons for this, two of them are highlighted.

Population growth

The increasing world population is one of the biggest challenges in the modern era. Every year, the world population grows around 83 million people, approximately 1% of the total. This fact requires a redistribution of the limited resources present in our planet, as well as a resizing of urban nucleus, transport nets and electrical energy generation systems in order to satisfy the demands of the growing population, which is many times not done in an optimal way.

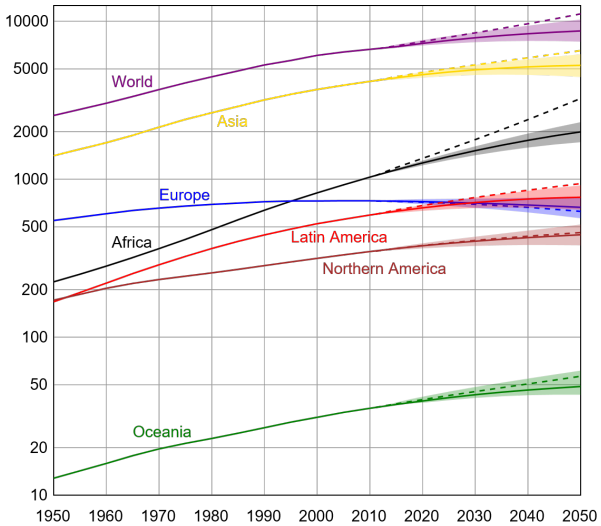

Figure 1.1: Estimates of population evolution in different continents, in millions of people. Source: United Nations, 2011 [1].

Exponential industrialization of developing countries

Globalization is formally defined as an interaction and integration process among people, companies and governments of different nations, driven by international trade and investment, and supported by information technology, which has effects on the environment, culture, political systems, economic development, prosperity and human physical well-being in societies around the world.

Although globalization has been present in the world for many centuries, advances in transport and information technology have increased its effect for the last decades, helping developing countries to grow very fast, especially in terms of the secondary sector, accentuated by industrial relocation.

This increasing industrial activity needs a growing electrical energy generation system to keep working, hence these developing countries are required to expand their generation systems. However, many times those countries lack of good conditions to use renewable energies, or are unable to face the huge investments to support them. Therefore, coal or gas power plants are generally built.

This is a problem for the modern world since, right now, most of the countries release huge amounts of CO_2 to the atmosphere as a consequence of the electricity production, causing a global health issue to the population and also increasing the greenhouse effect.

During the last decades, many energy policies have been approved to reduce the contaminant emissions, from the Kyoto Protocol in 1997, which limit the emissions to values slightly smaller than the 1990s, to the European pact celebrated in Bonn (Germany) in November 2017, to progressively close the coal power plants present in Europe.

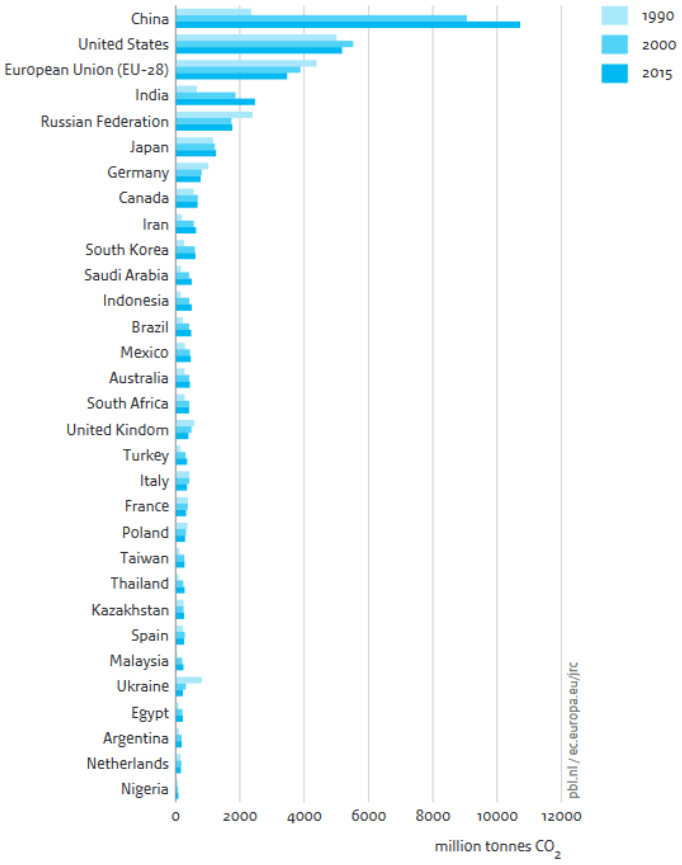

Figure 1.2: CO_2 emissions per country from fossil-fuel use and cement production. Source: EDGAR FT 2015 [2].

Those international agreements open the door to a great engineering challenge, consisting in redoing the electrical energy generation systems of those countries to make the world a healthier place to live in.

1.1 Swiss electrical energy system

Switzerland is a very special country for many reasons, and its electrical energy system is one of them. Its complex orography, with high mountains, big water accumulations and multiple rivers have allowed

engineers to develop an electric energy generation system based on water and supported by nuclear energy.

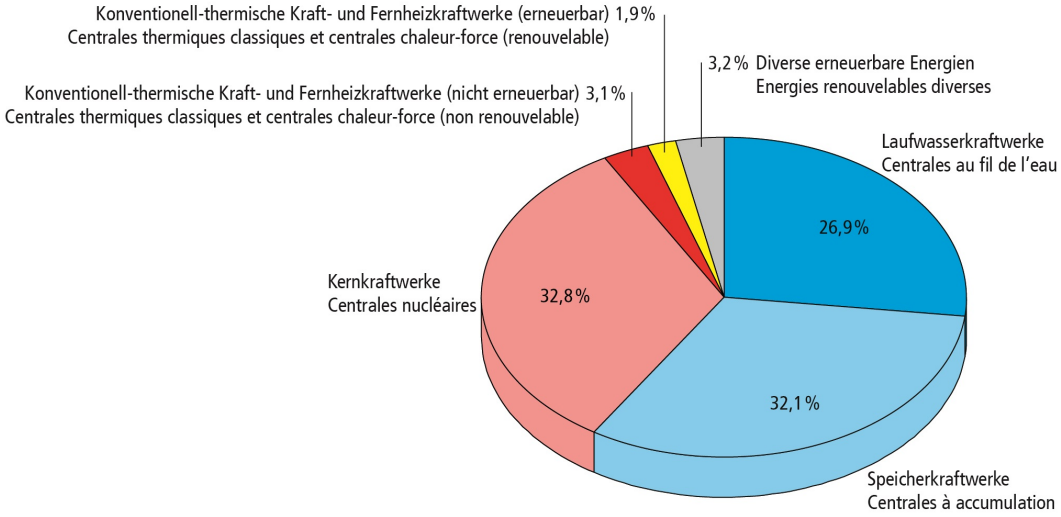

Figure 1.3: Electric energy generated in Switzerland in 2016, per central category. Source: BFE, Schweizerische Elektrizitätsstatistik 2016 [3].

This combination has many advantages: first, it has extremely low gas contaminant emissions; second, nuclear energy provides the base power in a very stable and relying way, since it almost always can provide its nominal power; third, the incoherences between the nuclear plus the hydraulic energy (not storaged) and the electricity demand are corrected with water reservoirs, which use turbines to produce electricity. Some of them can increase their water level with pumps when there is an excess of electricity generation; last but not least, the operational cost of this system is very reduced, since only nuclear energy needs fuel, and its price per GWh is not as high as coal or gas.

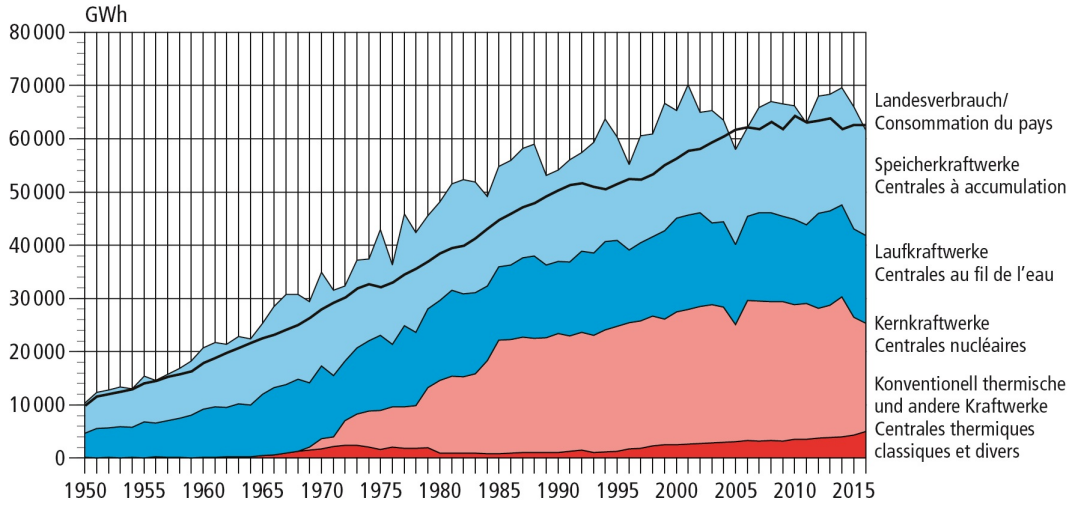

Figure 1.4: Evolution of electricity generation from 1950 to 2016, per central category. For most of the years, the total electricity generation is bigger than the total demand. Source: BFE, Schweizerische Elektrizitätsstatistik 2016 [3].

Apart from hydraulic and nuclear energy, biomass, cogeneration, solar and eolic are present in Switzerland. However, they represent a minority, having been all of them less than the 10% of the total energy generation in 2016 [3].

It is also interesting to observe the differences between the time of the day and the day of the year, in order to understand the contrast between the power needed during the moments of the year when less electricity is demanded, and those whose demand is lower.

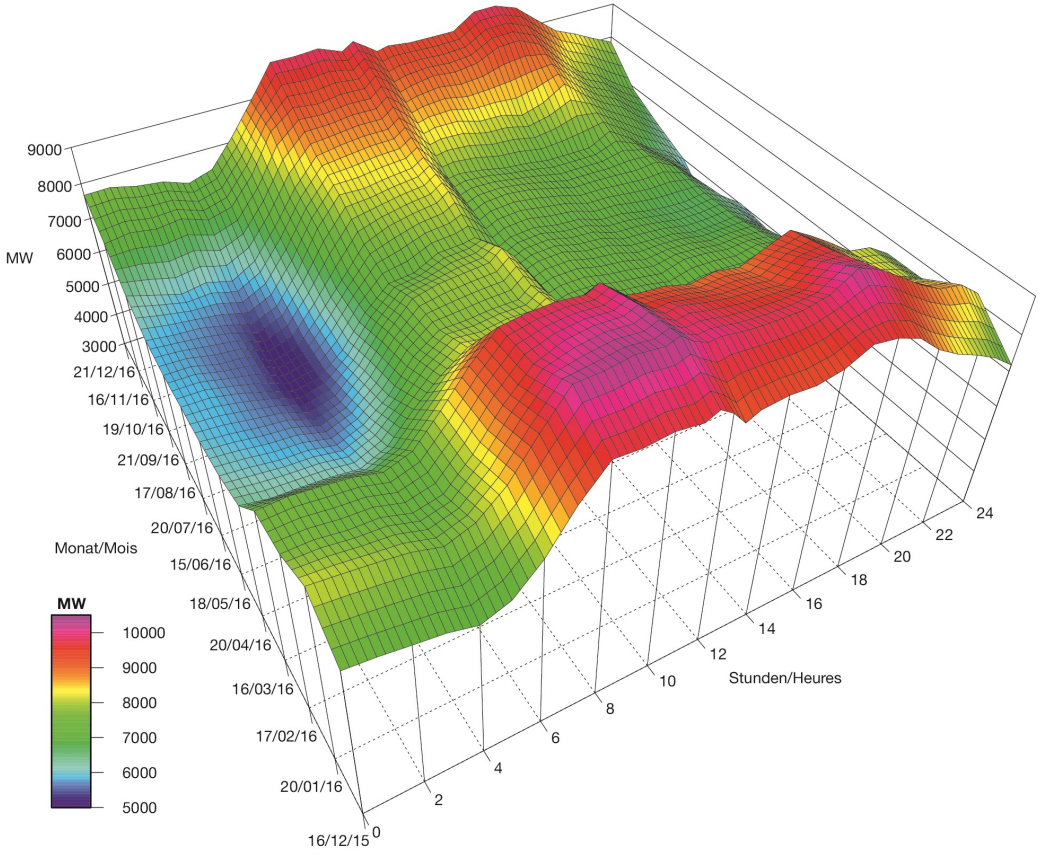

Figure 1.5: Electricity time demand, per hours and days, during 2016 in Switzerland. Source: BFE, Schweizerische Elektrizitätsstatistik 2016 [3].

In a day, the most energy demanding hours are the mornings, between 8 and 11 hours, as well as the evenings around 17 hours. In contrast, the least energy demanding hours are the nights, between 0 and 5 hours, since there is not much human activity. The power amplitude in a normal day is around 3000 MW.

During the year, the power contrasts are not as big as during a day, since the power difference between a day of summer and a day of winter is around 2000 MW. If a single hour was plotted during the whole year, the result would be a smooth curve with the maximum values present in winter and the lowest in summer, due to the warmer temperatures and more light hours. However, it is very important to understand that these oscillating power values between a single day and the year are huge in relative terms since, during the most energy demanding moment (around 11 am of 20th January), it is necessary to provide approximately 10000 MW, twice the power needed during the lowest energy demand moment (around 3 am during 20th July).

The seasonality is usually present in the energy demand curves along the year. However, countries with very high temperatures during summer and smooth temperatures during winter may require higher electrical power in the aestival season.

1.1.1 Swiss Energy Policy 2050

In May 2017, Switzerland celebrated a referendum to decide about the energy future. The main point was to determine if people wanted to keep using nuclear energy to feed the electricity demand of the country, and the result was no to nuclear.

The strategy of this energy policy plan is to gradually close the nuclear power plants in Switzerland and increase the presence of renewable energies and the energy efficiency of buildings and industries to reduce the average electricity per capita consumption.

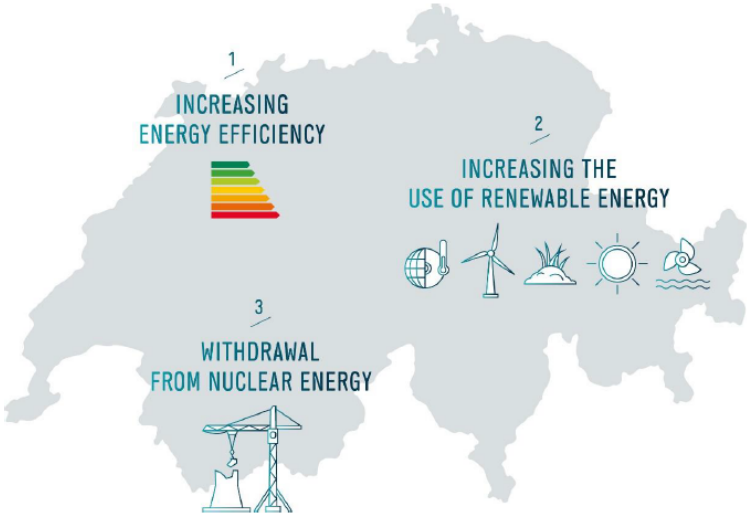

Figure 1.6: Principles of the Energy Strategy 2050 plan. Source: Swiss Federal Office of Energy, January 2018 [4].

However, moving to renewable energies such as solar or wind can be difficult, since they require certain meteorological conditions to work, being unstable and unpredictable sources. Therefore, it is still not known if gas power plants will be installed in order to satisfy high peak energy demands, which would be negative in terms of CO_2 emissions, as well as expensive, not only operationally but also in terms of initial investment.

Although the public opinion has sentenced the end of fission nuclear energy in the long term, the truth is that not everyone knows the fundamentals of a nuclear power plant, the operational risks and the real implications for the environment in the short, middle and long term.

The next pages of this report aim to explain the basic principles of nuclear power plants, as well as to introduce the topic of this Master's Thesis.

1.2 Nuclear Power Plants

Obtaining electrical energy from nuclear fission is usually seen as a very modern and powerful technology, but the truth is that it has been used for more than 60 years.

It was in Obninsk (Russia), on the 26^{th} June 1954 when, for the first time, a Nuclear Power Plant (NPP) was connected to a national power grid. Its name was *Atom Mirny*, and was still in semi-experimental status, providing a 5 MW_e output. Only two years later, on the 27^{th} August 1956, Calder Hall 1, in Cumbria (United Kingdom), was connected to the UK national power grid, providing a 50 MW_e output.

According to the International Atomic Energy Agency (IAEA), there are currently 451 operable civil nuclear power nuclear reactors around the world, with a further 58 under construction. In terms of power, it sums up to 394,84 GW_e installed, and 59,63 GW_e under construction.

Europe is the most nuclearized continent, with a total amount of 184 operating nuclear reactors, followed by Asia and North America, with 140 and 112 operating nuclear reactors, respectively. Africa is the continent with the fewest: only 2 operating nuclear reactors.

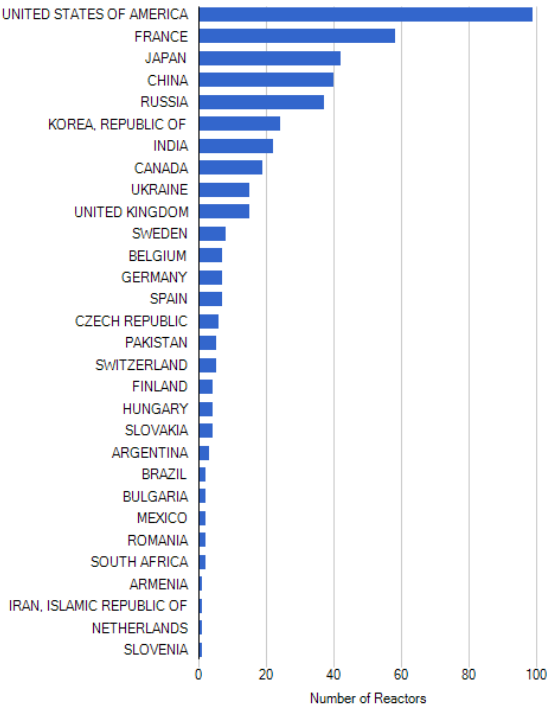

Figure 1.7: Number of nuclear reactors by country. Source: IAEA, data from June 2018 [5].

There are many projects under construction, especially in China, with 17 out of the 39 projects being built in Asia. The rest are being built in Europe, especially in the eastern part, with 13 out of 15 projects.

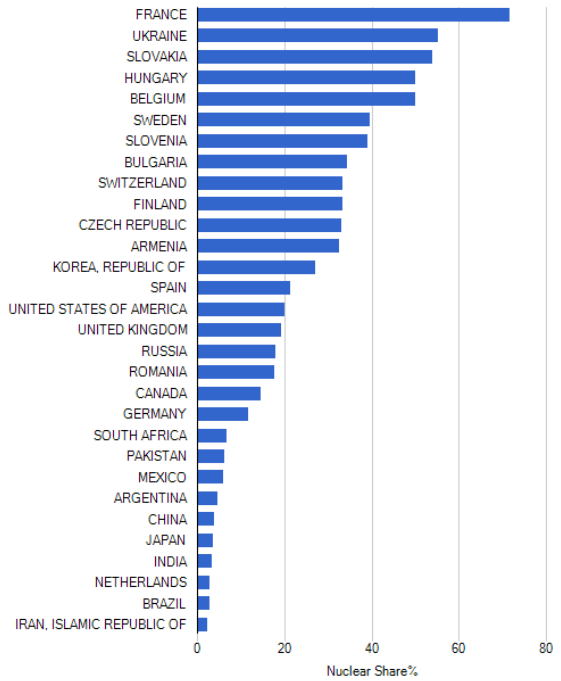

Figure 1.8: Share of nuclear energy by country. Source: IAEA, data from June 2018 [6].

It is also interesting to see the nuclear energy share by countries, as shown in figure 1.8, to get an idea of the importance of nuclear energy for the different countries in the world.

However, attention to the nuclear energy share trend, shown on figure 1.9, must be paid in order to understand the energy policies of these countries. For example, China has a nuclear energy share of about 4%, but the trend is that this technology presence is growing a lot. On the other side, Germany has a nuclear energy share of 11,5%, but it has been decreasing since 1999, Japan shows a strong denuclearization process after Fukushima accident and Switzerland remains stable for now.

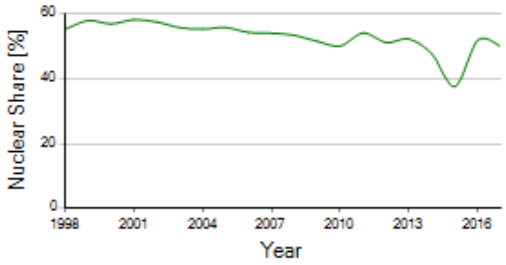

(a) Belgium

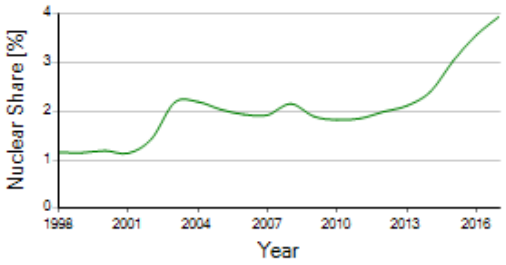

(b) China

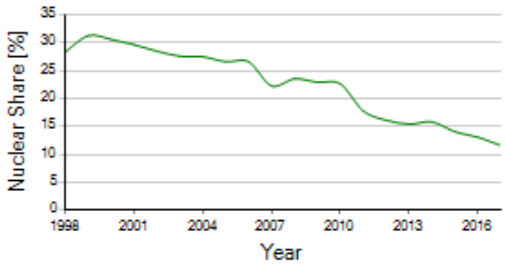

(c) Germany

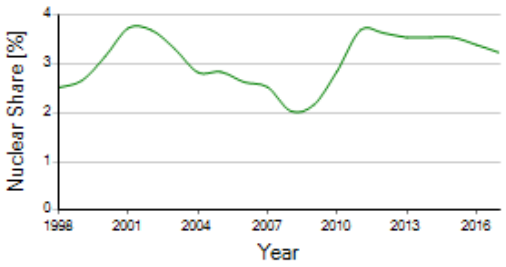

(d) India

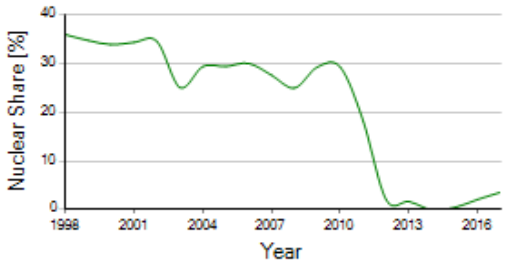

(e) Japan

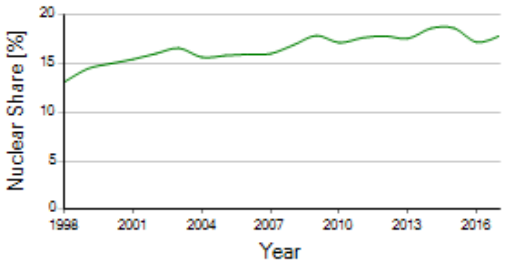

(f) Russia

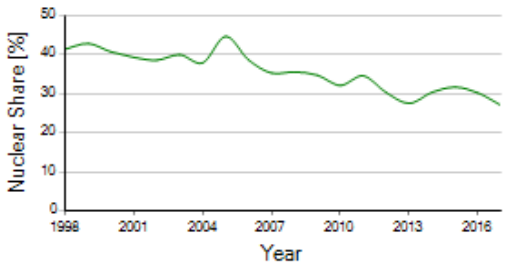

(g) South Korea

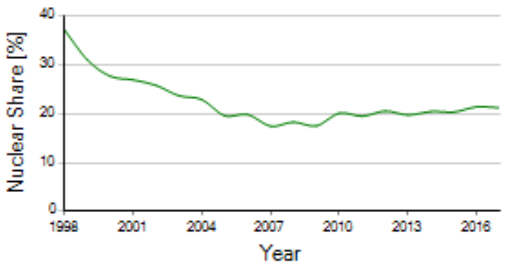

(h) Spain

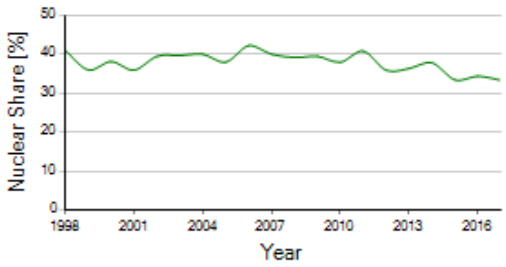

(i) Switzerland

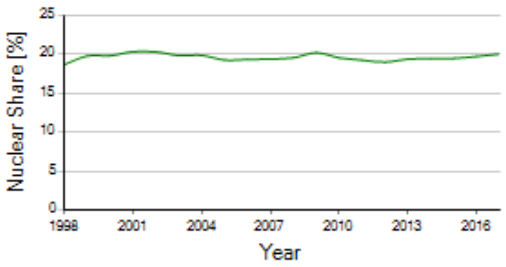

(j) United States of America

Figure 1.9: Nuclear share trend by country. Source: IAEA, data from June 2018 [7].

1.2.1 Types of nuclear power plants

Since the 1950s, there have been many developments related to nuclear energy in terms of security, functionalities, efficiency and operability. These advances have set the most popular classification of nuclear reactors: their generation.

Generation I Reactors

Generation I reactors were developed during the 1950s and the 1960s and their outputs were generally between 50 and 500 MW_e. They were very experimental and became the precursors of the commercial reactors that nowadays generate electricity throughout the world, known as generation II reactors. The last generation I nuclear reactors present in Europe were closed in the United Kingdom in 2010.

Figure 1.10: The Calder Hall nuclear power station, Cumbria, England, 1956. Source: Ann Ronan [8].

Generation II Reactors

Generation II reactors were developed between 1970 and 1996, boosted by the 1973 Oil crisis to ensure the energy independence of multiple countries, being France the main protagonist. Many advances in functionality aspects were developed, including the invention of new types of reactors and important improvements in security aspects, such as the use of passive elements that do not require human action or electricity supply to work. These reactors have a long life, designed to last 40 years of operation, extendible to 60 years of operation prior to complete overhaul and pressure vessel replacement. Around 85% of the electricity produced by nuclear energy in the world is generated by this type of reactors. There are three main technologies: Gas Cooled Reactors, Pressurized Heavy Water Reactors and Light Water Reactors.

Gas Cooled Reactors (GCR) were developed, constructed and operated by the United Kingdom government. In this country, 41 out of the 45 nuclear reactors ever built are GCR. The oldest design used CO_2 gas circulating through the core at a pressure of 1.6 MPa to exchange heat from the fuel elements.

Figure 1.11: Gösgen nuclear power plant, Däniken, Switzerland. Source: Eidgenössisches Nuklearsicherheitsinspektorat ENSI [9].

This type of reactors used natural uranium metal clad with an alloy of magnesium as fuel, known as Magnox. These reactors were the precursors of the newer Advanced Gas Cooled Reactors (AGR), which use a slightly enriched uranium dioxide clad with stainless steel as fuel.

Pressurized Heavy Water Reactors (PHWR), also known as Canada Deuterium-Uranium Reactors (CANDU), were developed in the late 1950s and 1960s by a partnership between Atomic Energy of Canada Limited (AECL), the Hydro-Electric Power Commission of Ontario, Canadian General Electric and other companies. All current power reactors in Canada are CANDUs, although this technology is also present in Korea, Argentina, Romania, China, India and Pakistan. They use deuterium-oxide (heavy water) as moderator and coolant and natural uranium as fuel, which offers a degree of energy independence.

Pressurized Water Reactors (PWR) are the first big group of Light Water Reactors (LWR) and the most common type of nuclear reactors in the world. They were originally designed by Westinghouse Bettis Atomix Power Laboratory for military ship applications, and then developed for commercial applications. However, other companies such as Asea Brown Boveri-Combustion Engineering (ABB-CE), Framatone, Kraftwerk Union, Siemens and Mitsubishi have also built this type of reactor throughout the world. They use light water as moderator and coolant, and enriched uranium oxide as fuel. The most special characteristic of PWR is that the coolant remains in liquid phase along the whole first loop thanks to a pressurizer that maintains the pressure at approximately 152 bar, increasing the saturation temperature to 343°C. In Switzerland, Beznau (1 and 2) and Gösgen use this type of reactors to work.

Boiling Water Reactors (BWR) are the second group of LWR, and were developed slightly after PWR by a collaboration between General Electric (GE) and several US national laboratories, especially Idaho National Laboratory (INL). At the present, GE Hitachi Nuclear Energy is the main manufacturer of this type of reactors. Like PWR, they use light water as moderator and coolant, and enriched uranium oxide as fuel. However, they lack of a pressurizer and boiling is present in the first loop. In Switzerland, Leibstadt and Muehleberg NPP use this type of reactors to work.

Generation III Reactors

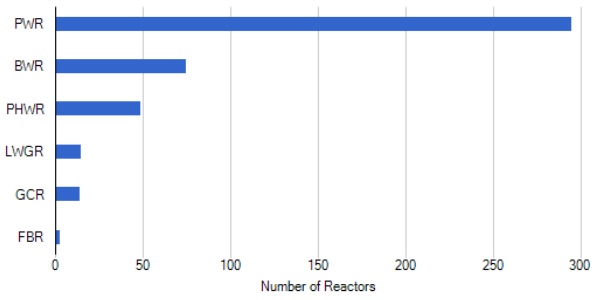

Figure 1.12: Number of nuclear reactors by type. Source: IAEA, data from June 2018. [10]

Generation III reactors are the natural evolution of generation II reactors. Their design incorporates improvements in characteristics such as fuel technology, superior thermal efficiency, enhanced safety systems, where the inclusion of passive nuclear safety has again an important role, and standardized design to reduce maintenance and capital costs. The first generation III operating reactor was built in Japan in 1996. These reactors can operate for a long time: from 60 to 120 years if their lives are extended.

The main types are enhanced PWR and BWR, incorporating safety systems such as a double containment, designed to withstand the impact of a large air-plane crash, and simplified designs that allow a big reduction in valves, pipes, cable and size of the seismic building.

Generation IV Reactors

Generation IV reactors are still being researched, and have 4 technological objectives: sustainability, safety and reliability, economy and non-proliferation. They are not expected to be available for commercial construction until 2020-2030. There are 6 main technologies being studied: Very-High Temperature Reactors, Lead-Cooled Fast Reactors, Supercritical-Water-Cooled Reactors, Gas-Cooled Fast Reactors, Sodium-Cooled Fast Reactors and Molten Salt Reactors.

This type of reactors have many benefits: their nuclear waste remains radioactive for a few centuries instead of millennia, they can provide from 100 to 300 times more energy yield from the same amount of nuclear fuel, they have improved operating safety feature and, in some reactors, it will be possible to consume existing nuclear waste for the production of electricity, closing the nuclear fuel cycle.

Due to the age of the current nuclear power plants, as shown in 1.13, in 10 to 20 years there will be a lot of disconnections of old generation II nuclear power plants. This installed power will have to be replaced by other power sources, or new generation III and IV nuclear power plants.

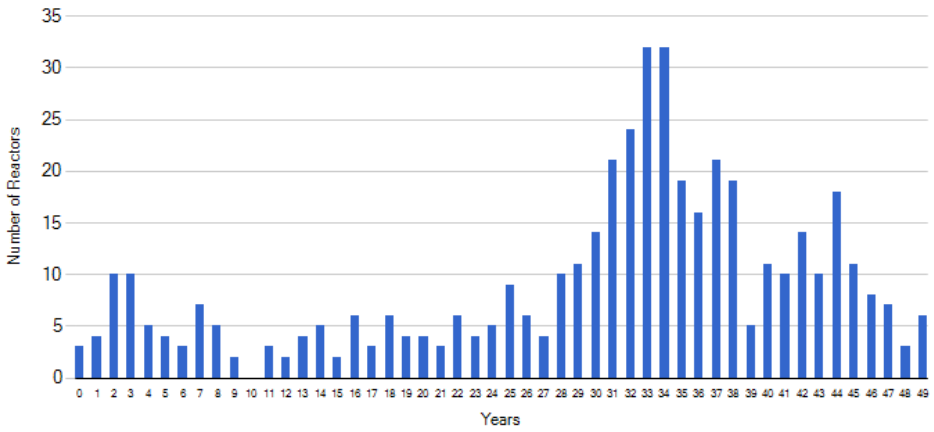

Figure 1.13: Age histogram of operating nuclear power plants. Source: IAEA, data from June 2018. [11]

1.2.2 Pressurized Water Reactors

Nowadays, the Pressurized Water Reactor is the most used type of nuclear reactor in the world. Before going further on the purpose of this thesis, it is necessary to understand the fundamentals of a Nuclear Power Plant and, specifically, of a PWR. To do so, the author will focus on the Westinghouse PWR design. Approximately, the electrical power output is 1 GW.

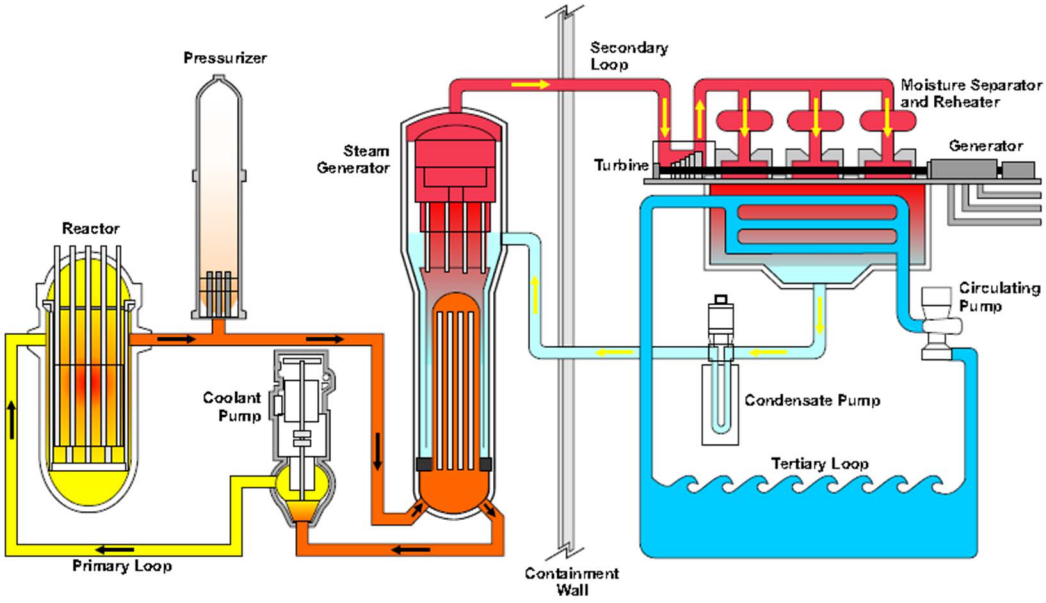

Figure 1.14: Pressurized Water Reactor scheme.

PWR Nuclear Power Plants use light water as moderator and coolant, and enriched uranium oxide as fuel. They have three major structures: the containment building, which houses the reactor and its high pressure steam generating equipment, the turbine building, which houses the steam turbines, condensers the electrical generator, and the auxiliary building, which houses normal and emergency support systems. Depending on the location of the nuclear power plant, there may or may not be a cooling tower to remove the excess heat from the facility.

In terms of design, PWR Nuclear Power Plants have three different water loops:

Primary loop

This water circuit is marked in orange and yellow in figure 1.14, and its role is to transport the heat from the fuel rods inside the reactor to the steam generator. Since the fuel rods have very high temperatures, it is necessary to pressurize the water inside this primary loop to a pressure of 152 bar in order to increase the boiling temperature of water and ensure that it remains in liquid phase. To do so, a pressurizer consisting of a heater and a spray system is used. After removing heat from the reactor, the water goes to the steam generator through a heat exchanger inside it. This circuit is fed by a pump. There can be more than one steam generator for the same nuclear reactor.

Secondary loop

This water circuit is marked in red and light blue in figure 1.14, and its role is to transport the high pressure steam from the steam generator to the turbines. After that, the very low pressure steam (around

0,06 bar) goes through the condenser, reducing its enthalpy and becoming water again. Finally, a pump increases the pressure to the working value (around 69 bar), and the cycle starts again. Unlike in BWR, the water passing through the turbines is not contaminated by radioactivity, since there are different closed loops.

Tertiary loop

This water circuit is marked in blue in figure 1.14, and its role is to exchange heat with the low pressure steam after the turbines. It is an open circuit, which means that the water is not recirculated, and it usually comes from the sea or a river. There are some nuclear power plants that do not have a condensation tower, in which case the steam out the turbine's pressure is equal to the atmospheric pressure, and some efficiency is lost due to the loss of enthalpy absorbed from the steam in the turbines.

Reactor core in a PWR

It is also important to have a good insight of the design fundamentals of the reactor core in order to understand what this project is about.

In a PWR, the reactor core is inside the reactor vessel, a cylindrical body with a hemispherical bottom head and a removable hemispherical upper head that allows the refuelling of the reactor. It is about 13 m high and it has a 20 cm steel wall thickness and a 4 m inner diameter, being its total weigh around 314 Tn.

The fuel assemblies are situated inside the vessel, as well as all the associated support and alignment devices. These fuel assemblies consist of a square array of 179 to 264 fuel rods, and 121 to 193 fuel assemblies can be loaded into an individual reactor, depending on the number of loops. Each fuel rod is formed by hundreds of 8 to 10 mm diameter UO_2 pellets, which are inserted into a Zircaloy-4 tube.

In order to assure structural resistance, spacer grids, which can also have mixing vanes attached to them, are situated on different parts of the reactor, as well as a bottom and a top nozzle on the extremes of the fuel assembly. The coolant flows up in the gaps between the fuel rods, named sub-channels.

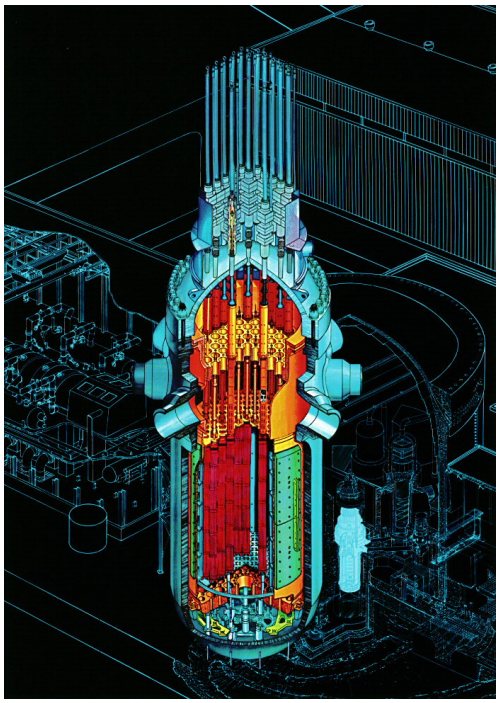

Figure 1.15: Pressurized Water Reactor vessel.

Mixing vanes optimization

There are different critical points that can be enhanced in a PWR to improve its global operating conditions and safety related issues. One of them is the heat-flow exchange between the fuel rods and the coolant, that must be high enough to avoid boiling crisis, which can happen in two different ways: Departure from Nucleate Boiling (DNB) and Dryout.

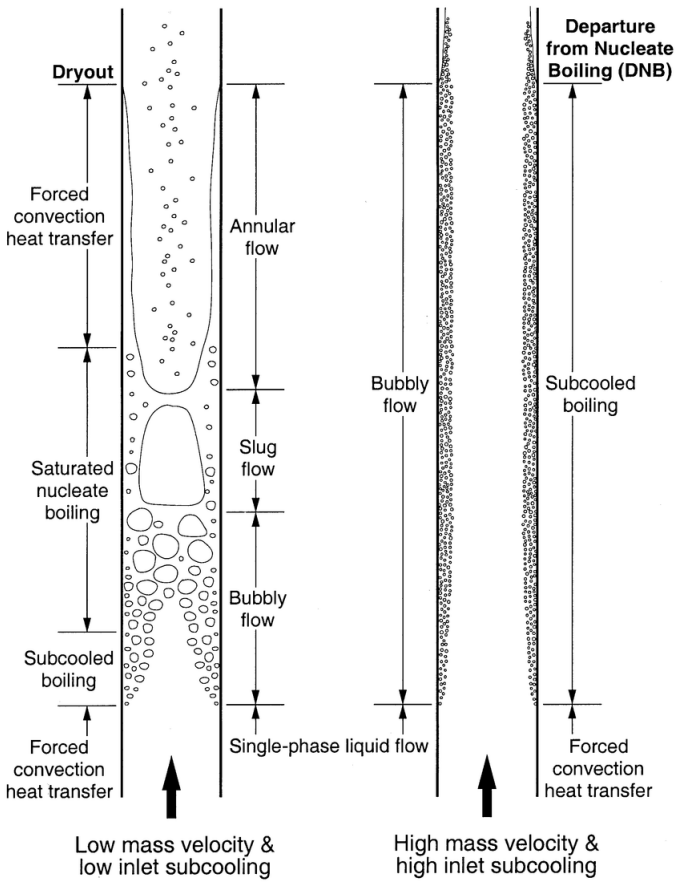

Figure 1.16: Dryout and DNB scheme.

The DNB occurs when the evaporation rate at the fuel rod is so high that a steam film is placed around it, acting as a insulator and decreasing the heat-flow exchange drastically. The Dryout can occur in annular flow regimes, where the mass flux is basically steam and a liquid film is covering the rods. When this film is locally evaporated, the rod is directly in contact with the steam. For both cases, after some time, the non-dissipated heat present in the rod increases its temperature and dangers its integrity, and it can even provoke a radioactive release or core melt down.

The mixing vanes situated on the spacer grids' body increase the turbulence of the flow, improving the heat-flow exchange and avoiding boiling crisis. The turbulent flow generated by the mixing vanes generally consists of a swirling flow in a sub-channel and a cross flow at the gaps. The swirling flow improves the heat-flow between the rod surface and the coolant, while the cross flow mixes the water of different sub-channels, uniforming their temperature.

The turbulent flow in the sub-channels depends on the vane configuration and the pattern of the vane adjustment on the spacer grid.

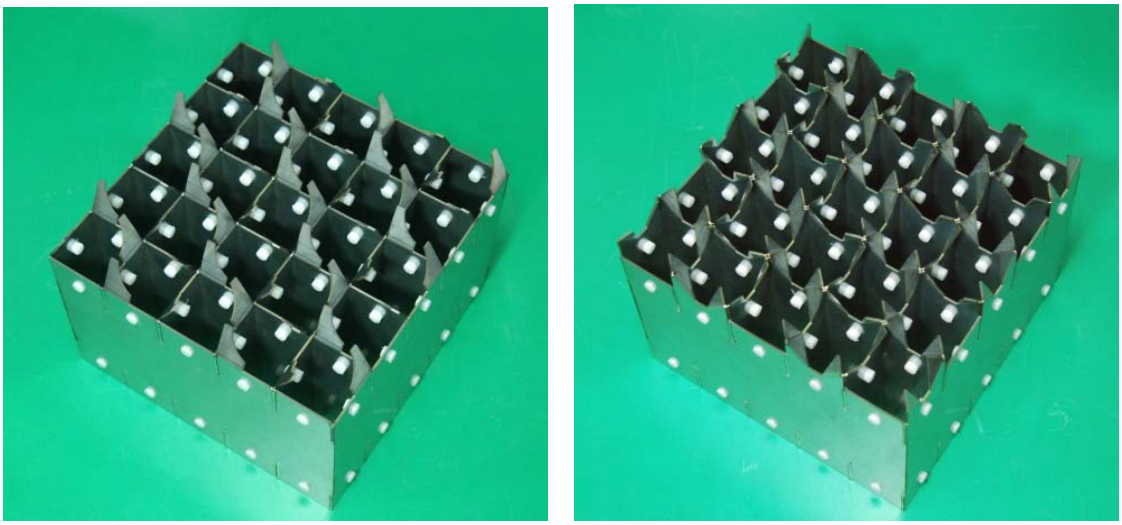

(a) Split-type spacer grid. **(b)** Swirl-type spacer grid.

Figure 1.17: The two types of spacer grids with mixing vanes that will be simulated.

1.3 What to expect from this project

This project aims to develop a Computational Fluid Dynamics (CFD) model able to reproduce the physical conditions of the real experiment in which Dr. Ing. Arto Tapio Ylönen worked for his doctoral dissertation. In order to do so, a 3D geometry will be designed and simulated together with the different types of mixing vanes.

This project is **not** an optimization of the mixing vanes, which could be the subject of another study, but a validation of a CFD simulation based on the results of an experiment.

1.3.1 PSI Experimentation

In January 2013, Dr. Ing. Ylönen presented his doctoral dissertation, having studied single-phase mixing and two-phase flow in a 4x4 rod bundle with square lattice.

He designed, constructed and tested a *SUB-channel FLOW (SUBFLOW)* test facility able to take measurements of the flow thanks to a two-layer conductivity wire mesh. Many tests were executed with and without spacer grids, using an injected salt water tracer (Na_2SO_4) at the same velocity than the flow to take the measurements, due to its different electrical conductivity.

The measurements were taken in 6 different planes: 50 mm, 150 mm, 250 mm, 350 mm, 450 mm and 550 mm from the top of the spacer, while the injection was always done 157.5 mm before the spacer. 6 geometries were tested (4 spacer types + 1 spacer body + 1 bare bundle) using two different flow velocities: 0.8 m/s and 1.2 m/s.

The different mixing vanes were compared, existing big differences between the flow structures and the swirl-type generated, which will have a great impact on the heat-flow exchange between the coolant and the fuel rods.

1.3.2 CFD model creation importance

Nowadays numerical simulations are playing an important role in industrial processes in order to save time and money. When it comes to turbulent flows inside fuel bundles of reactor cores, careful validation against trustworthy experimental data is needed, due to the inherent complexity of the flow.

After validation, researchers can extract a lot of detailed data from the CFD model, especially those hard to be measured in the experiment.

Chapter 2

State of the art

2.1 Previous work

A lot of experiments and simulation work about the flow structure at the downstream of the mixing vanes in a rod bundle has been done.

Rehme and Trippe, 1980 [12] evaluated the pressure drop and the velocity distribution in a hexagonal 19 rod bundle. The axial velocities in a sub-channel were measured at downstream of the spacer grid using a Pitot tube, but the values were too low to estimate the actual velocity profiles.

Yao et al., 1982 [13] studied the heat-transfer augmentation in rod bundles near spacer grids, but they did not consider the flow mixing.

Shen et al., 1991 [14] performed an investigation of the cross-flow mixing effect caused by spacer grids with mixing vanes in a 4x4 rod bundle using a Laser Doppler Velocimeter (LDV). They noticed the swirling flow at the centre of sub-channels, the cross-flow in the gaps downstream of the spacer grid and how fast the turbulence intensity of the lateral flow decays as the flow advances until it reaches a certain value and then becomes constant at a downstream distance of 21 times the hydraulic diameter (D_H).

Karouta et al., 1995 [15] worked on a CFD analysis in a square sub-channel geometry. They compared the results from the simulation against the experimental ones and found a good match of the lateral velocities. However, the axial velocities did not match so well because of the assumption of an infinitesimal vane thickness in the calculation.

Yang and Chung, 1998 [16] did measurements of the axial velocity and the turbulent intensity of the flow inside a 5x5 rod bundle with spacer grids using a LDV. They also measured the swirl decay, as well as the skewness and flatness factors and the pressure drop downstream of the spacer grid.

Langford et al., 2001 [17] performed measurements of the swirling flow in a square 5x5 rod bundle geometry using the Dynamic Particle Image Velocimetry (DPIV) technique. They used two different types of split-type mixing vanes. They measured the lateral velocity and vorticity fields in a sub-channel for six different planes downstream of the spacer grid.

Holloway et al., 2006 [18] conducted an investigation of the swirling flow in rod bundle sub-channels

using CFD. They compared the results obtained from a CFD simulation in a two-sub-channel geometry with periodicities against the experimental results obtained using a LDV in a square 17x17 rod bundle geometry. They found a good agreement between both results close to the spacer grid.

Holloway et al., 2008 [19] worked on experiments of single-phase convective heat transfer in rod bundles. They built a heated 5x5 rod bundle geometry with a special sensor to measure the rod wall temperature. The measured results showed an enhancement of the heat transfer for up to 10 D_H downstream of the spacer grid.

Domínguez-Ontiveros and Hassan, 2009 [20] did a non-intrusive experimental investigation of flow behaviour inside a 5x5 rod bundle with spacer grids using Matching Index of Refraction (MIR) and DPIV techniques. They obtained full field velocity vectors and turbulence statistics for the rod bundle under single phase flow conditions.

Caraghiaur et al., 2009 [21] performed an experimental investigation of the turbulent flow in a 24 rod bundle geometry with spacer grids. They measured experimental data on pressure, axial velocity and turbulence intensity using LDV technique.

Conner et al., 2010 [22] worked on a CFD methodology and validation for single-phase flow in PWR fuel assemblies. They used Star-CD code to model a 5x5 rod bundle geometry and compared the lateral velocity and heat transfer CFD results against experimental data they got using PIV technique and a specially designed sensor rod. They validated the CFD methodology since the CFD results matched the experimental data accurately.

Liu and Ferng, 2010 [23] performed numerical simulations of the thermal-hydraulic characteristics within the fuel rod bundle using CFD methodology. They compared the flow mixing and heat transfer capability results obtained from the CFD simulation against the experimental ones for standard-type and split-type mixing vanes. They noted that the split-type one enhances both the flow mixing and the heat transfer capability more than the standard grid does. They also compared the results for the Nusselt (Nu) number distribution downstream the grid, which shows reasonable agreement for the standard grid design, but not for the split-vane.

Horváth and Dressel, 2012 [24] performed numerical simulations of square arrayed rod bundles using CFD. They tested geometries with different pitch to diameter (P/D) ratios in order to find an optimal mesh and turbulence model for simulations with complex geometries in the future. They used StarCD software, and developed mesh and turbulence model sensitivity analysis. They found that GL Reynolds Stress Model was the best match for their cases.

The Committee on the Safety of Nuclear Installations of the Nuclear Energy Agency published its report of the OECD/NEA KAERI Rod Bundle CFD Benchmark Exercise, 2013 [25], that shows the results of a CFD exercise in which 25 different participants took part. Lee, Kim and Song (2014) [26] worked on a synthesis explaining the results of the full report. Two different 5x5 rod bundle geometries, corresponding to split-type and swirl-type mixing vanes, were given to the participants, who performed CFD simulations with different mesh sizes and turbulence models without knowing the real data from the experimental results. After analysing the data, each simulation was given a mark based on the error of their results compared to the experimental ones in 12 probe lines, and it was surprising to see that, although there were cases with more than 100 M cells and people who used DES or LES, the most accurate one was a 13.1 M cells using a SAS-SST turbulence model.

Li and Gao, 2014 [27] developed methods of simulating large-scale rod bundles and an application to a 17x17 fuel assembly with mixing vane spacer grid. They performed mesh sensitivity analysis with polyhedral and tetrahedral meshes using a periodic boundary condition to minimize the computational charge. The polyhedral mesh shows higher computational efficiency and better convergence properties compared to the tetrahedral mesh. The simulation results show reasonable agreement when compared to the experimental data.

Bieder et al., 2015 [28] performed a CFD analysis of the flow in the near wake of a generic PWR mixing vanes. They compared the CFD simulation results against experimental data obtained from measurements in the AGATE facility and Trio_U calculations. The CFD simulations were LES and RANS using k-ε turbulence model. They compared cross-flow and axial velocities, and it showed that the results right after the mixing vanes are insensitive to the turbulence model and the inertia forces are dominant. They conclude recommending not to use RANS models near the mixing vanes.

2.2 Current work

Due to the complexity of bundle channel geometry and the turbulence inside, some experimental and simulation work remains quite active. Yet it has not been clearly concluded which mesh type and turbulence models are best.

In this project, a different approach to the problem was used. A tracer was used in the experiment, set as a passive scalar in the simulation. This made it possible to model its distribution, in order to study the consequence of turbulent enhanced mixing instead of focusing in velocity profiles or temperature distribution.

Besides, mesh improvements were implemented, introducing high quality hexahedral mesh in the bare bundle parts of the geometry.

Last but not least, unsteady RANS (URANS) simulations, cheaper and faster than LES, were performed, and some dynamic instabilities that leaded to enhanced mixing were captured.

Chapter 3

Theoretical background

3.1 Mathematical model of the flow

In this chapter, the mathematical formulation of incompressible single-phase flow is presented. For single-phase flow, the whole control volume is filled with either one continuous gas fluid or one continuous liquid fluid. In this study, the single-flow fluid is incompressible water.

Mass conservation equation

The rate of temporal change of mass in a control volume and the sum of inlet and outlet mass flows should be balanced. Since this study deals with an incompressible fluid, the rate of temporal change of mass in the control volume is equal to 0.

$$\frac{\partial u_x}{\partial x} + \frac{\partial u_y}{\partial y} + \frac{\partial u_z}{\partial z} = \nabla \cdot \vec{u} = 0 \tag{3.1}$$

Where velocity $\vec{u}$ is expressed in m/s and lengths x, y and z in m.

Momentum conservation equation

The motion of Newtonian fluid is described by the momentum conservation equations. These, known as the Navier-Stokes equations, postulate that the change of momentum in space and time equals the sum of forces acting on the bounding surfaces and the mass of the control volume.

$$\rho\left(\frac{\partial u_x}{\partial t} + u_x\frac{\partial u_x}{\partial x} + u_y\frac{\partial u_x}{\partial y} + u_z\frac{\partial u_x}{\partial z}\right) = -\frac{\partial P}{\partial x} + \mu\left(\frac{\partial^2 u_x}{\partial x^2} + \frac{\partial^2 u_x}{\partial y^2} + \frac{\partial^2 u_x}{\partial z^2}\right) + F_{V,x} \tag{3.2}$$

$$\rho\left(\frac{\partial u_y}{\partial t} + u_x\frac{\partial u_y}{\partial x} + u_y\frac{\partial u_y}{\partial y} + u_z\frac{\partial u_y}{\partial z}\right) = -\frac{\partial P}{\partial y} + \mu\left(\frac{\partial^2 u_y}{\partial x^2} + \frac{\partial^2 u_y}{\partial y^2} + \frac{\partial^2 u_y}{\partial z^2}\right) + F_{V,y} \tag{3.3}$$

$$\rho\left(\frac{\partial u_z}{\partial t} + u_x\frac{\partial u_z}{\partial x} + u_y\frac{\partial u_z}{\partial y} + u_z\frac{\partial u_z}{\partial z}\right) = -\frac{\partial P}{\partial z} + \mu\left(\frac{\partial^2 u_z}{\partial x^2} + \frac{\partial^2 u_z}{\partial y^2} + \frac{\partial^2 u_z}{\partial z^2}\right) + F_{V,z} \tag{3.4}$$

Where density ρ is expressed in kg/m^3, time t in s, velocity u in m/s, pressure P in Pa, dynamic

viscosity μ in $Pa \cdot s$, volumetric force F_V in N/m^3, and lengths x, y and z in m.

Navier-Stokes are non-linear partial differential equations due to the convective acceleration term. Since there is no general analytic solution found, they have to be solved numerically for every specific case.

Energy conservation equation

The rate of change in energy is equal to the net energy flux and the rate of work done by forces. The dissipation Φ_e, expressed in equation 3.6 for incompressible flows, is the thermal energy converted from the friction losses of the fluid, and is always positive and irreversible.

$$\begin{aligned}\rho\left(\frac{\partial h}{\partial t}+u_x\frac{\partial h}{\partial x}+u_y\frac{\partial h}{\partial y}+u_z\frac{\partial h}{\partial z}\right)=&\left(\frac{\partial P}{\partial t}+u_x\frac{\partial P}{\partial x}+u_y\frac{\partial P}{\partial y}+u_z\frac{\partial P}{\partial z}\right)\\&+\left[\frac{\partial}{\partial x}\left(\lambda\frac{\partial T}{\partial x}\right)+\frac{\partial}{\partial y}\left(\lambda\frac{\partial T}{\partial y}\right)+\frac{\partial}{\partial z}\left(\lambda\frac{\partial T}{\partial z}\right)\right]+\rho\dot{q_s}+\mu\Phi_e\end{aligned} \tag{3.5}$$

$$\Phi_e = 2\left[\left(\frac{\partial u_x}{\partial x}\right)^2+\left(\frac{\partial u_y}{\partial y}\right)^2+\left(\frac{\partial u_z}{\partial z}\right)^2\right]+\left(\frac{\partial u_y}{\partial x}+\frac{\partial u_x}{\partial y}\right)^2+\left(\frac{\partial u_z}{\partial y}+\frac{\partial u_y}{\partial z}\right)^2+\left(\frac{\partial u_x}{\partial z}+\frac{\partial u_z}{\partial x}\right)^2 \tag{3.6}$$

Where density ρ is expressed in kg/m^3, time t in s, velocity u in m/s, enthalpy h in J/kg, pressure P in Pa, dynamic viscosity μ in $Pa \cdot s$, temperature T in K, thermal conductivity λ in $W/m \cdot K$, energy source $\dot{q_s}$ in W/kg, and lengths x, y and z in m.

Since the empirical experiment was performed with no heating in the fuel rods, the CFD model will be isothermal. Therefore, the energy conservation equation will not be used. Instead, a transport equation is solved for a passive scalar, which represents the tracer.

3.2 Numerical methods

The Navier-Stokes equations have analytically described the flow field. However, in order to obtain numerical solutions, different numerical methods and models are needed, depending on the computational capacity and desired grade of accuracy.

3.2.1 Direct Numerical Simulation

The Direct Numerical Simulation (DNS) numerically solves the Navier-Stokes equations without any turbulence model. For that, the whole range of spatial and temporal scales of the turbulence must be resolved in the computational mesh, from the smallest dissipative scales (Kolmogorov scales) to the integral scale l, the motions containing most of the kinetic energy.

Since it is necessary to solve the Kolmogorov scales η, the resolution of the mesh must be high. The number of cells n will be determined by l/η.

$$n \approx \frac{l}{\eta} \tag{3.7}$$

$$\eta = \sqrt[4]{\frac{\nu^3}{\varepsilon}} \tag{3.8}$$

$$\varepsilon \approx \frac{u'^3}{l} \tag{3.9}$$

$$Re_l = \frac{u'l}{\nu} \tag{3.10}$$

Where Kolmogorov scale η and integral scale l are expressed in m, kinematic viscosity ν in m^2/s, kinetic energy dissipation rate ε in m^2/s^3 and velocity fluctuation u' in m/s.

Thus, with the previous equations, it is possible to express the number of cells n as:

$$n \propto Re_l^{3/4} \tag{3.11}$$

However, in all three dimensions, the total number of cells n is proportional to $Re_l^{9/4}$. Therefore, DNS are very expensive simulations normally limited to small regions with low Reynold numbers in academic environments. Normally, engineering applications do not need such a high level of accuracy, and the post-processing tasks can be extremely complex and costly.

3.2.2 Large Eddy Simulation

In turbulent flows, large eddies carry most of the kinetic energy as well as the transport of the conservation variables, while dissipation is the small scales' main effect. Large Eddy Simulation (LES) is an inherently transient technique in which the large scales of the turbulence are directly resolved everywhere in the flow domain, and the small-scale motions are modelled throughout a low-pass filtering of the Navier-Stokes equations called sub-grid scale model.

The sub-grid scale model is based on an artificial eddy viscosity approach in which the effects of turbulence are included into the turbulent viscosity. Therefore, this simplification considers the dissipation of kinetic energy at sub-grid scales as analogous to molecular diffusion. Mathematically:

$$\tau_{ij}^r - \frac{1}{3}\tau_{kk}\delta_{ij} = -2\nu_t \mathbf{S} \tag{3.12}$$

$$\mathbf{S} = \frac{1}{2}\left(\frac{\partial \overline{u}_i}{\partial x_j} + \frac{\partial \overline{u}_j}{\partial x_i}\right) \tag{3.13}$$

Where the sub-filter scale stress tensor τ_{ij}^r is expressed in N/m^2, the eddy viscosity ν_t is expressed in m^2/s and the mean strain rate tensor $\mathbf{S}$ is expressed in s^{-1}.

This is a big advantage in terms of cost of the simulation, since the necessary computational capacity to perform them is much less than in DNS. However, this technique is still very expensive compared to RANS.

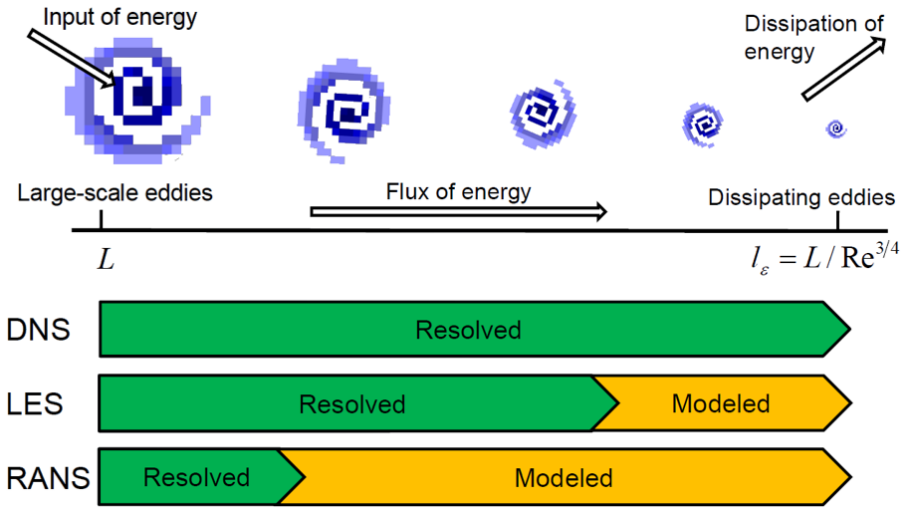

Figure 3.1: Comparison between the different numerical models. Source: Introduction to CFD course. University of Oviedo.

3.2.3 Reynolds Averaged Navier-Stokes

In most of the cases, the calculation of the full spectrum of turbulent eddies is not necessary for engineering applications, and it is sufficient with the averaged values. For that, Reynolds-Averaged Navier-Stokes (RANS) turbulence models are used.

Mainly, for RANS models, each solution variable ϕ in the instantaneous Navier-Stokes equations is decomposed into its averaged value $\overline{\phi}$ and its fluctuating component ϕ'.

$$\phi = \overline{\phi} + \phi' \tag{3.14}$$

Where ϕ represents velocity components, pressure, energy or species concentration.

For a stationary, incompressible Newtonian fluid, RANS equations can be written as:

$$\rho \overline{u}_j \frac{\partial \overline{u}_i}{\partial x_j} = \rho \overline{f}_i + \frac{\partial}{\partial x_j}\left[-\overline{p}\delta_{ij} + 2\mu \mathbf{S} - \boxed{\rho \overline{u_i' u_j'}} \right] \tag{3.15}$$

Where the additional boxed term corresponds the Reynolds stress tensor, which is defined as following:

$$\rho \overline{u_i' u_j'} = \mathbf{T_t} = -\rho \begin{pmatrix} \overline{u'u'} & \overline{u'v'} & \overline{u'w'} \\ \overline{u'v'} & \overline{v'v'} & \overline{v'w'} \\ \overline{u'w'} & \overline{v'w'} & \overline{w'w'} \end{pmatrix} \tag{3.16}$$

The different turbulence models available try to provide a closure of the governing equations by modelling $\mathbf{T_t}$ in terms of the mean flow quantities. STAR-CCM+, the software suite used to perform the simulations of this project, has two different approaches: Eddy Viscosity Models and Reynolds Stress Transport (RST) Models.

Eddy Viscosity Models

This first approach is based on the analogy between turbulent motion and the molecular gradient diffusion process. It is possible to model the anisotropic part of the Reynolds stress tensor $\mathbf{T_{t_{ani}}}$ as a function of mean flow quantities thanks to the Boussinesq eddy-viscosity approximation μ_t:

$$\mathbf{T_{t_{ani}}} = 2\mu_t \mathbf{S} - \frac{2}{3}(\mu_t \nabla \cdot \overline{v})\mathbf{I} \tag{3.17}$$

$$\mathbf{S} = \frac{1}{2}(\nabla \overline{\mathbf{v}} + \nabla \overline{\mathbf{v}}^T) \tag{3.18}$$

Where the mean strain rate tensor $\mathbf{S}$ is expressed in s^{-1}, the turbulent viscosity μ_t in m^2/s, the mean velocity $\overline{v}$ in m/s and $\mathbf{I}$ represents the identity tensor.

The different eddy viscosity models solve additional transport equations that enable the turbulent viscosity μ_t to be derived. For this project, standard k-ε, V^{2}F k-ε, k-ω and Spalart-Allmaras are used.

K-Epsilon model

The k-ε turbulence model was originally developed in the 1970s by Jones and Launder [29] and it is nowadays widely used in the industry, since it produces good results in fully-developed turbulent pipe flows far from a solid wall. It is a two-equation model that solves transport equations for the turbulent kinetic energy k and the turbulent dissipation rate ε in order to determine the turbulent viscosity μ_t.

$$\mu_t = \rho C_\mu f_\mu k T \tag{3.19}$$

Where ρ is the density, C_μ is a model coefficient, f_μ is a damping function, and T is the turbulent time scale, which is calculated as following:

$$\max\left(T_e, C_t\sqrt{\frac{\nu}{\varepsilon}}\right), \text{ for } \textit{Realizable Scale Option} \text{ deactivated} \tag{3.20}$$

$$\max\left(\min\left(T_e, \frac{C_T}{C_\mu f_\mu \mathbf{S}}\right), C_t\sqrt{\frac{\nu}{\varepsilon}}\right), \text{ for } \textit{Realizable Scale Option} \text{ activated} \tag{3.21}$$

Where $T_e = k/\varepsilon$ is the large-eddy time scale, C_t and C_T are model coefficients, ν is the kinematic viscosity and $\mathbf{S}$ is the mean strain rate tensor.

As for the transport equations for the kinetic energy k and the turbulent dissipation rate ε:

$$\frac{\partial}{\partial t}(\rho k) + \nabla \cdot (\rho k \overline{\mathbf{v}}) = \nabla \cdot \left[\left(\mu + \frac{\mu_t}{\sigma_k}\right)\nabla k\right] + P_k - \rho(\varepsilon - \varepsilon_0) + S_k \tag{3.22}$$

$$\frac{\partial}{\partial t}(\rho \varepsilon) + \nabla \cdot (\rho \varepsilon \overline{\mathbf{v}}) = \nabla \cdot \left[\left(\mu + \frac{\mu_t}{\sigma_\varepsilon}\right)\nabla \varepsilon\right] + \frac{1}{T_e} C_{\varepsilon 1} P_\varepsilon - C_{\varepsilon 2} f_2 \rho\left(\frac{\varepsilon}{T_e} - \frac{\varepsilon_0}{T_0}\right) + S_\varepsilon \tag{3.23}$$

Where v is the mean velocity; μ is the dynamic viscosity; σ_k, σ_ε, C_{ε_1}, and C_{ε_2} are model coefficients;

P_k and $P\varepsilon$ are production terms; f_2 is a damping function; ε_0 is the ambient turbulence value and S_k and S_ε are the user-specified source terms.

V2F k-ε model

The V2F model is a sub-model of k-ε designed to capture the near-wall turbulence effects more accurately than the Standard model. It is a low Reynolds number model and it takes better account of wall blocking effects in terms of heat transfer, skin friction and flow separation. It solves transport equations for two more turbulence quantities in addition to k and ε: the the wall-normal stress component $\overline{\vartheta^2} = \overline{v'v'}$ and the elliptic relaxation parameter f. Therefore, the turbulent eddy viscosity is calculated as follows:

$$\mu_t = \rho \min(C_\mu kT, C_{\mu_\vartheta^2} \vartheta^2 T_S) \tag{3.24}$$

Where ρ is the density; C_μ and $C_{\mu_\vartheta^2}$ are model coefficients and T and T_S are turbulent time scale and limited time scale, respectively.

The turbulent time scale T is defined in equations 3.20 and 3.21, and the limited time scale T_S is defined as follows:

$$T_S = \max\left(T_e, C_t, \sqrt{\frac{\nu}{\varepsilon}}\right) \tag{3.25}$$

Where $T_e = \frac{k}{\varepsilon}$ is the large-eddy time scale, C_t is a model coefficient, ν is the kinematic viscosity and $\mathbf{S}$ is the mean strain rate tensor defined in equation 3.18.

As for the transport equations for the kinetic energy k, the turbulent dissipation rate ε, the wall-normal stress component $\overline{\vartheta^2} = \overline{v'v'}$ and the elliptic relaxation parameter f:

$$\frac{\partial}{\partial t}(\rho k) + \nabla \cdot (\rho k \overline{\mathbf{v}}) = \nabla \cdot \left[\left(\mu + \frac{\mu_t}{\sigma_k}\right)\nabla k\right] + P_k - \rho(\varepsilon - \varepsilon_0) + S_k \tag{3.26}$$

$$\frac{\partial}{\partial t}(\rho \varepsilon) + \nabla \cdot (\rho \varepsilon \overline{\mathbf{v}}) = \nabla \cdot \left[\left(\mu + \frac{\mu_t}{\sigma_\varepsilon}\right)\nabla \varepsilon\right] + \frac{1}{T_e} C_{\varepsilon 1} P_\varepsilon - C_{\varepsilon 2}\rho\left(\frac{\varepsilon}{T_e} - \frac{\varepsilon_0}{T_0}\right) + S_\varepsilon \tag{3.27}$$

$$\frac{\partial}{\partial t}(\rho \overline{\vartheta^2}) + \nabla \cdot (\rho \overline{\vartheta^2} \overline{\mathbf{v}}) = \nabla \cdot \left[\left(\mu + \frac{\mu_t}{\sigma_{\overline{\vartheta^2}}}\right)\nabla \overline{\vartheta^2}\right] + P_{\overline{\vartheta^2}} - \frac{6\rho\overline{\vartheta^2}\varepsilon}{k} \tag{3.28}$$

$$\nabla \cdot (L^2 \nabla f) - f + P_f = 0 \tag{3.29}$$

Where $\overline{\mathbf{v}}$ is the mean velocity; μ is the dynamic viscosity; P_k, P_ε, $P_{\overline{\vartheta^2}}$ and P_f are production terms; ε_0 is the ambient turbulence value and $C_{\varepsilon 1}$, $C_{\varepsilon 2}$, σ_k, σ_ε and $\sigma_{\overline{\vartheta^2}}$ are user-specified source terms for which further information can be found in STAR-CCM+ User Guide.

SST K-Omega model

The standard k-ω turbulence model was developed in 1988 by Wilcox [30] and then revised on 1998 and again in 2006 to correct some deficiencies present. It is nowadays widely used in the industry, since it produces better results than the k-ε model near-wall region.

It is a two-equation model that solves transport equations for the turbulent kinetic energy k and the specific dissipation rate ω in order to determine the turbulent viscosity μ_t.

$$\mu_t = \rho k T \tag{3.30}$$

Where ρ is the density and T is the turbulent time scale, which has different formulations depending on the sub-model chosen:

$$\frac{\alpha^*}{\omega}, \text{ for the Standard } k\text{-}\omega \text{ model with } \textit{Realizable Scale Option} \text{ deactivated} \tag{3.31}$$

$$\min\left(\frac{\alpha^*}{\omega}, \frac{a_1}{\mathbf{S}F_2}\right), \text{ for the SST } k-\omega \text{ model with } \textit{Realizable Scale Option} \text{ deactivated} \tag{3.32}$$

$$\min\left(\frac{\alpha^*}{\omega}, \frac{C_T}{\sqrt{3}\mathbf{S}}\right), \text{ for the Standard } k-\omega \text{ model with } \textit{Realizable Scale Option} \text{ activated} \tag{3.33}$$

$$\min\left(\frac{1}{\max(\omega/\alpha^*, (SF_2)/a_1)}, \frac{a_1}{\mathbf{S}F_2}\right), \text{ for the SST } k-\omega \text{ model with } \textit{Realizable Scale Option} \text{ activated} \tag{3.34}$$

Where α^* and C_T are model coefficients, $\mathbf{S}$ is the mean strain rate tensor and F_2 is a blending function.

As for the transport equations for the kinetic energy k and the specific dissipation rate ω:

$$\frac{\partial}{\partial t}(\rho k) + \nabla \cdot (\rho k \overline{\mathbf{v}}) = \nabla \cdot \left[(\mu + \sigma_k \mu_t)\nabla k\right] + P_k - \rho\beta^* f_{\beta^*}(\omega k - \omega_0 k_0) + S_k \tag{3.35}$$

$$\frac{\partial}{\partial t}(\rho \omega) + \nabla \cdot (\rho \omega \overline{\mathbf{v}}) = \nabla \cdot \left[(\mu + \sigma_\omega \mu_t)\nabla \omega\right] + P_\omega - \rho\beta f_\beta(\omega^2 - \omega_0^2) + S_\omega \tag{3.36}$$

Where $\overline{\mathbf{v}}$ is the mean velocity; μ is the dynamic viscosity; σ_k and σ_ω are model coefficients; P_k and P_ω are production terms; f_β^* is the free-shear modification factor; f_β is the vortex-stretching modification factor; S_k and S_ω are the user-specified source terms and k_0 and ω_0 are the ambient turbulence values. Further information regarding production and user-specified source terms can be found in STAR-CCM+ User Guide.

Spalart-Allmaras model

The Spalart-Allmaras turbulence model was developed for the aerospace industry, and could be implemented in an unstructured CFD solver, unlike other aerospace models, which made it very popular among this field. The provided results are acceptable for wake, mixing layer and radial jet flows, but the results for plane and round jets are inaccurate. It is also likely to be less suited to flows involving complex recirculation and body forces than two-equation models such as k-ε, k-ω or Reynolds Stress Transport models.

It is a one-equation model that solves a transport equation for the modified diffusivity $\tilde{\nu}$ in order to determine the turbulent viscosity μ_t.

$$\mu_t = \rho f_{v1} \tilde{\nu} \tag{3.37}$$

Where ρ is the density, $f_{\nu 1}$ is a damping function and $\tilde{\nu}$ is the modified diffusivity.

As for the transport equation for the modified diffusivity $\tilde{\nu}$:

$$\frac{\partial}{\partial t}(\rho\tilde{\nu}) + \nabla \cdot (\rho\tilde{\nu}\overline{\mathbf{v}}) = \frac{1}{\sigma_{\tilde{\nu}}}\nabla \cdot \left[(\mu + \rho\tilde{\nu})\nabla\tilde{\nu}\right] + P_{\tilde{\nu}} + S_{\tilde{\nu}} \tag{3.38}$$

Where $\overline{\mathbf{v}}$ is the mean velocity, $\sigma_{\tilde{\nu}}$ is a model coefficient, μ is the dynamic viscosity, $P_{\tilde{\nu}}$ is the production term and $S_{\tilde{\nu}}$ is the user-specified source term.

Reynolds Stress Transport Models

The second approach is known as Reynolds Stress Transport (RST) models. They calculate the components of the specific Reynolds stress tensor $\mathbf{R} = -\mathbf{T_t}/\rho$ by solving their governing transport equations. The results provided by these models are potentially more accurate than Eddy Viscosity Models, since the effects of turbulence anisotropy, streamline curvature, swirl rotation and high strain rates are naturally accounted by their transport equations.

The transport equation for the specific Reynolds stress tensor $\mathbf{R}$ is:

$$\frac{\partial}{\partial t}(\rho\mathbf{R}) + \nabla \cdot (\rho\mathbf{R}\overline{\mathbf{v}}) = \nabla \cdot \mathbf{D} + \mathbf{P} + \mathbf{G} - \frac{2}{3}\rho\mathbf{I}\gamma_M + \overline{\phi} + \overline{\varepsilon} + \mathbf{S_R} \tag{3.39}$$

Where ρ is the density, $\overline{\mathbf{v}}$ is the mean velocity, $\mathbf{D}$ is the Reynolds stress diffusion, $\mathbf{P}$ is the turbulent production, $\mathbf{G}$ is the buoyancy production, $\mathbf{I}$ is the identity tensor, γ_M is the dilatation dissipation, $\overline{\phi}$ is the pressure strain tensor, $\overline{\varepsilon}$ is the turbulent dissipation rate tensor and $\mathbf{S_R}$ is the user-specified source. Further information regarding specific terms can be found in STAR-CCM+ User Guide.

Regarding the turbulent dissipation rate tensor, it is formulated as follows:

$$\overline{\varepsilon} = \frac{2}{3}\varepsilon\mathbf{I} \tag{3.40}$$

Therefore, seven equations must be solved, six for the Reynolds stresses and one for the isotropic turbulent dissipation ε. This, compared to two-equation models as k-ε or k-ω, is much more expensive in terms of computational efforts.

Chapter 4

CFD Model

In this chapter, the CFD model and the results of the different simulations are presented. All the geometries were designed on ANSYS SpaceClaim and the different cases were simulated on STAR-CCM+.

4.1 Geometry

The geometry of the case is a reproduction of the flow domain of the experimental facility that Dr. Ylönen used for his research. Hence, that is a 4x4 square lattice rod bundle in which rods have a diameter of 25 mm and a separation between centres of 34 mm. Altogether, they form a 16 sub-channel geometry, in which there are 4 central sub-channels, 8 single-wall contact sub-channels and 4 double-wall contact sub-channels. The hydraulic diameter (D_h) of the geometry is 30.39 mm.

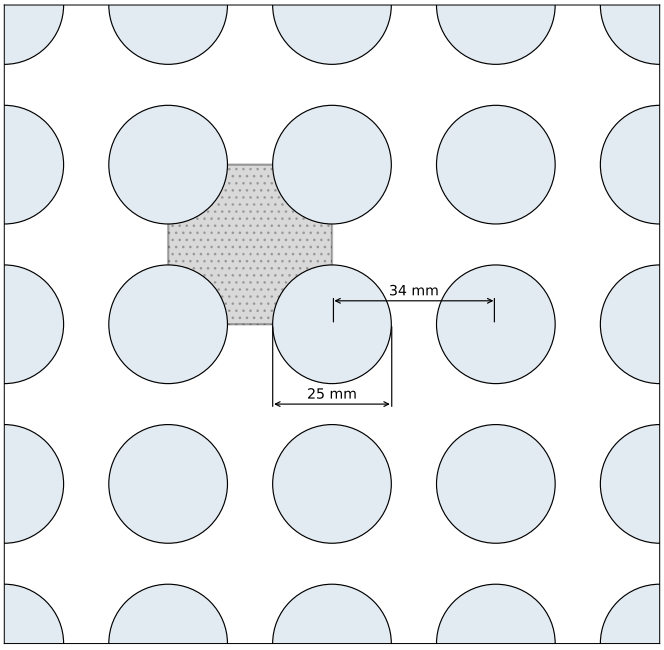

Figure 4.1: Planar view of bare bundle geometry. The grey area symbolises a sub-channel.

It is important to highlight that simulations for the bare bundle case were performed. The geometry used for these simulations is a 1800 mm long channel without obstacles. In the streamwise direction, the full geometry is characterized by its different parts:

- **Part 0** (from the channel inlet till the injector point): this part is a pure extrusion of the bare bundle 2D geometry where the flow develops.

- **Part 1** (from the injector till the front edge of the spacer body): in this part, the tracer is released, but there are still no flow obstacles.

- **Part 2** (from the front edge till the tips of the mixing vanes): the spacer body is placed in this part, in case there is one. Actually, this part was bigger in the simulation, since volumetric margins at the beginning and the end of the spacer body were added in order capture the flow effects before and after the spacers.

- **Part 3** (the rest): this part has no flow obstacles inside, and it is where the different measuring planes positioned.

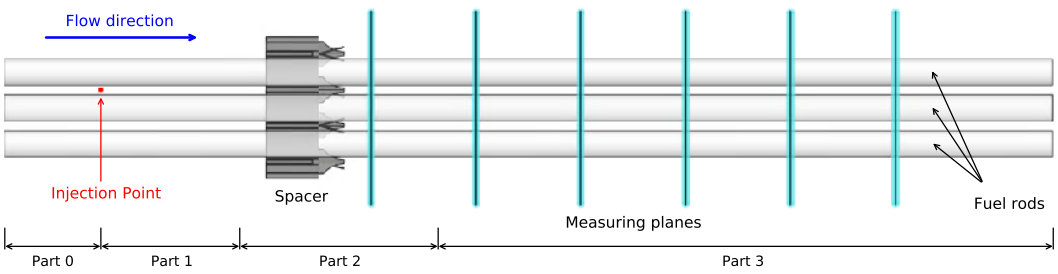

Figure 4.2: Axial view of bare bundle geometry. Only the central fuel rods are shown.

The total length of the experimental rod bundle is 2465 mm, but the simulations took place in a shorter space to save computational time.

4.2 Bare bundle case

4.2.1 Physical models - Boundary conditions

The lack of any obstacles in the flow domain made the bare bundle case a good environment to start working on the project. The geometrical conditions allow the flow to develop fully, reason why it was possible to simplify the domain to a thin slice of the bare bundle.

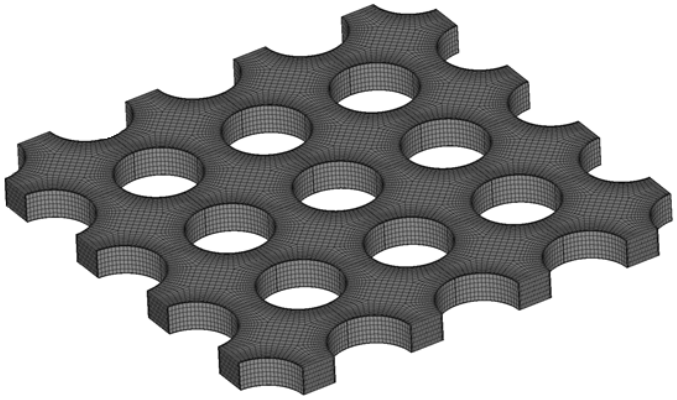

Figure 4.3: Slice of the bare bundle used for this set of simulations.

Figure 4.4 represents the velocity distribution along a line parallel to the z axis placed in the centre of a sub-channel not in contact with the wall. The inlet velocity field of this simulation was a constant value of 0.8 m/s. Figure 4.4 shows how the flow develops at some point near the tracer injection, moment in which it can be categorised as fully-developed flow.

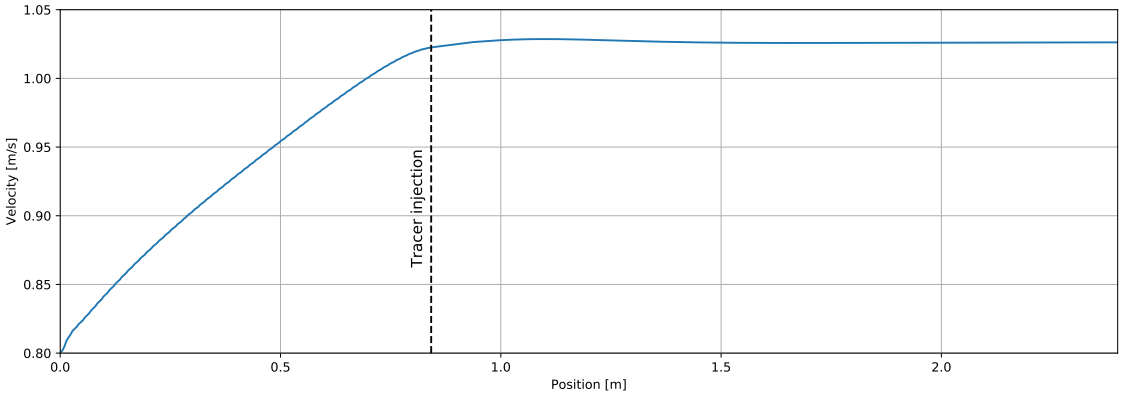

Figure 4.4: Velocity magnitude along z axis in the centre of a sub-channel.

Different steady simulations were done in order to analyse the results obtained from different meshes and turbulence models. For each of these cases, a slice of 0.01 m was modelled, in which the front and back faces were connected through a *Fully-Developed translational periodic* interface. Only the mass-flow inlet with a value of 8.49829 kg/s was set as boundary condition. This is the mass-flow rate necessary for the rod bundle to adapt a bulk velocity of 0.8 m/s, and the one used in the experiment.

4.2.2 Mesh sensitivity analysis

For all the simulated cases, directed hexahedral meshes with three different base sizes on x and y directions were used. This type of mesh was selected for three reasons: due to the lack of spacers in the flow domain, the geometry is simple. Hence, the mesh does not need to adapt to complex geometries and shapes; second, this type of mesh induces few numerical errors compared to other mesh types, since it provides good orthogonal quality and skewness values, among other mesh characteristics; last but not least, the number of cells is drastically reduced compared to other mesh types such as tetrahedral.

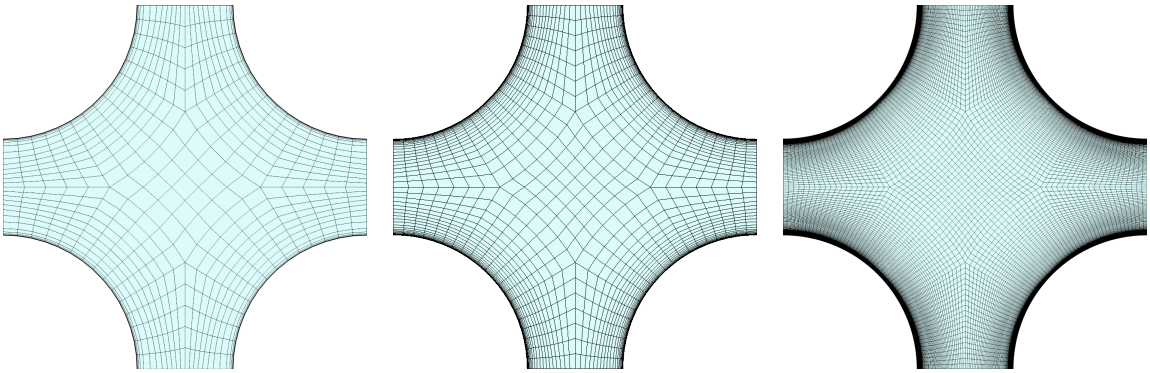

(a) Coarse hexahedral mesh. **(b)** Medium hexahedral mesh. **(c)** Fine hexahedral mesh.

Figure 4.5: The three different base sizes for hexahedral type of mesh in a sub-channel.

	Coarse Mesh	Medium Mesh	Fine Mesh
Number of cells (M) [-]	0.19	0.48	2.0
Cell volume [mm^3]	2.807	0.989	0.201

Table 4.1: Parameters of the different hexahedral-trimmed meshes.

In order to compare the results of the different meshes, the velocity distribution along a line is provided. This probe line, shown in figure 4.6, is placed in the centre of a sub-channel not in contact with the wall.

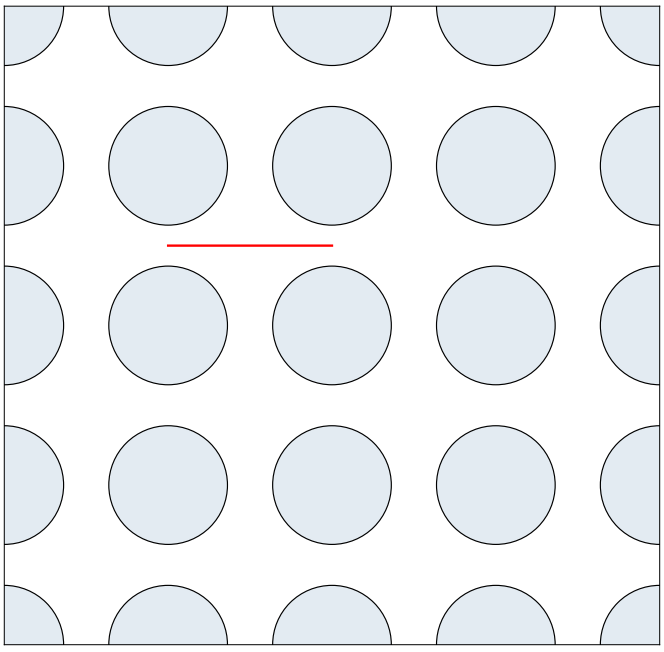

Figure 4.6: Planar view of the geometry with probe line in red.

For the three cases, V^2F k-ε turbulence model is used. The results of the simulations and the experimental data are shown in figure 4.7.

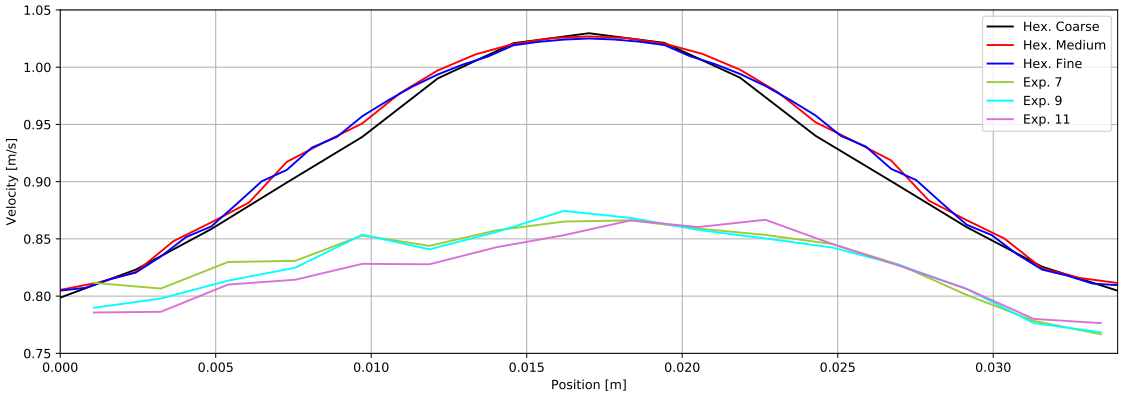

Figure 4.7: Velocity magnitude for different hexahedral meshes along the probe line.

The mesh sensitivity analysis validated the medium type of mesh, which was the one used for the following cases.

4.2.3 Turbulence models analysis

Once the mesh was validated, it was necessary to analyse the sensitivity of the results when the turbulence model used was changed. For this reason, in addition to the V^2F k-ε turbulence model, two more simulations using k-ε and k-ω were performed.

The results were compared using the same methodology described in the mesh sensitivity analysis, and are shown in figure 4.8.

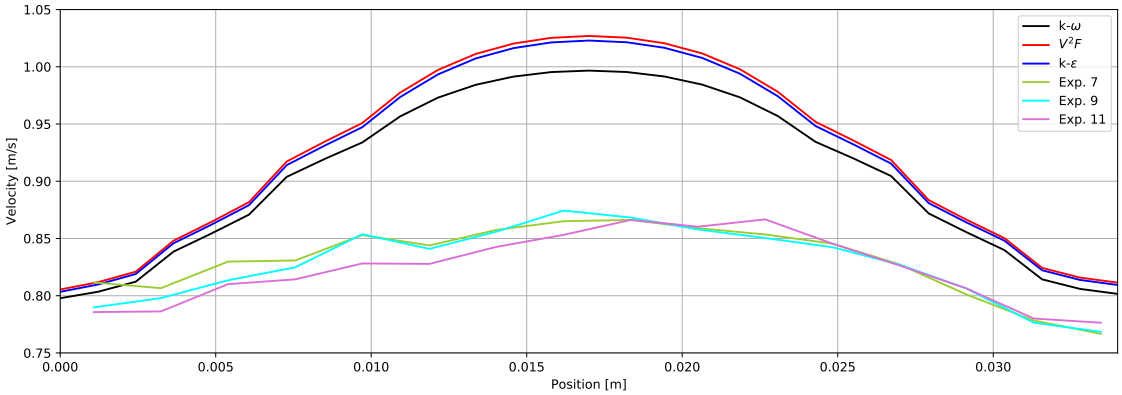

Figure 4.8: Velocity magnitude for different turbulence models along the probe line.

It was also interesting to make a comparison between the CFD results and the experiment data regarding the tracer spread along the z axis. To include the tracer into the model, the *Passive Scalar* option in the model physics, a mathematical object transported by the flow which does not interact with it, was activated. The passive scalar is very useful to understand the dynamics of the stream and it was widely used during the development of this project.

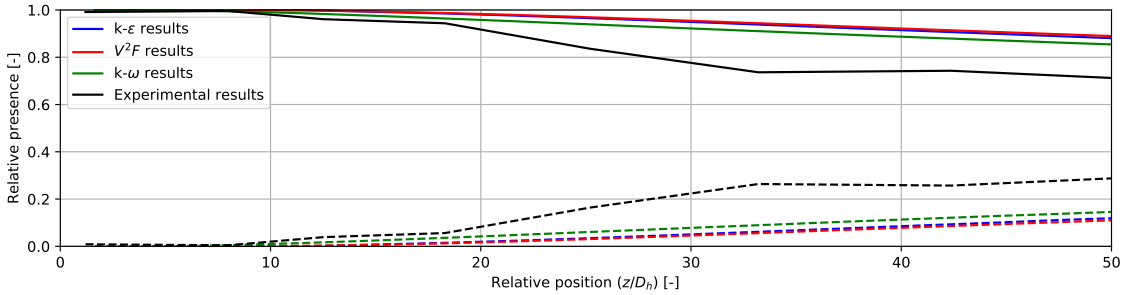

Figure 4.9: Tracer presence along the z axis.

There are two lines for each data source in figure 4.9: the first one represents the amount of tracer that remains inside the sub-channel in which the passive scalar is injected, while the second one is its complementary, the amount ot tracer that leaves the sub-channel and enters one of the adjacent.

For the bare bundle case there was no mixing vane installed and one could think that the flow would be quite undisturbed because of that. However, the flow is highly turbulent, and that turbulence causes the passive scalar to scatter to other sub-channels.

4.2.4 Conclusions

The fully development of the flow made it possible to simulate only a thin slice of the bare bundle, saving a lot of computational time. Mesh sensitivity analysis were performed and a hexahedral mesh convergence was achieved. Different turbulence models were chosen and compared against the data from the experiment. Calculations using a full-length geometry were done to capture the tracer diffusion along the z axis.

None of the simulation results showed a decent enough match with the experimental data for the bare bundle case. There exist different open issues that can be the cause of this phenomenon and which could be the topic for further studies:

- **Surface feature:** the type of the material of the wall can have different behaviours for water, creating strong or not so strong viscous forces near the wall.
- **Wire mesh sensors:** the presence of the wire mesh sensors has an influence on the flow, causing a loss of pressure right before the obstacle. That is something non existing in the CFD model that could explain the different velocity values along the probe line.

4.3 Spacer-vane case

4.3.1 Physical models - Boundary conditions

The bare bundle case was a good first approach to the problem but, in order to perform comparisons for spacer vane cases with the experimental data, it was necessary to build the CFD models with the different kinds of spacers. Due to the presence of these flow obstacles, it was not possible to simplify the case to a thin slice of the bundle, but some computational time was saved due to certain simplifications.

As mentioned before, figure 4.4 shows how the flow was fully developed near the tracer injection. This fact made it possible to omit the previous part of the simulation and use the fully developed velocity field, as well as the specific dissipation rate and turbulent kinetic energy fields as the input for the new simulation.

Figure 4.10: Fluid domain of the simulation with different parts.

It is important to recall the parts classification in section 4.1. As mentioned in the previous paragraph, *part 0* was not simulated. Regarding *part 1*, it was calculated once and the output was taken as the input for the next part. The same input was used for the different spacers, since the flow properties are not influenced by the mixing vanes in *part 1*. *Part 2* and *part 3* were calculated normally and repeated for each case, but they were separated because it is still possible to take advantage of the hexahedral mesh in *part 3*, as can be seen below. The scheme of the different parts of these simulations is shown in figure 4.10.

4.3.2 Mesh sensitivity analysis

In this set of simulations, two different mesh configurations were tested for *spacer 1*, referring to the standard 30° vane distribution type. The first mesh type was a combination between hexahedral and trimmed meshes, while the second one was a pure polyhedral mesh.

Due to the presence of mixing vanes in the geometry, there are clear differences in the velocity distribution of different sub-channels. In order to be able to compare, the measurements took place in a probe line in the middle of the sub-channels for the measuring planes, and this line was moved 2 mm in the x axis in a plain containing the spacer, as shown in figures 4.11a and 4.11b. Since non-negligible lateral velocity is introduced by the mixing vanes, the three components of the velocity were compared.

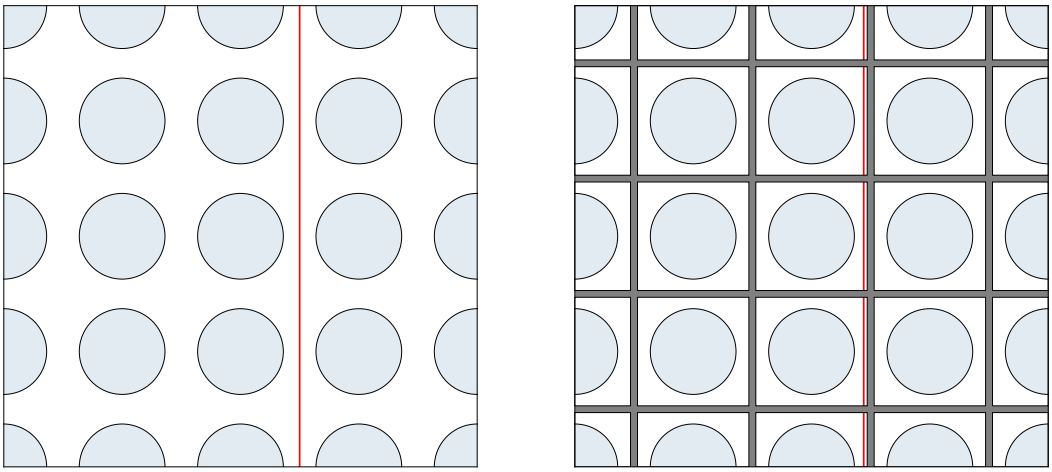

(a) Bare bundle. **(b)** Spacer region.

Figure 4.11: Probe lines used for the comparison of velocity profiles.

Hexahedral-trimmed mesh configuration

In chapter 4.2.2, a mesh sensitivity analysis of the hexahedral configuration was performed. Three different mesh base sizes for X and Y directions were tested. However, this simulation was simulated as *fully developed flow* in a thin slice of the bare bundle geometry. Therefore, the mesh size of Z direction was not tested.

For this mesh configuration, the validated directed medium hexahedral mesh was used in *part 1* and *part 3*, while an automated trimmed mesh was generated for *part 2*. The turbulence model selected to perform the mesh sensitivity analysis was V^2F k-ε. For *part 1* and *part 3*, the mesh sensitivity analysis was performed for three different mesh base sizes on the Z direction only, while for *part 2* it was performed for three different mesh base sizes on X, Y and Z directions.

For the fine mesh in *part 2*, convergence was not achieved in steady state mode, and transient mode was used instead. The time step of this simulation was 3.5E-04 s, obtaining a volume averaged Courant number smaller than 1. The results show that the instantaneous values of the velocity components in different points in this region oscillate slightly. In order to provide comparable values to the rest of the data, the averaged value along time was calculated. All the following results correspond to the averaged variable values.

The resultant mesh sizes are presented in table 4.2 and screenshots of each part of the meshes are shown below.

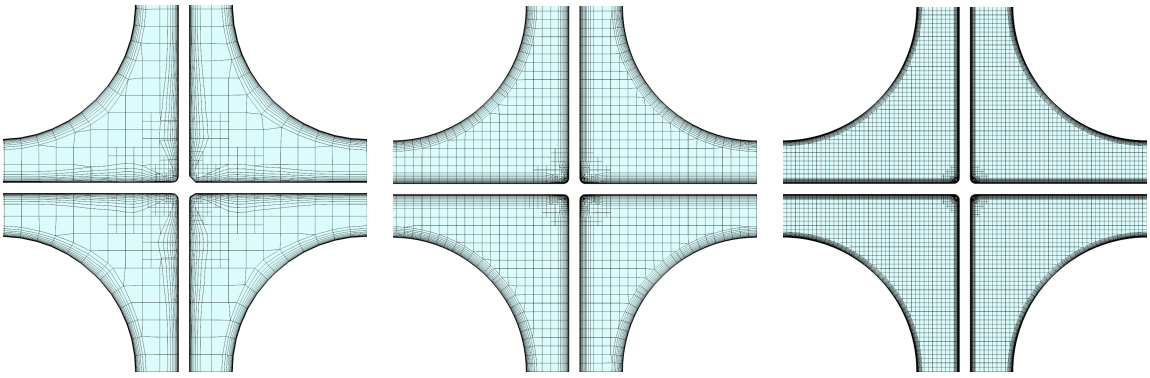

(a) Coarse trimmed mesh. **(b)** Medium trimmed mesh. **(c)** Fine trimmed mesh.

Figure 4.12: The three different base sizes for trimmed type of mesh around the spacer.

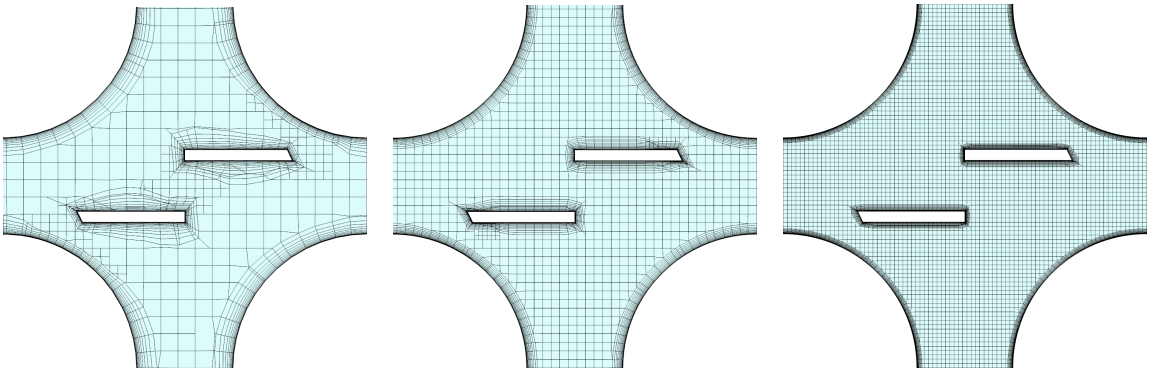

(a) Coarse trimmed mesh. **(b)** Medium trimmed mesh. **(c)** Fine trimmed mesh.

Figure 4.13: The three different base sizes for trimmed type of mesh around the vanes.

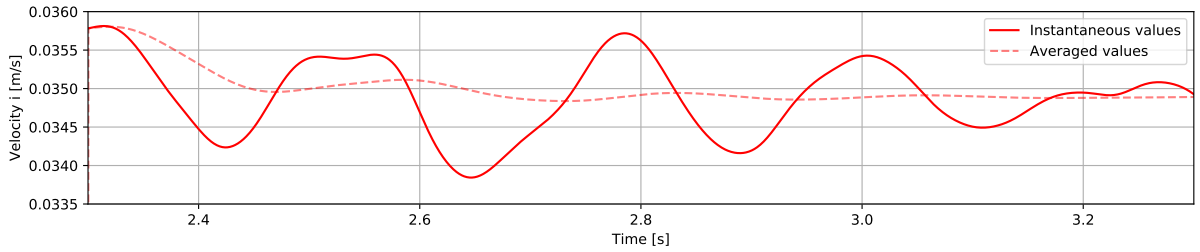

Figure 4.14: Instantaneous vs averaged i component of velocity over time in a point near the mixing vanes.

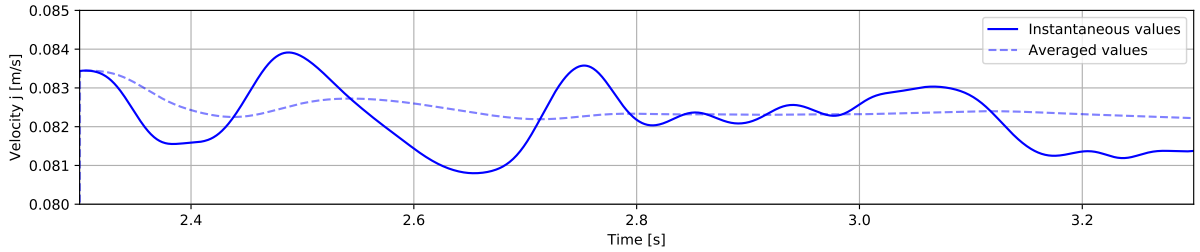

Figure 4.15: Instantaneous vs averaged j component of velocity over time in a point near the mixing vanes.

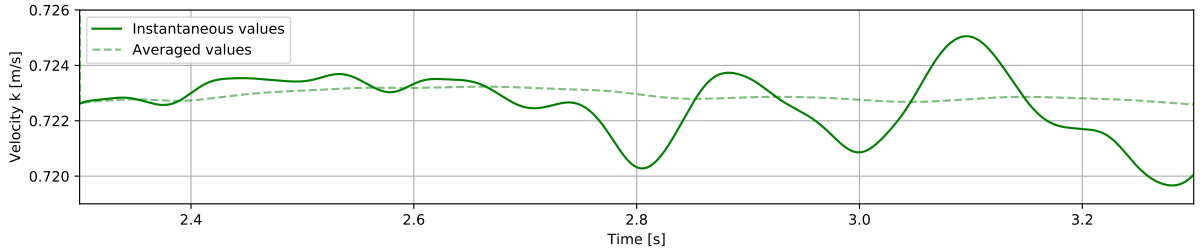

Figure 4.16: Instantaneous vs averaged k component of velocity over time in a point near the mixing vanes.

In *part 2*, three monitoring planes were placed: the first one, cutting the spacer body, as shown in figure 4.11b, the second one, cutting the vanes region, and the third one, near the outlet of the domain.

Some examples of the velocity k component profile along the probe lines comparisons in the trimmed region are shown next, but the full report can be found in section A.1 of the appendix.

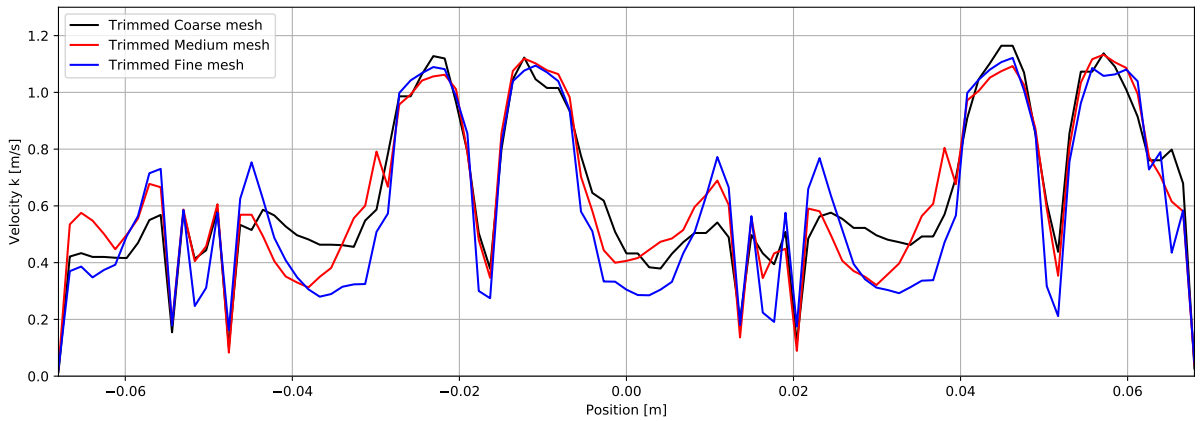

Figure 4.17: k component of velocity along the probe line in a plane cutting the vanes.

	Coarse Mesh	Medium Mesh	Fine Mesh
Number of cells P2 (M) [-]	4.7	21.4	57.6
Cell volume P2 [mm^3]	2.338	0.377	0.058

Table 4.2: Parameters of the different hexahedral-trimmed meshes.

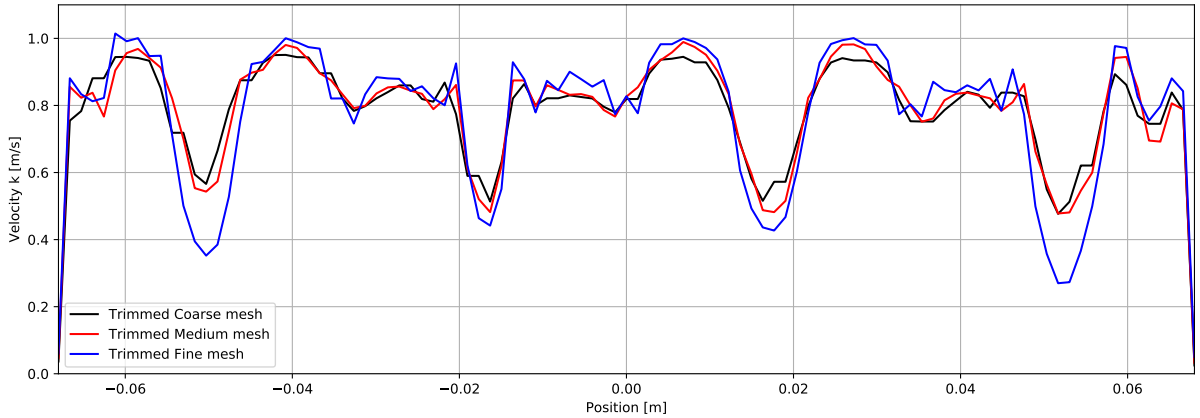

Figure 4.18: k component of velocity along the probe line in a plane near the outlet of the second region.

The results show visible differences between the profiles of the three mesh qualities, especially the fine one. Also, the tracer share was calculated for *part 2* and the results are shown below.

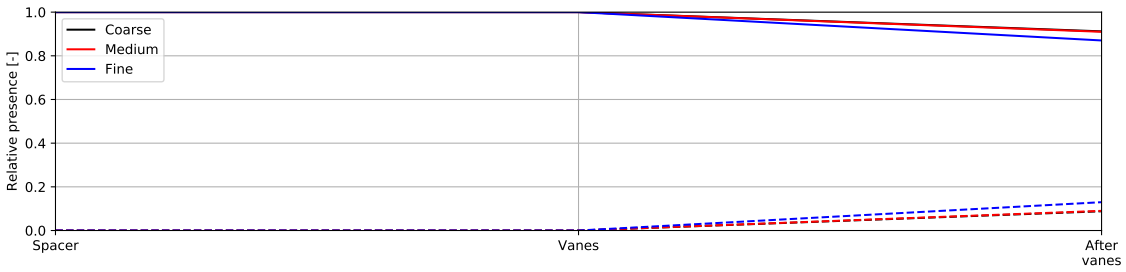

Figure 4.19: Tracer share in *part 2* with hexahedral-trimmed mesh configuration.

The fine case shows a higher mixing rate than the medium and coarse cases in *part 2*. A possible explanation for this fact is that the level of detail in the fine mesh together with the transient solver make it possible to capture the unstable effects present in the flow. These fluctuating components of velocity would enhance lateral mixing between adjacent sub-channels.

Due to resource limitations in terms of time and computational capabilities, the author did not follow this path. However, this is a very interesting point of the thesis that can open the door to a further research in this matter.

To sum up, it is not possible to declare mesh convergence based on these results, since there is not a clear trend present in the velocity profiles or the tracer share. Nevertheless, some results with fine *part 2* mesh will be shown later, just to preliminary peer into the phenomena which could be caught with this methodology.

Polyhedral mesh configuration

Three different directed polyhedral meshes were tested in *part 1* and *part 3*, while three automated polyhedral meshes were generated for *part 2*.

This type of mesh had not been done in previous chapters and, therefore, the base size in X, Y and Z directions were modified. The obtained mesh sizes are shown on table 4.3.

The turbulence model selected for these simulations was k-ω.

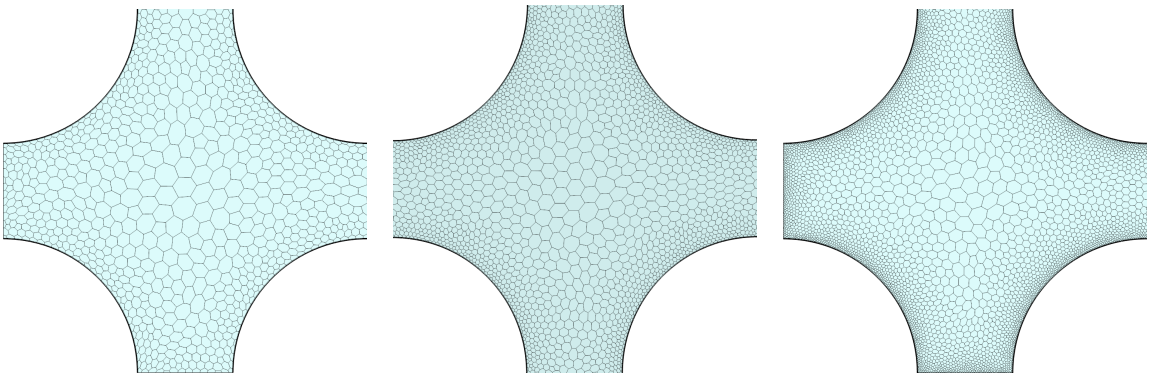

(a) Coarse polyhedral mesh. **(b)** Medium polyhedral mesh. **(c)** Fine polyhedral mesh.

Figure 4.20: The three different base sizes for polyhedral type of mesh around the bare bundle.

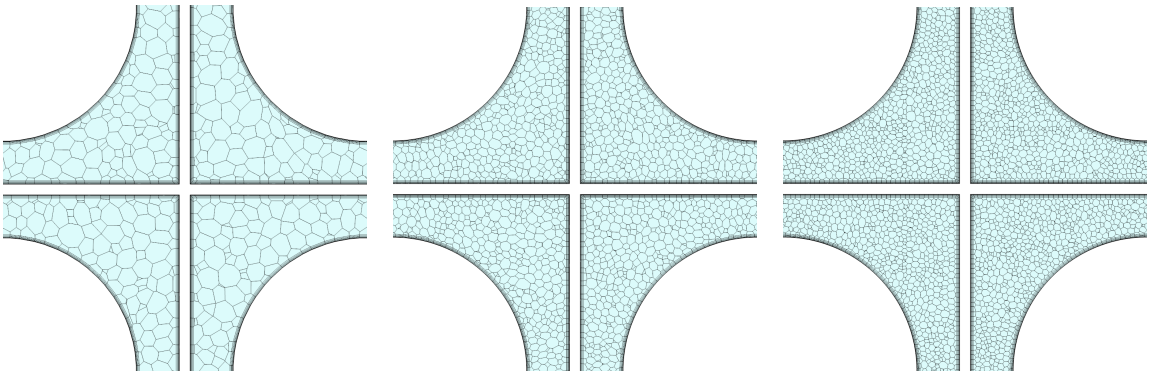

(a) Coarse polyhedral mesh. **(b)** Medium polyhedral mesh. **(c)** Fine polyhedral mesh.

Figure 4.21: The three different base sizes for polyhedral type of mesh around the spacer.

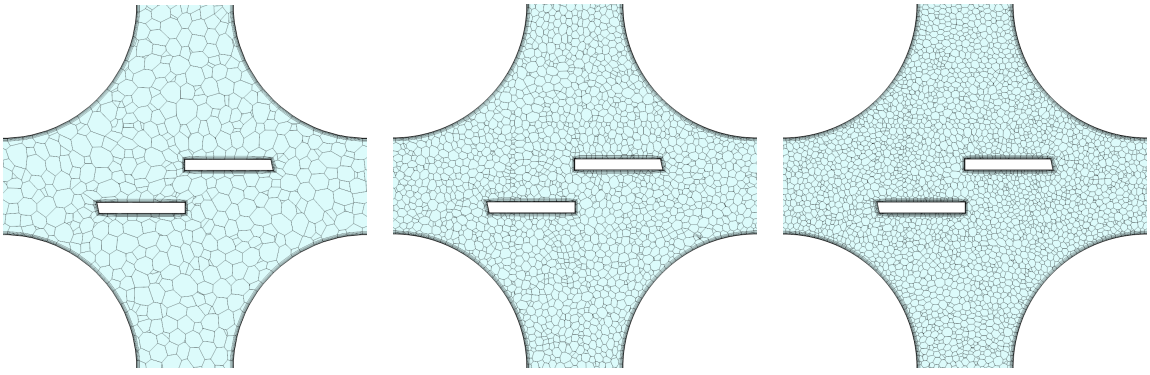

(a) Coarse polyhedral mesh. **(b)** Medium polyhedral mesh. **(c)** Fine polyhedral mesh.

Figure 4.22: The three different base sizes for polyhedral type of mesh around the vanes.

	Coarse Mesh	Medium Mesh	Fine Mesh
Number of cells P2 (M) [-]	2.7	13.6	29.2
Number of cells P3 (M) [-]	8.0	17.6	38.8
Cell volume P2 [mm^3]	2.581	0.342	0.137
Cell volume P3 [mm^3]	2.407	1.408	1.019

Table 4.3: Parameters of the different polyhedral meshes.

In *part 2*, three monitoring planes were placed: the first one, cutting the spacer body, as shown in figure 4.11b, the second one, cutting the vanes region, and the third one, near the outlet of *part 2*. Some examples of the k component of velocity profiles are shown below, but the full report can be found in section A.2 of the appendix.

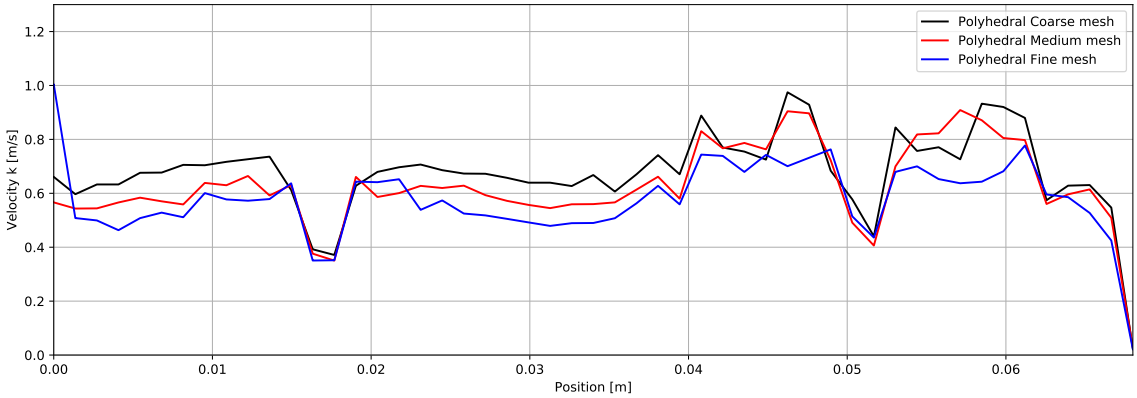

Figure 4.23: k component of velocity along the probe line in a plane cutting the vanes.

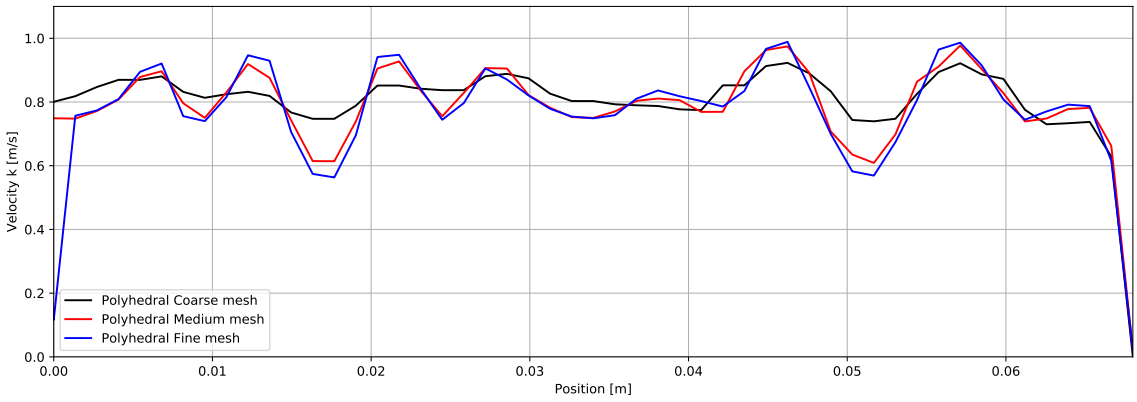

Figure 4.24: k component of velocity along the probe line in a plane near the outlet of the second region.

The velocity profiles in *part 2* show certain convergence trend between the medium and fine case, although there exist some visible differences at some points.

In *part 3*, the monitoring planes shown in figure 4.2 are used to extract the information. Some examples of the velocity components comparisons in this region are shown next, but the full report can be found in section A.3 of the appendix.

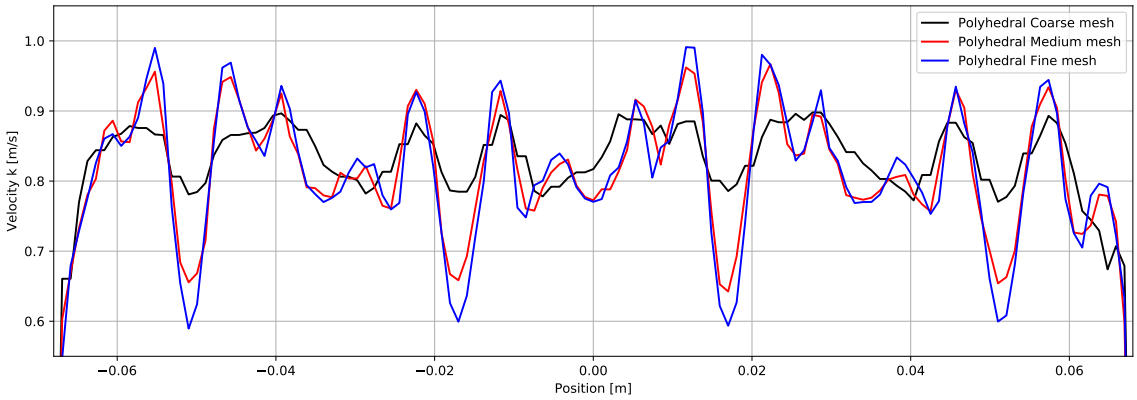

Figure 4.25: k component of velocity along the probe line in a plane 50 mm from the back edge of the spacer body.

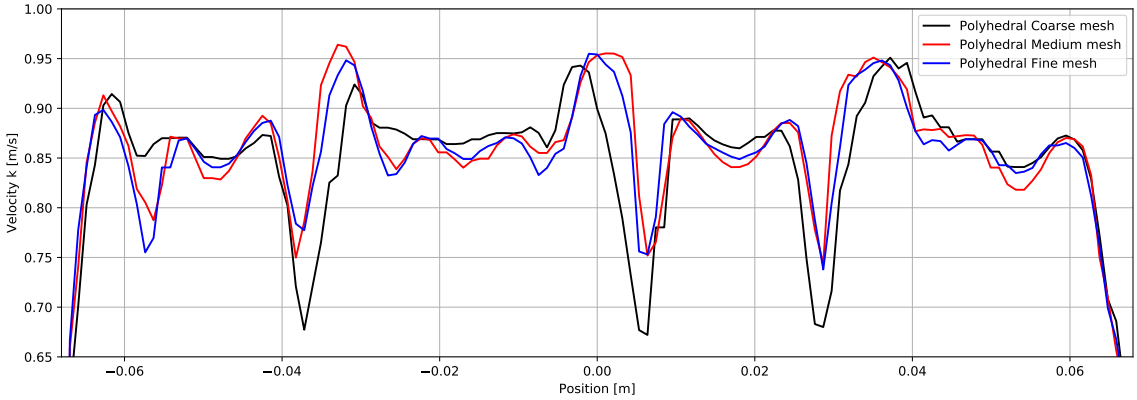

Figure 4.26: k component of velocity along the probe line in a plane 250 mm from the back edge of the spacer body.

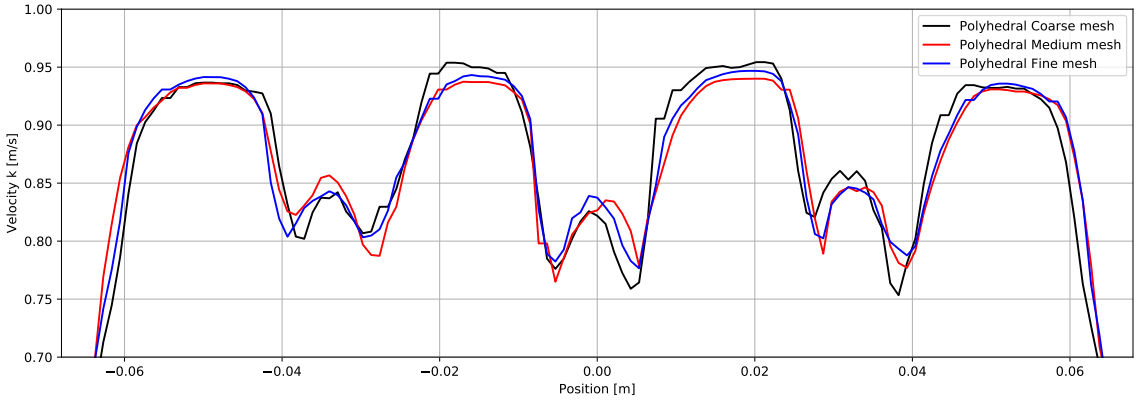

Figure 4.27: k component of velocity along the probe line in a plane 550 mm from the back edge of the spacer body.

The velocity profiles show a roughly acceptable match between the different mesh qualities, from the first plane, 50 mm from the back edge of the spacer body, where the flux is normally better adjusted, to the last plane, 550 mm from the back edge of the spacer body, the most conflictive zone of the region.

As studied in chapter 4.3.2, the tracer share is a useful piece of data to evaluate the quality of a simulation. For the polyhedral configuration, the results in *part 2* and *part 3* are displayed.

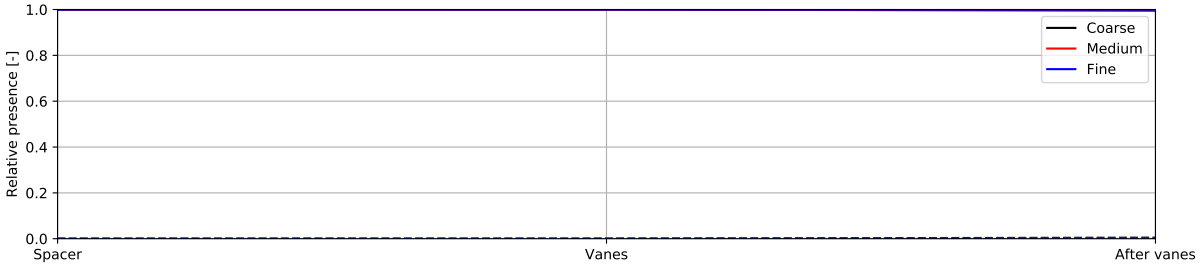

Figure 4.28: Tracer share in *part 2* with polyhedral mesh configuration.

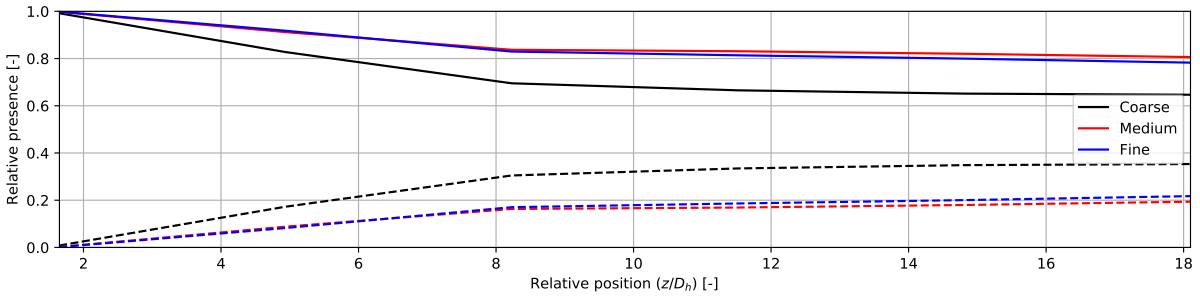

Figure 4.29: Tracer share in *part 3* with polyhedral mesh configuration.

The tracer share results show a good mesh convergence.

It is also interesting to check the swirling aspect of the flow. For that, the angular momentum (Ω), a variable which defines the strength of a swirl, was calculated.

$$\Omega = \sum_{ij} \vec{r_{ij}} \times \vec{v_{ij}} \tag{4.1}$$

Where $\vec{r_{ij}}$ is the position vector from the centre of the swirl and $\vec{v_{ij}}$ is the velocity vector at the point (i, j).

The results of the angular momentum in the injection sub-channel along the monitoring planes are shown in figure 4.30.

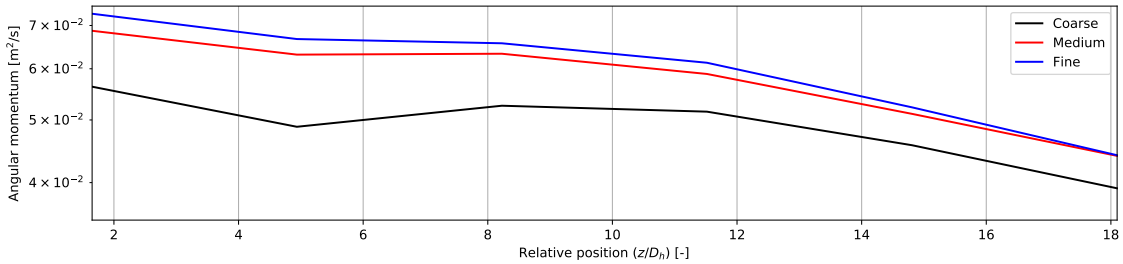

Figure 4.30: Swirl decay comparison with polyhedral mesh configuration.

In this project we are more interested in lateral mixing phenomenon and how the swirls develop along streamwise direction, which are reflected by tracer share and swirl decay rate, respectively. Based on the results above, we can declare mesh independence quite safely with regards to these two parameters.

4.3.3 Turbulence model analysis

After the mesh validations, various simulations with different turbulence models and different mesh types were performed, in order to determine which of them provided the best match with the experimental data.

The chosen turbulence models for this simulations were k-ω and V^{2}F k-ε. That way, four simulations are compared: Hexahedral-Trimmed on k-ω, Hexahedral-Trimmed on V^{2}F k-ε, Polyhedral on k-ω and Polyhedral on V^{2}F k-ε. Once again, the author would like to clarify that the results presented from the hexahedral-trimmed on V^{2}F k-ε simulation are just preliminary, and no mesh independence was yet achieved.

This time, the results were compared to the experimental data. Some examples of the k component of velocity comparison in this region are shown next, but the full report can be found in section A.4 of the appendix.

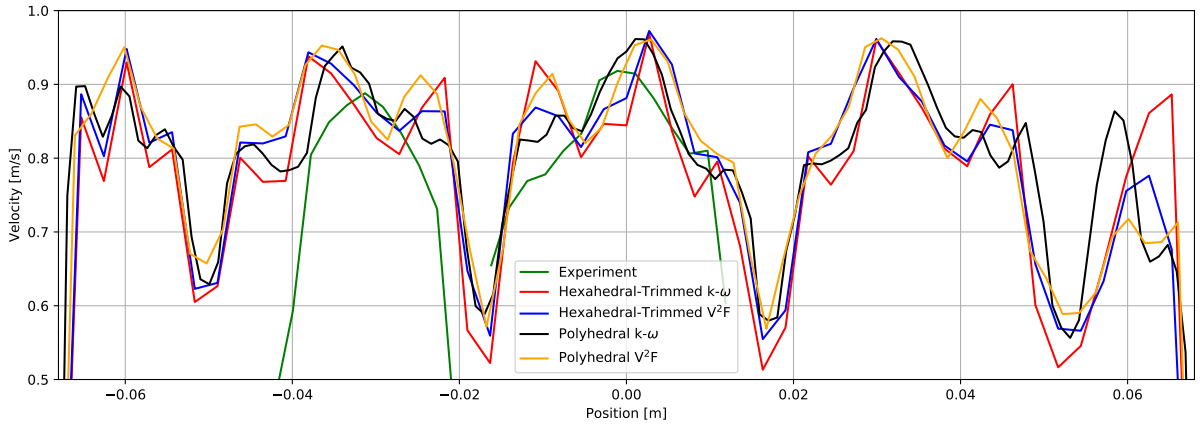

Figure 4.31: k component of velocity along the probe line in a plane 50 mm from the back edge of the spacer body.

At the first monitoring plane, 50 mm from the back edge of the spacer body, the four simulations showed a similar velocity profile. The simulation results roughly matched the experimental data.

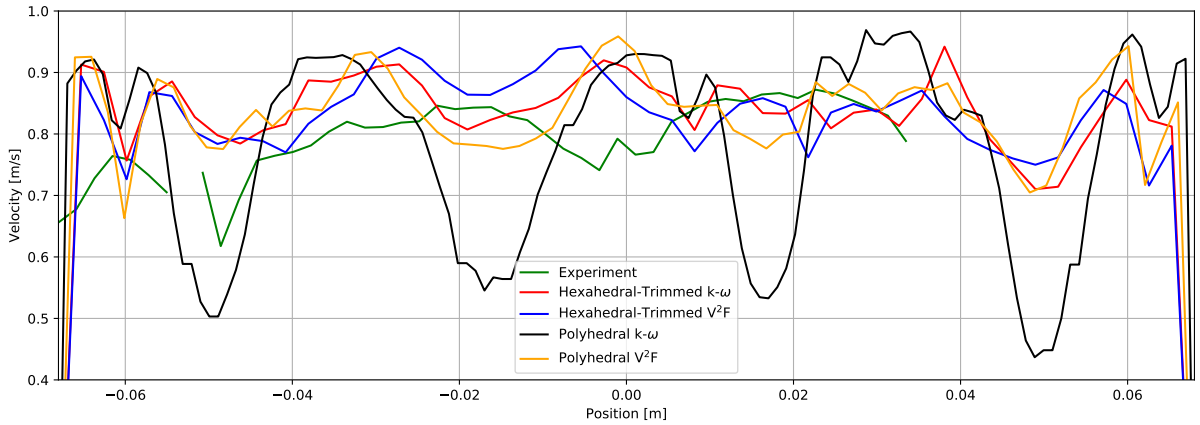

Figure 4.32: k component of velocity along the probe line in a plane 150 mm from the back edge of the spacer body.

On the next monitoring plane, at 150 mm from the back edge of the spacer body, the different numerical models started distinguish from each other. However, this effect eventually got bigger in the following planes with all the simulations, as shown in figure 4.33, which represents the k component of velocity profile along a probe line situated on the last monitoring plane, 550 mm from the back edge of the spacer body.

To sum up, based on the results, it can be concluded immediately that downstream the mixing vanes, where the inertial forces are still dominating, all turbulence models behave in a similar way, while as the flow advances towards the exit, turbulence models show very different predictions.

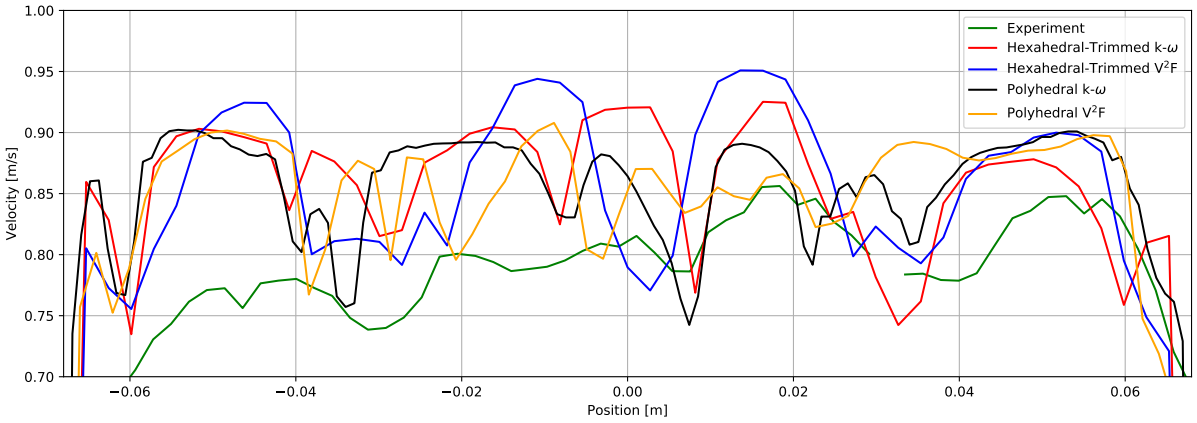

Figure 4.33: k component of velocity along the probe line in a plane 550 mm from the back edge of the spacer body.

The tracer share was compared.

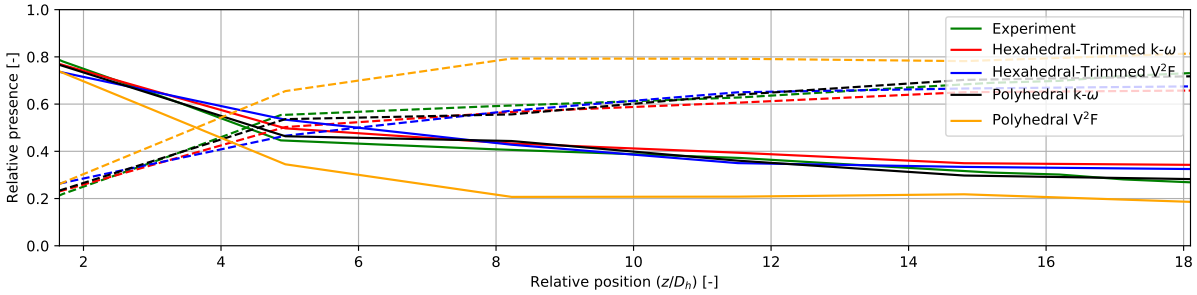

Figure 4.34: Tracer presence along the z axis for the different turbulence models and meshes.

The results show a good match between the experimental data and the polyhedral k-ω simulation. Hexahedral-trimmed k-ω and V^{2}F k-ε are not bad also. Polyhedral V^{2}F k-ε overestimated the mixing too much.

Regarding the angular momentum, the results of the different simulations are shown in figure 4.35. In Dr. Ing. Arto's dissertation, these results were displayed in a logarithmic scale, and an exponential mathematical regression was calculated, since the angular momentum can be estimated with the following exponential correlation reported by McClusky et al. [31]:

$$\Omega(z/D_h) = Be^{-A(z/D_h)} \tag{4.2}$$

Where Ω is the angular momentum and A and B are experimental coefficients. This way, B determines the initial angular momentum, while A represents the swirl decay rate. In this case, the regression is calculated without taking in account the first and last monitoring plane, following the methodology used by Dr. Ing. Arto.

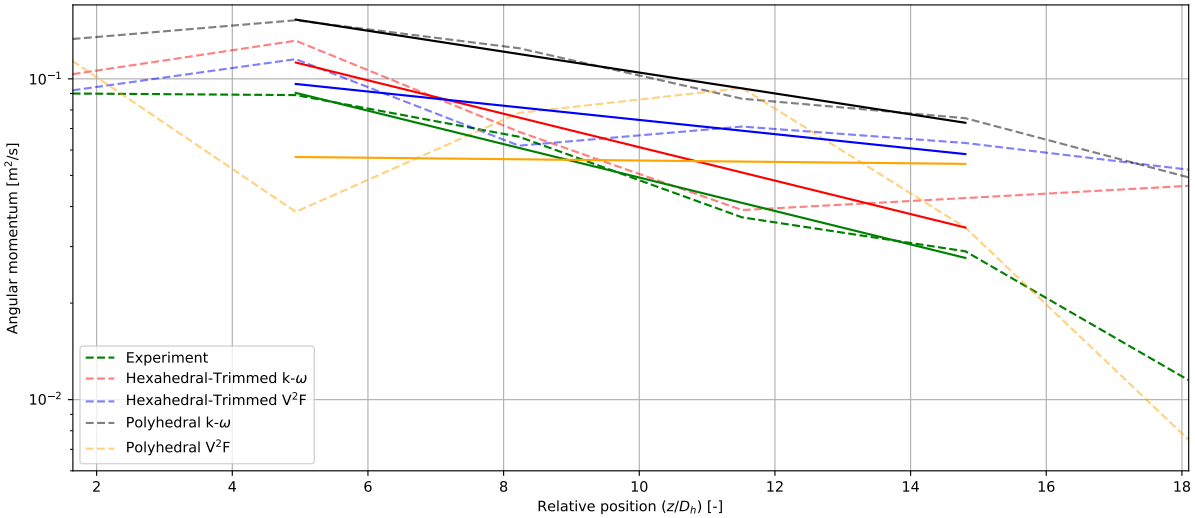

Figure 4.35: Angular momentum along the z axis.

	A	ϵA	ϵ_RA	B	ϵB	ϵ_RB
Hexahedral-Trimmed k-ω	0.120	0.000	0.00%	0.203	0.040	24.34%
Hexahedral-Trimmed V^2F k-ε	0.051	0.069	57.50%	0.124	0.040	24.16%
Polyhedral k-ω	0.075	0.045	37.50%	0.222	0.058	35.47%
Polyhedral V^2F k-ε	0.005	0.115	95.83%	0.059	0.105	64.22%
Experimental results	0.120	-	-	0.164	-	-

Table 4.4: Parameters of the exponential fit for the different turbulence analysis.

The results show certain mismatch between the simulations, in both the initial angular momentum and the swirl decay rate, and it was hard to decide between the polyhedral k-ω and the hexahedral-trimmed V^2F k-ε simulations.

It is also very important to look at the flow structures and how they develop along the channel. 2D lateral velocity profiles are shown below.

In the first monitoring plane, situated at 50 mm from the back edge of the spacer body, the four simulations got a good qualitative match with the experimental data, since the swirl had the same position and rotation. However, the simulations with k-ω turbulence model on polyhedral mesh showed relatively worse results.

In the second monitoring plane, situated at 150 mm from the back edge of the spacer body, the performance of all the simulations except the polyhedral V^2F k-ε case was very good, getting a good match compared to the experimental data.

In the third monitoring plane, placed at 250 mm from the back edge of the spacer body, the hexahedral-trimmed k-ω simulation creates two sub-swirls instead of the only one measured in the experiment. Also, the polyhedral V^2F k-ε shows a clear mismatch in terms of shape.

From the fourth monitoring plane, situated at 350 mm from the back edge of the spacer body, it is very hard to say which simulation has a better match with the experimental data, since none of the cases can reproduce the shape of the swirl perfectly.

In the fifth monitoring plane, whose position is 450 mm from the back edge of the spacer body, the hexahedral-trimmed V^2F k-ε model gets the best match for the data from the experiment. The polyhedral k-ω also performs well, but the vectors in the extremes of the sub-channel do not reproduce well the dynamics of the experimental flow.

The last plane shows a mismatch between the simulations and the experimental data, but the velocity vectors of the V^2F k-ε model are quite similar compared to the experimental ones.

50 mm measurements - Lateral velocity vectors

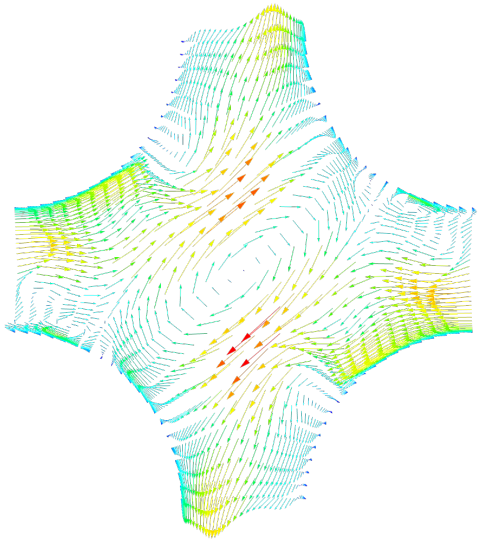

(a) Hexahedral-Trimmed k-ω
v_{max} = 0.5269 m/s

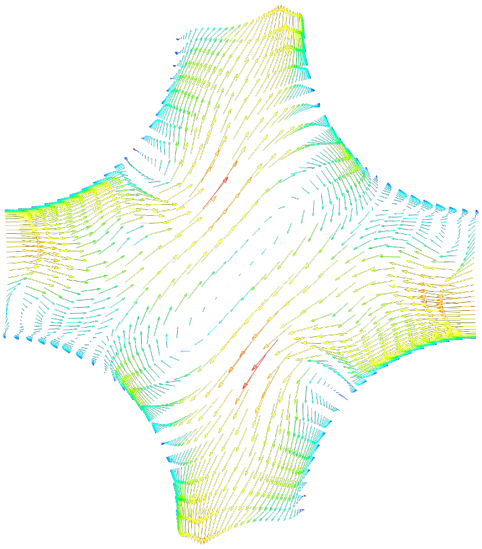

(b) Hexahedral-Trimmed V^{2}F k-ε
v_{max} = 0.4600 m/s

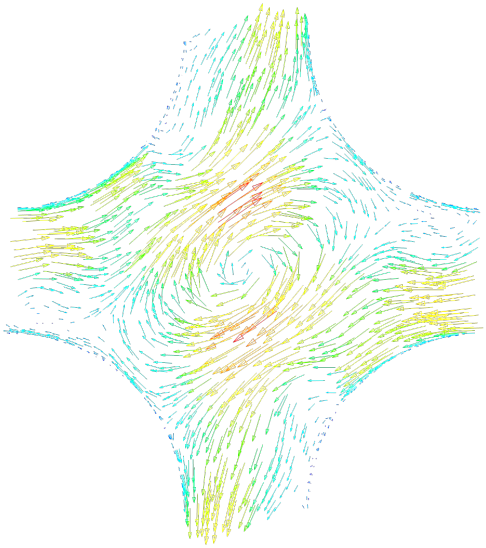

(c) Polyhedral k-ω
v_{max} = 0.5610 m/s

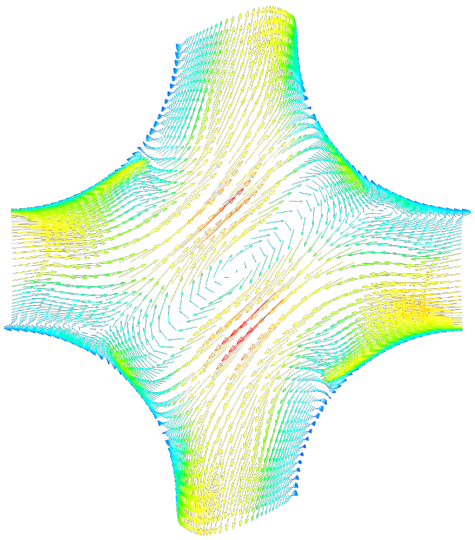

(d) Polyhedral V^{2}F k-ε
v_{max} = 0.4939 m/s

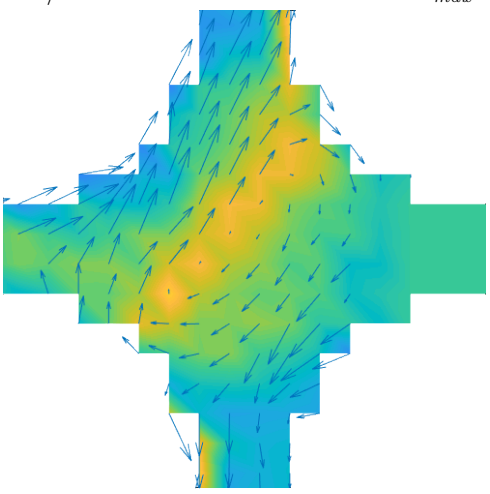

(e) Experimental data

150 mm measurements - Lateral velocity vectors

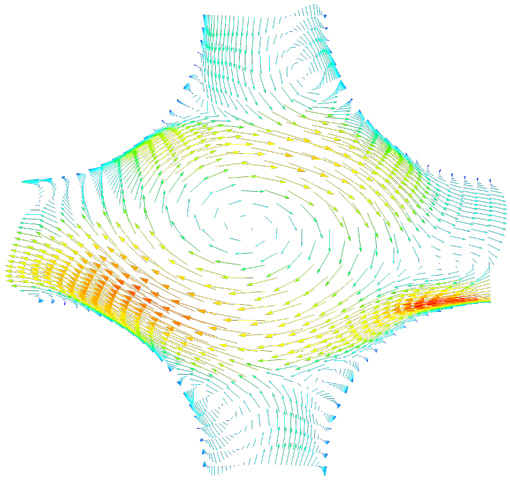

(a) Hexahedral-Trimmed k-ω
v_{max} = 0.4123 m/s

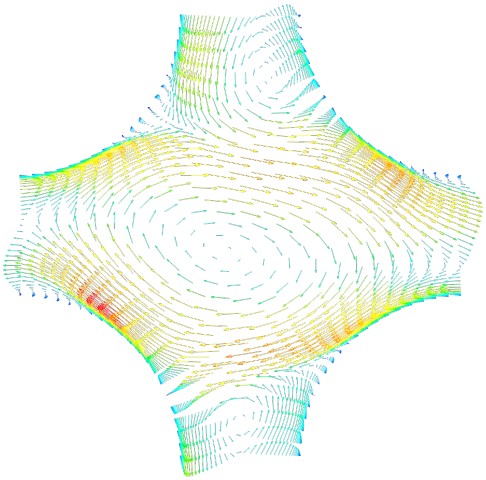

(b) Hexahedral-Trimmed V^{2}F k-ε
v_{max} = 0.3219 m/s

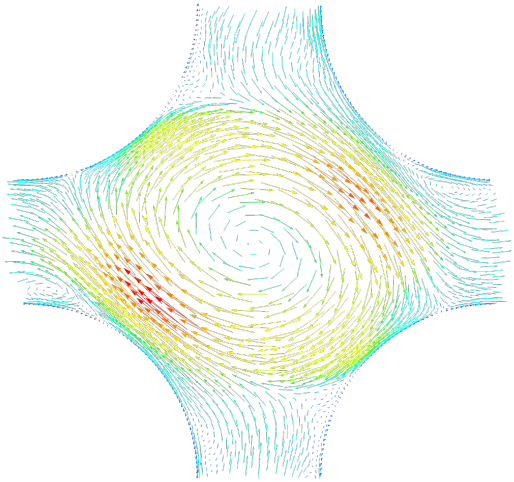

(c) Polyhedral k-ω
v_{max} = 0.4024 m/s

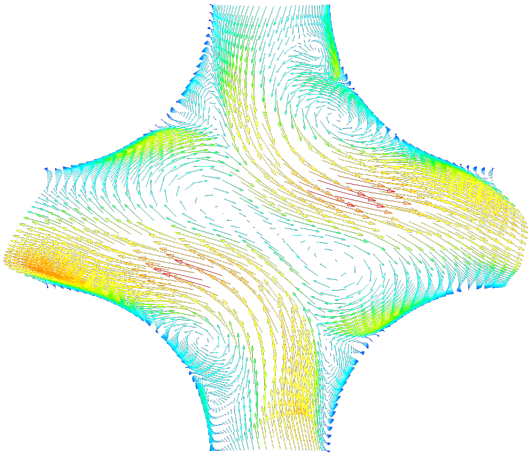

(d) Polyhedral V^{2}F k-ε
v_{max} = 0.3824 m/s

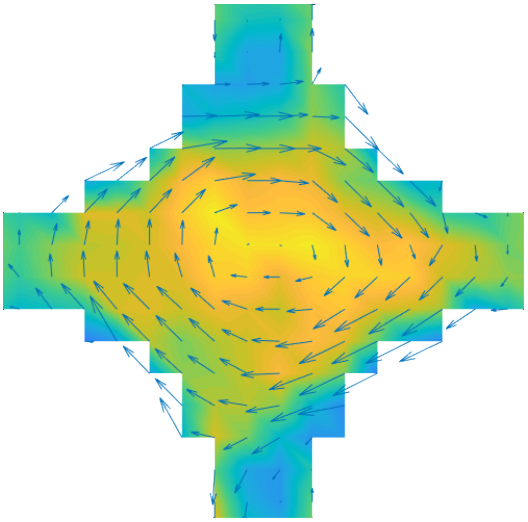

(e) Experimental data

250 mm measurements - Lateral velocity vectors

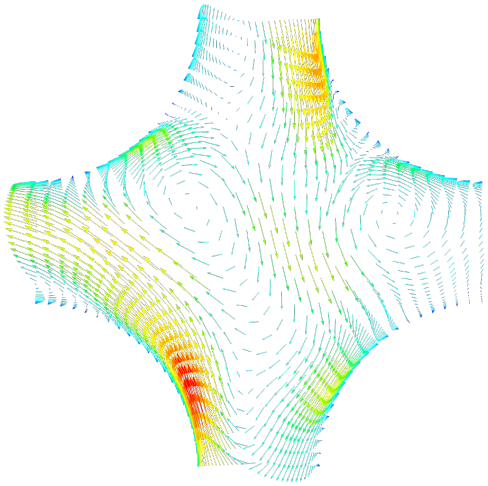

(a) Hexahedral-Trimmed k-ω
v_{max} = 0.3387 m/s

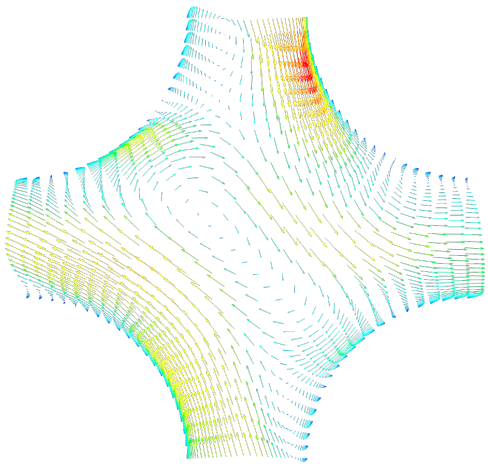

(b) Hexahedral-Trimmed V^{2}F k-ε
v_{max} = 0.2532 m/s

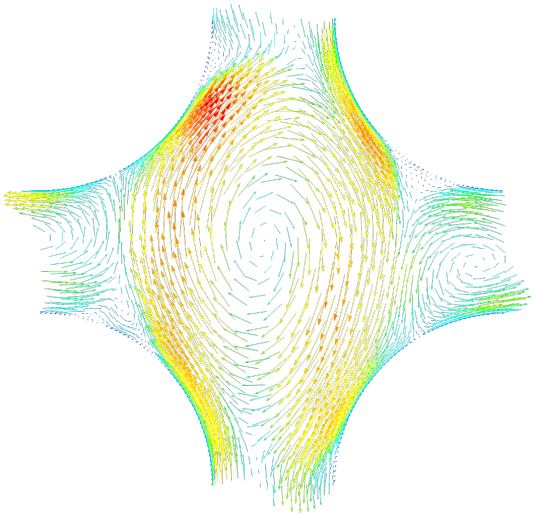

(c) Polyhedral k-ω
v_{max} = 0.3026 m/s

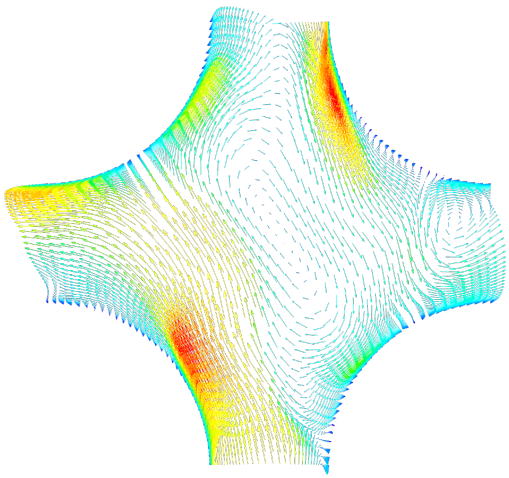

(d) Polyhedral V^{2}F k-ε
v_{max} = 0.3354 m/s

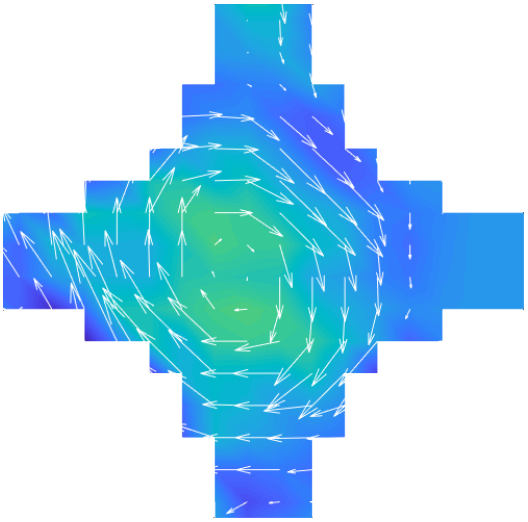

(e) Experimental data

350 mm measurements - Lateral velocity vectors

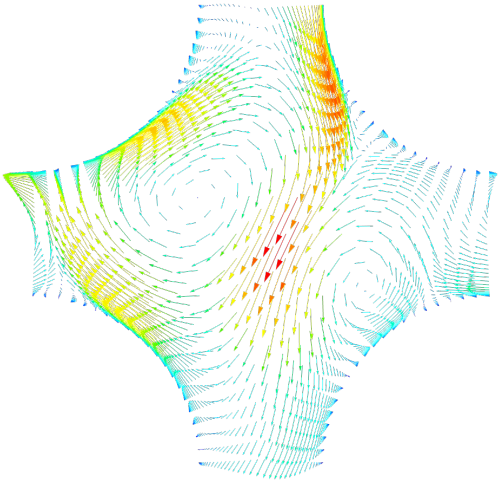

(a) Hexahedral-Trimmed k-ω
v_{max} = 0.2363 m/s

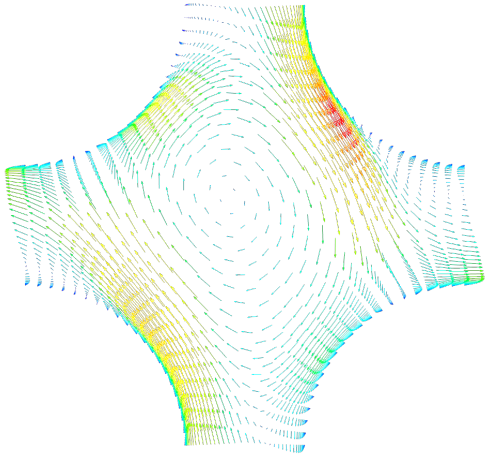

(b) Hexahedral-Trimmed V^{2}F k-ε
v_{max} = 0.2141 m/s

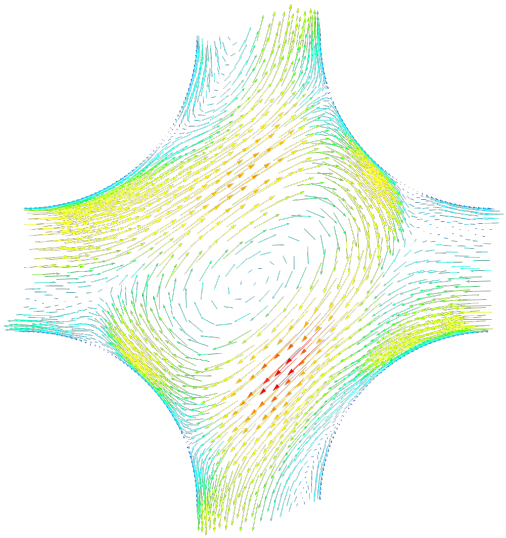

(c) Polyhedral k-ω
v_{max} = 0.2537 m/s

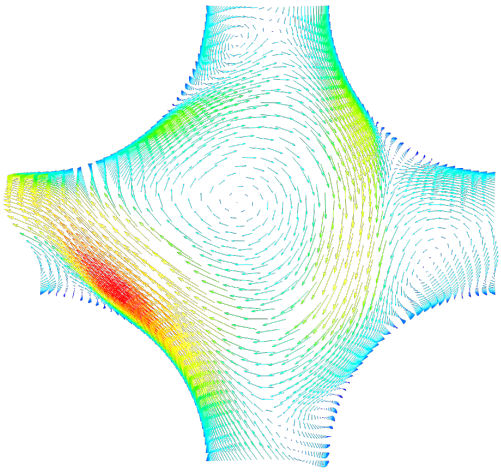

(d) Polyhedral V^{2}F k-ε
v_{max} = 0.3168 m/s

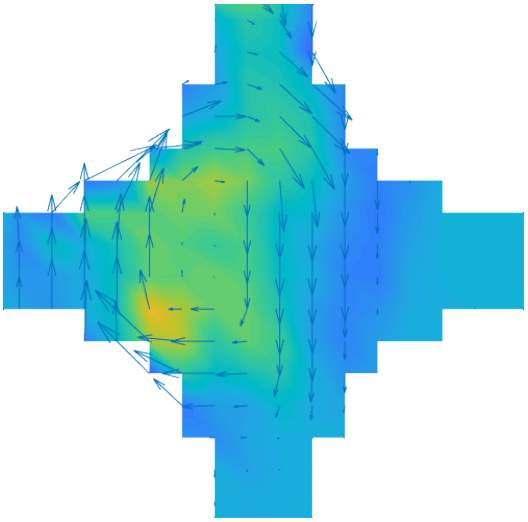

(e) Experimental data

450 mm measurements - Lateral velocity vectors

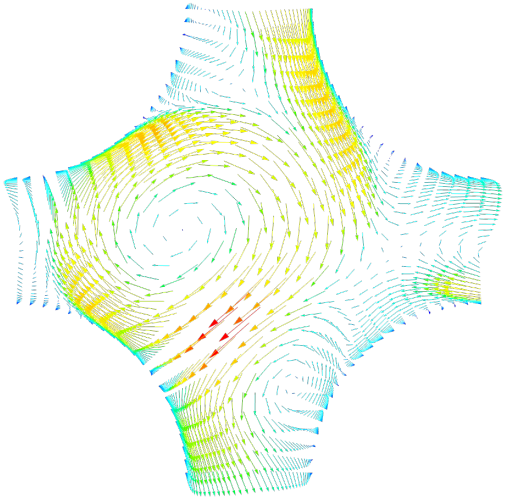

(a) Hexahedral-Trimmed k-ω
v_{max} = 0.1749 m/s

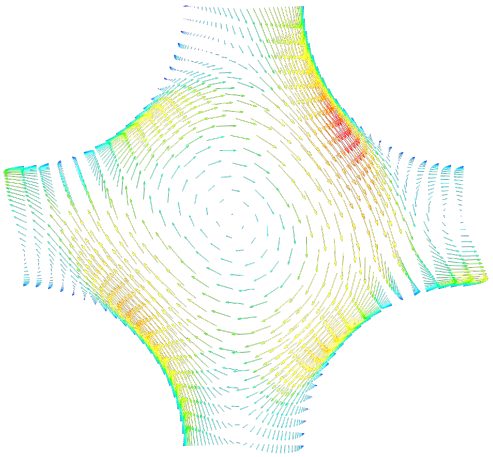

(b) Hexahedral-Trimmed V^{2}F k-ε
v_{max} = 0.1500 m/s

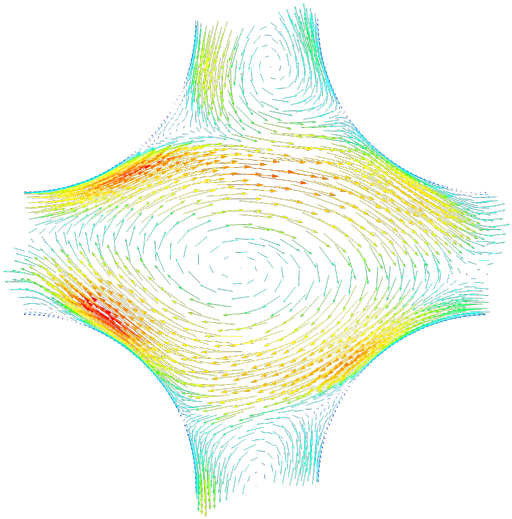

(c) Polyhedral k-ω
v_{max} = 0.1968 m/s

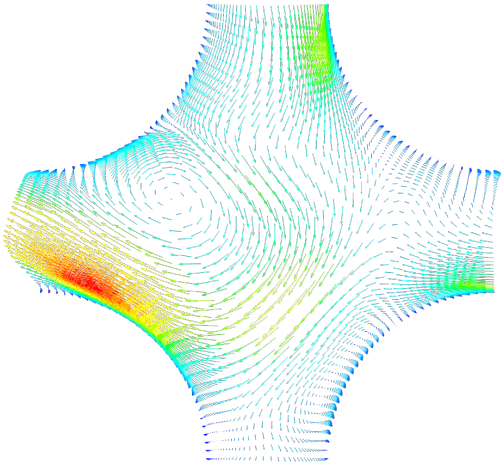

(d) Polyhedral V^{2}F k-ε
v_{max} = 0.2549 m/s

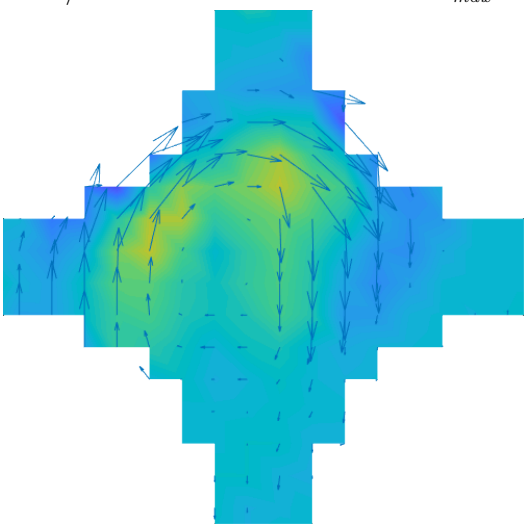

(e) Experimental data

550 mm measurements - Lateral velocity vectors

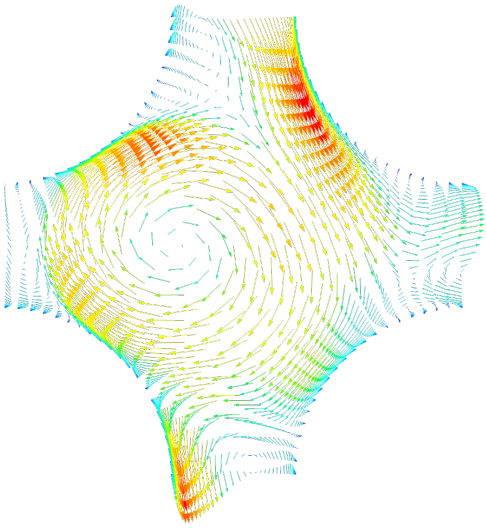

(a) Hexahedral-Trimmed k-ω
$v_{max} = 0.1386$ m/s

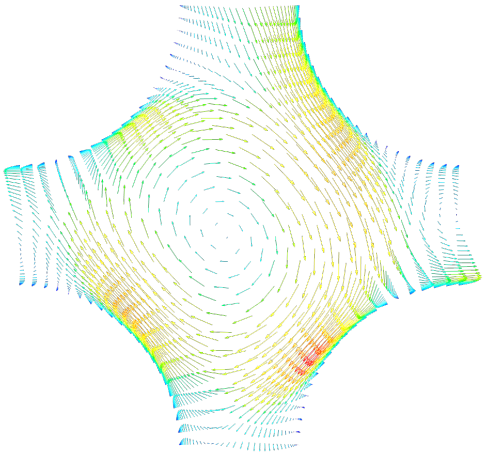

(b) Hexahedral-Trimmed V^{2}F k-ε
$v_{max} = 0.1228$ m/s

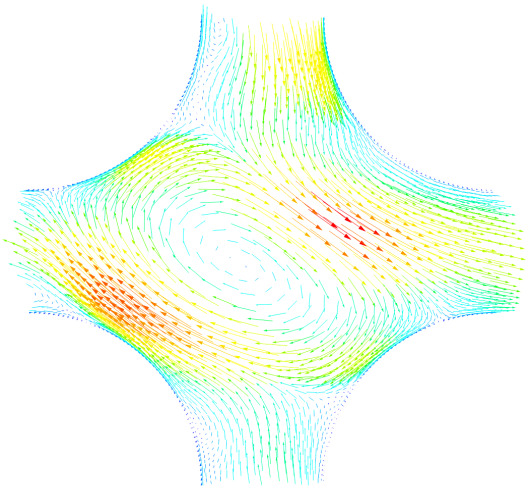

(c) Polyhedral k-ω
$v_{max} = 0.1627$ m/s

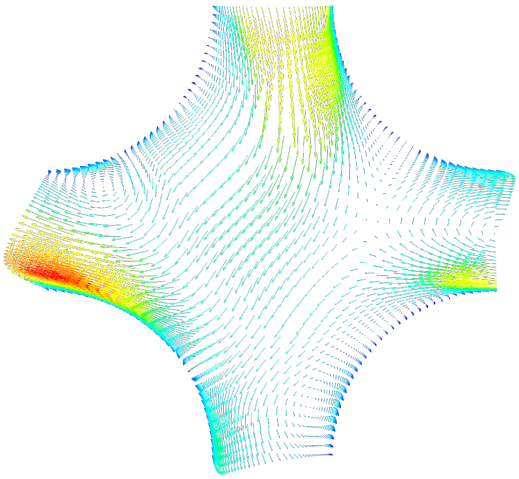

(d) Polyhedral V^{2}F k-ε
$v_{max} = 0.1999$ m/s

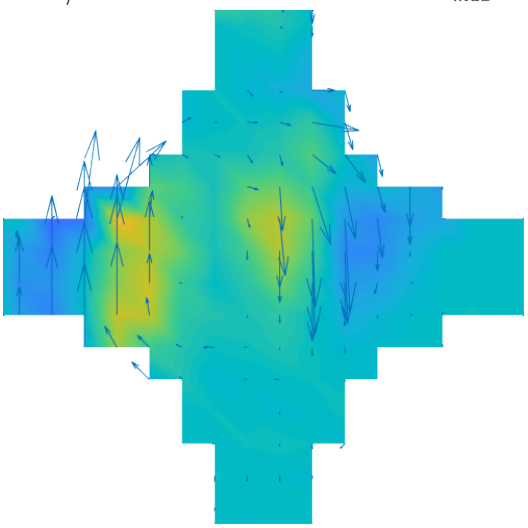

(e) Experimental data

50 mm measurements - Passive scalar contour

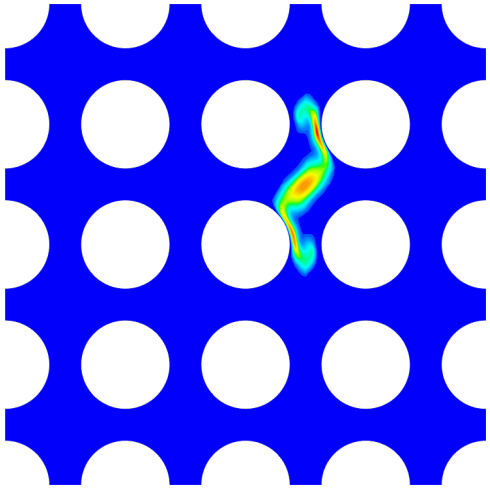

(a) Hexahedral-Trimmed k-ω

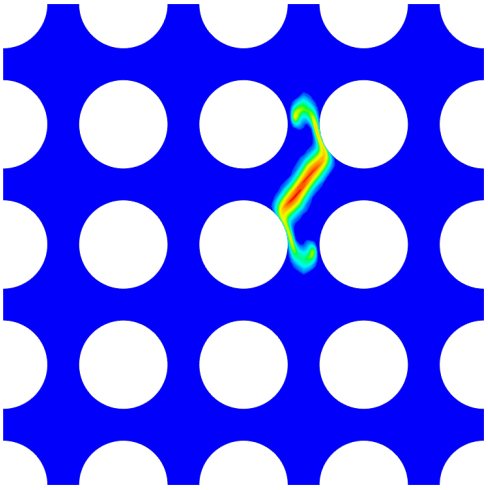

(b) Hexahedral-Trimmed V^2F k-ε

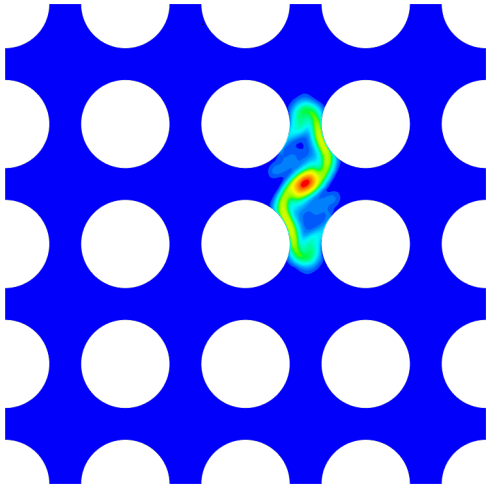

(c) Polyhedral k-ω

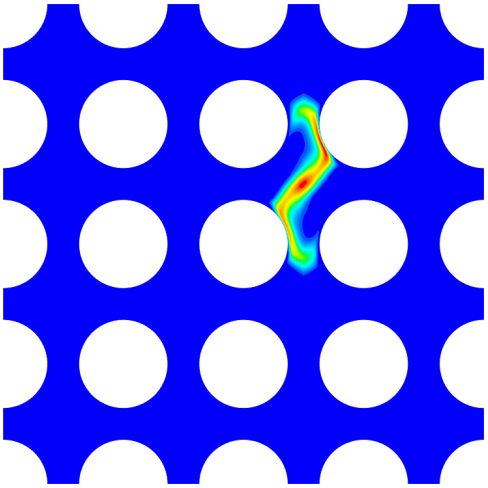

(d) Polyhedral V^2F k-ε

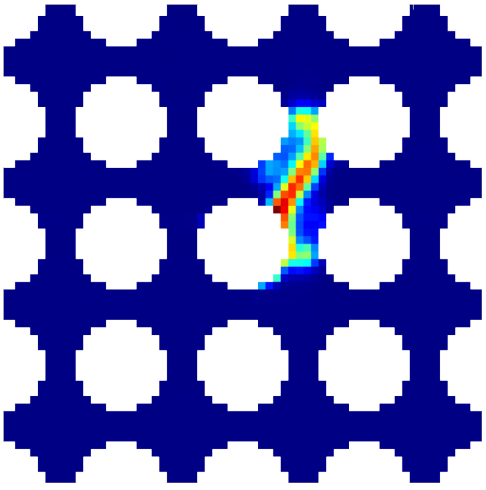

(e) Experimental data

150 mm measurements - Passive scalar contour

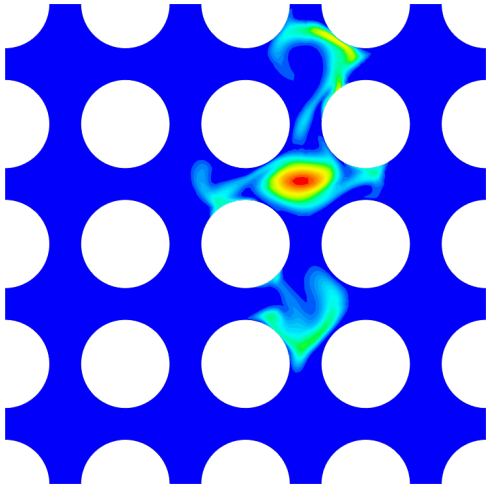

(a) Hexahedral-Trimmed k-ω

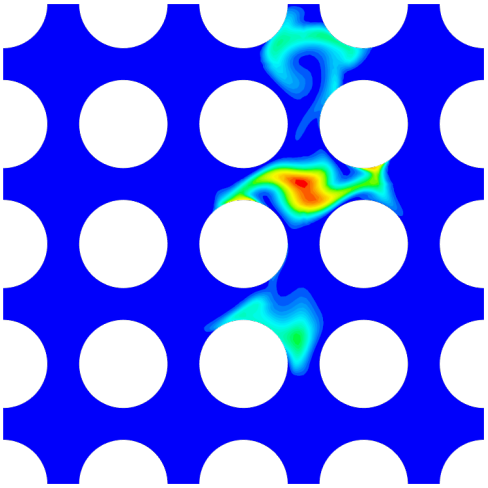

(b) Hexahedral-Trimmed V^2F k-ε

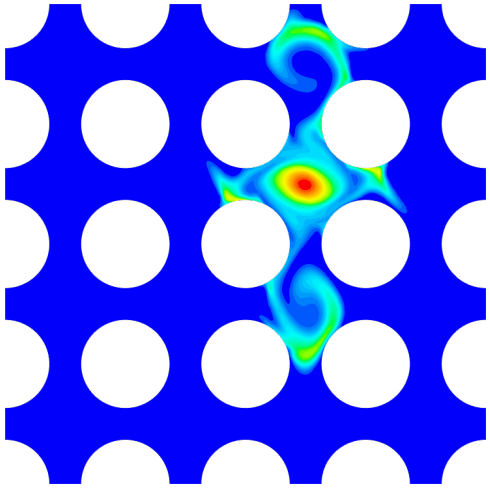

(c) Polyhedral k-ω

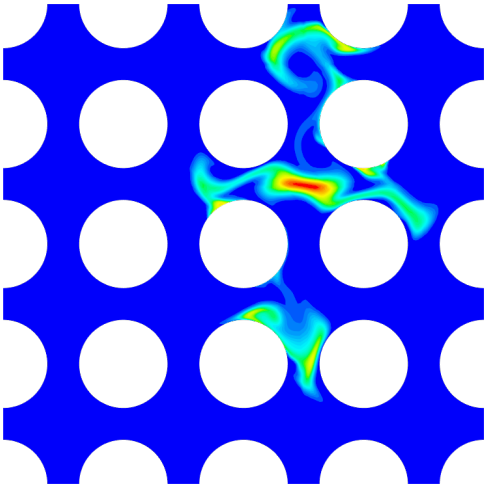

(d) Polyhedral V^2F k-ε

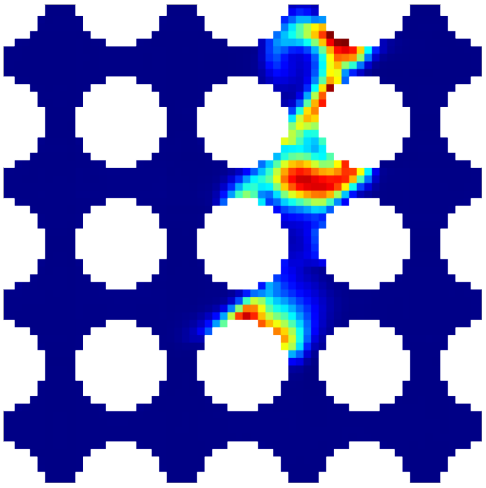

(e) Experimental data

250 mm measurements - Passive scalar contour

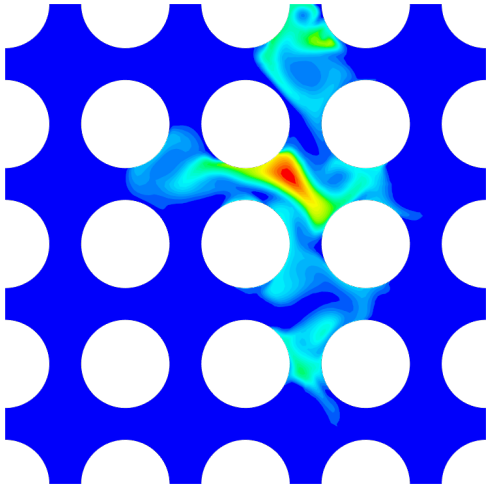

(a) Hexahedral-Trimmed k-ω

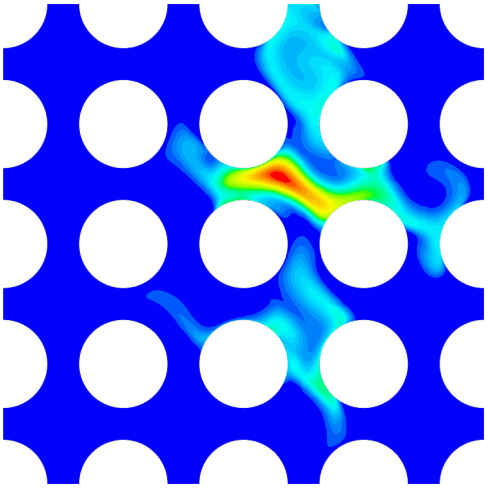

(b) Hexahedral-Trimmed V^2F k-ε

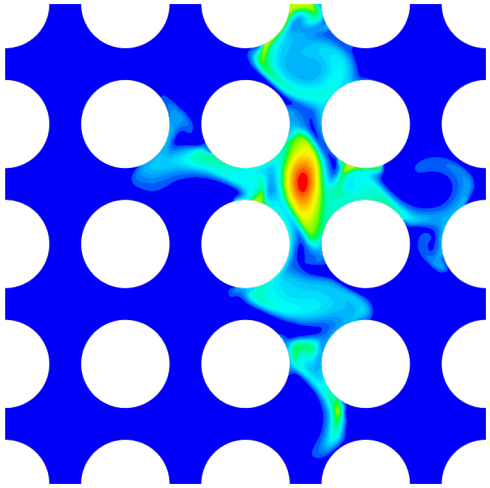

(c) Polyhedral k-ω

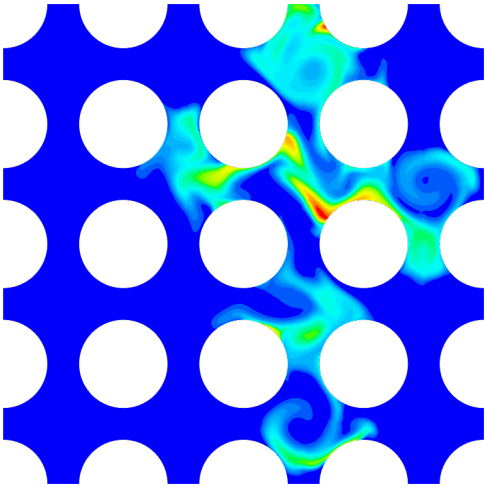

(d) Polyhedral V^2F k-ε

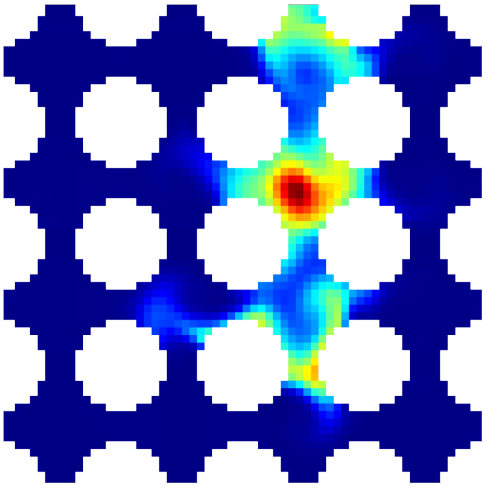

(e) Experimental data

350 mm measurements - Passive scalar contour

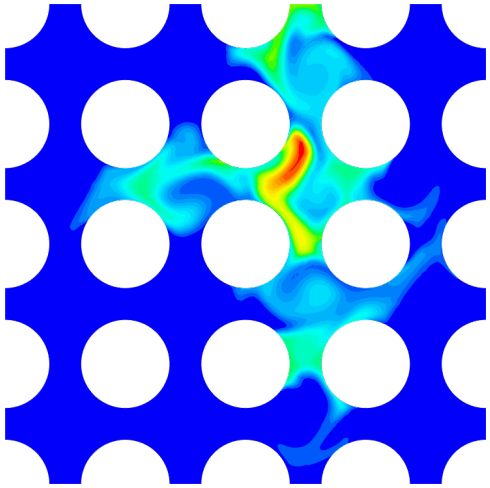

(a) Hexahedral-Trimmed k-ω

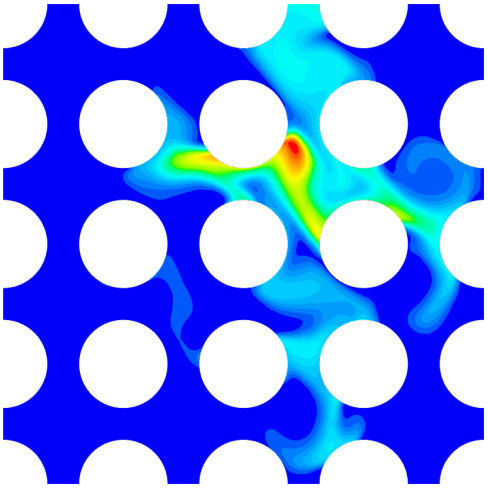

(b) Hexahedral-Trimmed V^2F k-ε

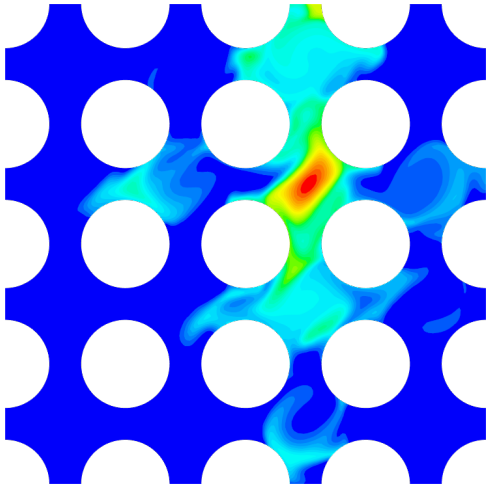

(c) Polyhedral k-ω

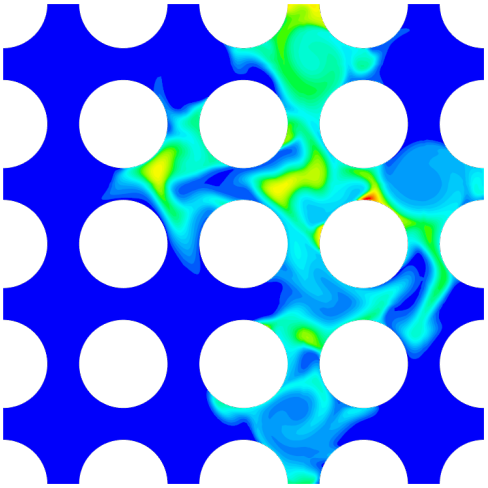

(d) Polyhedral V^2F k-ε

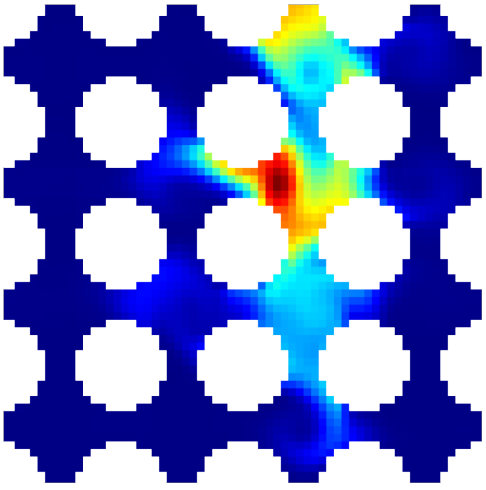

(e) Experimental data

450 mm measurements - Passive scalar contour

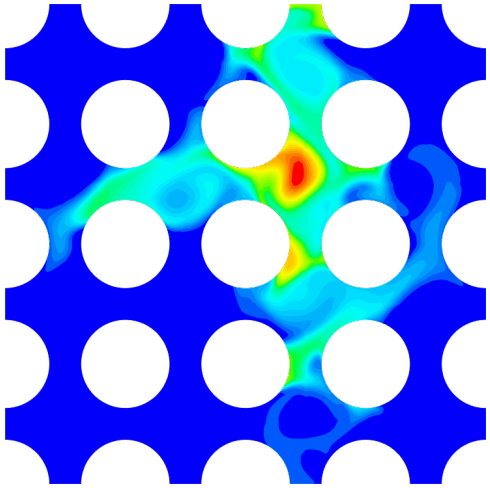

(a) Hexahedral-Trimmed k-ω

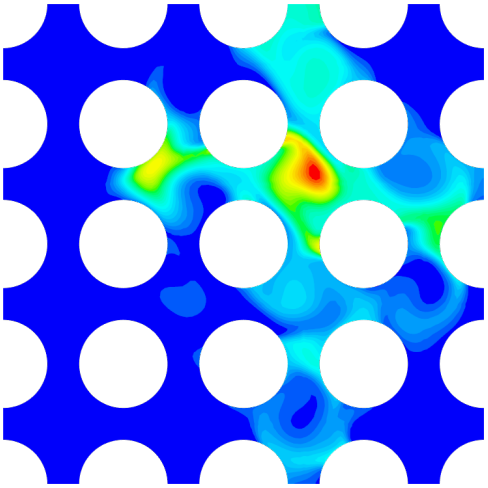

(b) Hexahedral-Trimmed V^2F k-ε

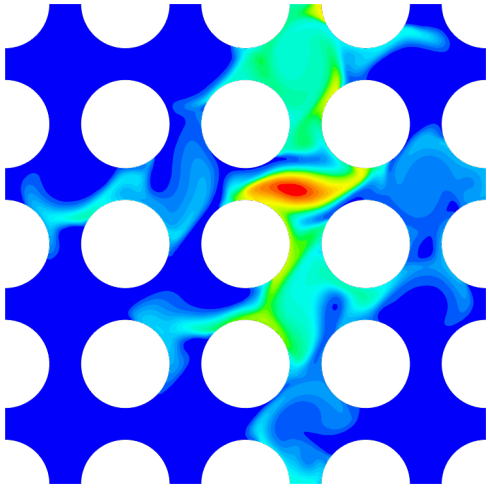

(c) Polyhedral k-ω

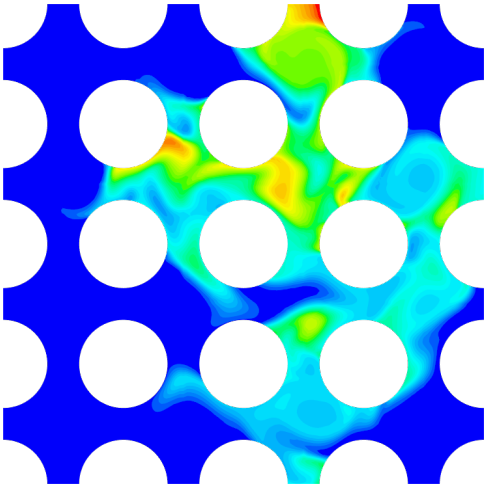

(d) Polyhedral V^2F k-ε

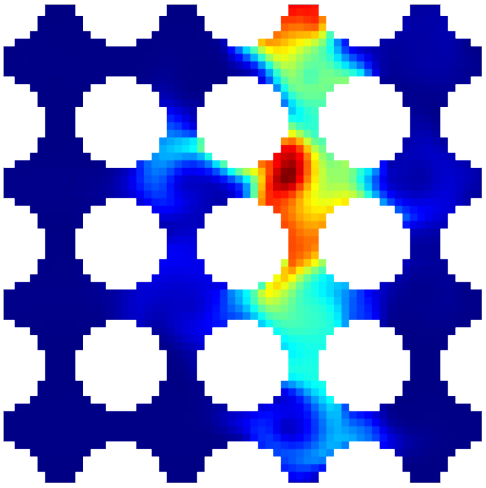

(e) Experimental data

550 mm measurements - Passive scalar contour

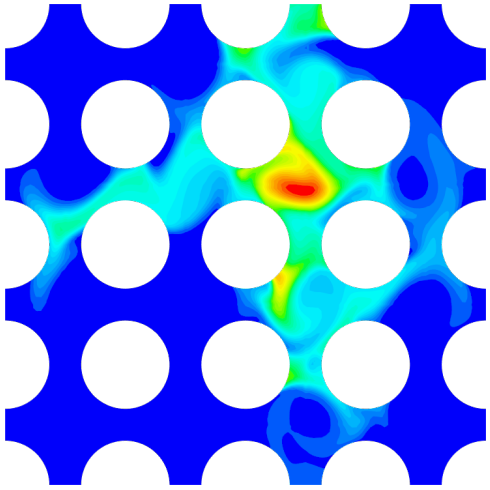

(a) Hexahedral-Trimmed k-ω

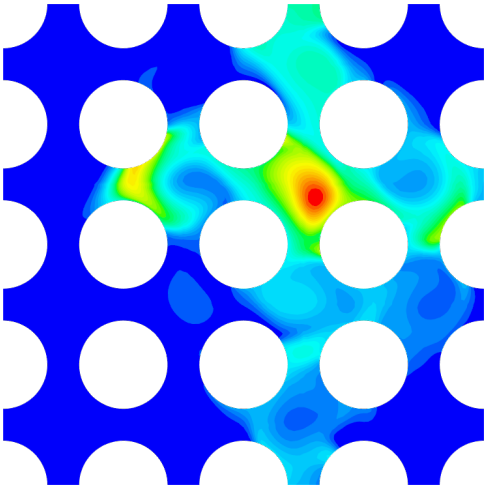

(b) Hexahedral-Trimmed V^2F k-ε

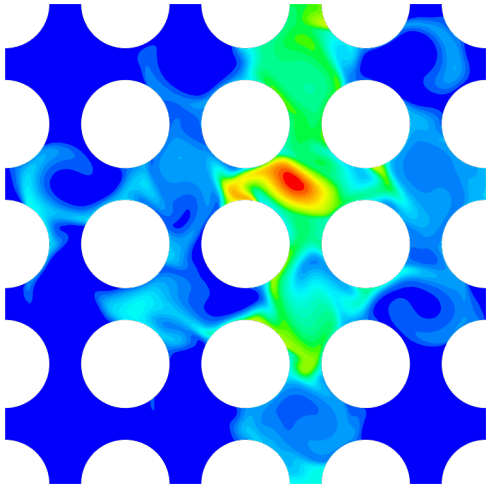

(c) Polyhedral k-ω

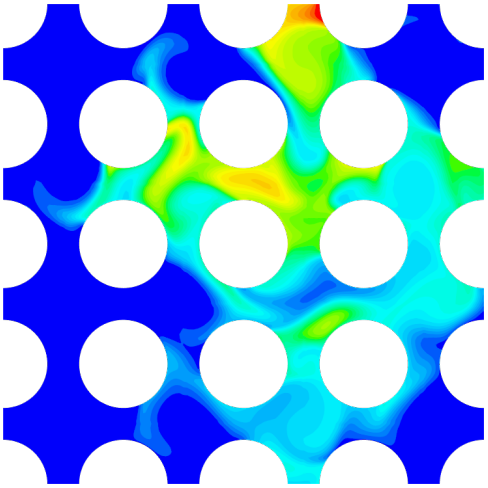

(d) Polyhedral V^2F k-ε

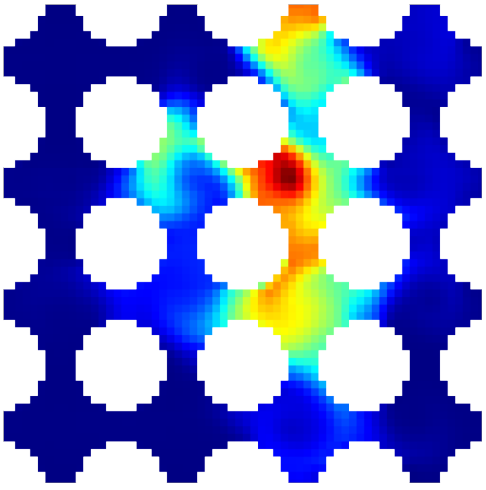

(e) Experimental data

In addition to the lateral velocity vectors, the passive scalar contours were also compared to the experimental data. This part of the study was also very important to check which model performed the best against the results of the experiment.

In the first monitoring plane, situated at 50 mm from the back edge of the spacer body, the four simulations got a good qualitative match with the experimental data, but the best shape was achieved by the hexahedral-trimmed V^2F k-ε model.

In the second monitoring plane, situated at 150 mm from the back edge of the spacer body, the situation is quite similar, and the hexahedral-trimmed V^2F k-ε is again the best match due to the similarities of the tracer present in the sub-channels adjacent to the injection.

In the third monitoring plane, situated at 250 mm from the back edge of the spacer body, the polyhedral k-ω and hexahedral-trimmed V^2F k-ε simulations achieve good matches compared to the experimental data. In the other two cases, there exist too much dispersion in the injection sub-channel.

The fourth monitoring plane, situated at 350 mm from the back edge of the spacer body, shows that the best match is again achieved by the hexahedral-trimmed V^2F k-ε case. After this case, the hexahedral-trimmed k-ω also performs well, but with some visible discrepancies.

There exists the same situation in the fifth monitoring plane, situated at 450 mm from the back edge of the spacer body. However, this time the general match is not as good as before, since the flow dynamics change between the simulations along the z axis. Nevertheless, both hexahedral-trimmed k-ω and V^2F k-ε do not perform badly.

Last but not least, in the sixth monitoring plane, placed at 550 mm from the back edge of the spacer body, hexahedral-trimmed V^2F k-ε and polyhedral k-ω to some extent show a matching trend, but general match is not good anymore.

4.3.4 Conclusions

After the mesh sensitivity study and the turbulence models analysis, there were two promising numerical models that showed good match on the lateral velocity vectors, passive scalar contours and tracer share: the hexahedral-trimmed V^2F k-ε and the polyhedral k-ω cases. As to the detailed velocity components extracted from different probe lines situated in the monitoring planes, generally no good match was obtained.

As mentioned in section 4.3.2, the hexahedral-trimmed model was very time consuming, since the simulations had to be run on transient solver and the results had to be averaged over time due to the fluctuating behaviour of instant variables. It was clear that further study on this topic was needed, possibly with a new refinement of the mesh and a time-step sensitivity analysis.

For these reasons, the model selected to perform the simulations on the rest of the spacers was the polyhedral k-ω, which showed relatively good results on different tests and was also not so demanding in terms of time and computational capability.

4.4 Different spacer grids

From chapter 4.3, a mesh configuration and turbulence model was chosen. This strategy was used to simulate the four types of spacers to check the similarities between the simulation results and the experimental data.

4.4.1 Spacer 1 - Standard 30°

The first type of spacer uses the standard vane configuration with an angle of 30° between the mixing vanes and the direction of the flow. This spacer was used for the turbulence analysis, and the results are presented below.

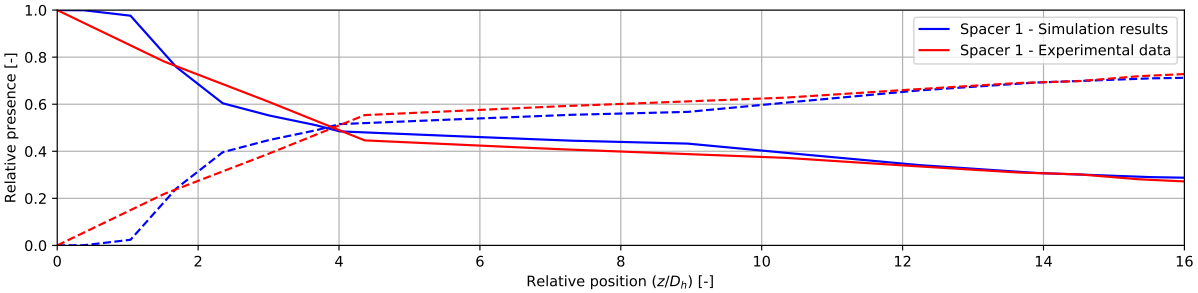

Figure 4.48: Tracer share comparison between experimental data and simulation results.

As mentioned in section 4.3.3, there is a good match between the simulated tracer share and the experimental data.

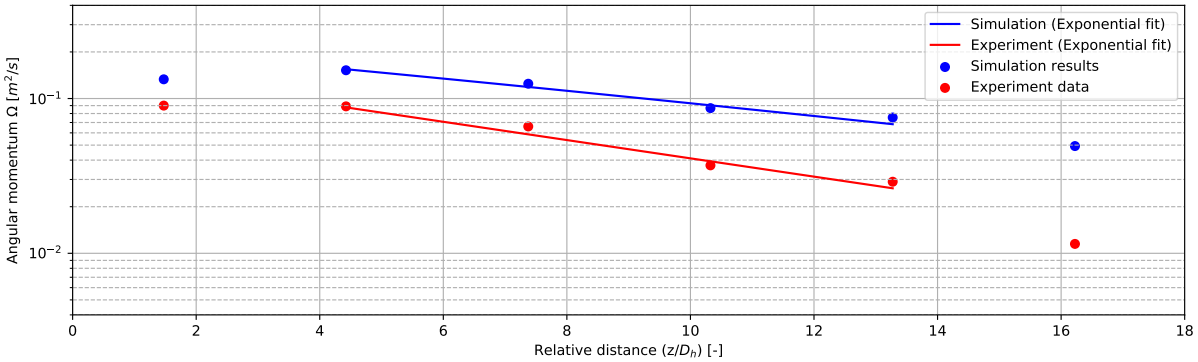

Figure 4.49: Swirl decay comparison between experimental data and simulation results.

The swirl decay from the simulation results presents some differences against the experimental one. The exponential fit was calculated using the second, third, fourth and fifth monitoring planes, following Dr. Ing. Arto's methodology.

	A	ϵA	ϵ_RA	B	ϵB	ϵ_RB
Simulation results	0.075	0.045	37.50%	0.222	0.058	35.47%
Experimental results	0.120	-	-	0.164	-	-

Table 4.5: Parameters of the exponential fit for spacer 1.

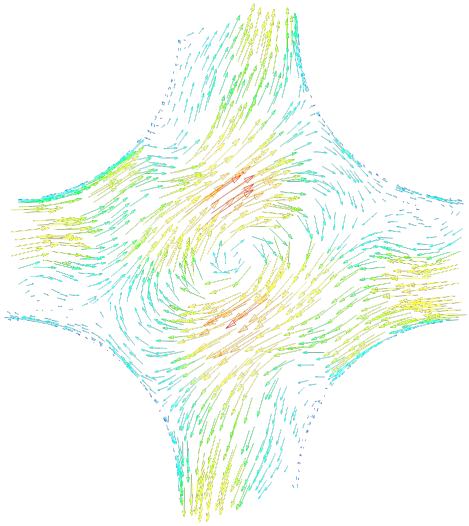

(a) Simulated lateral velocity vectors in the injection sub-channel at 50 mm from the back edge of the spacer body.

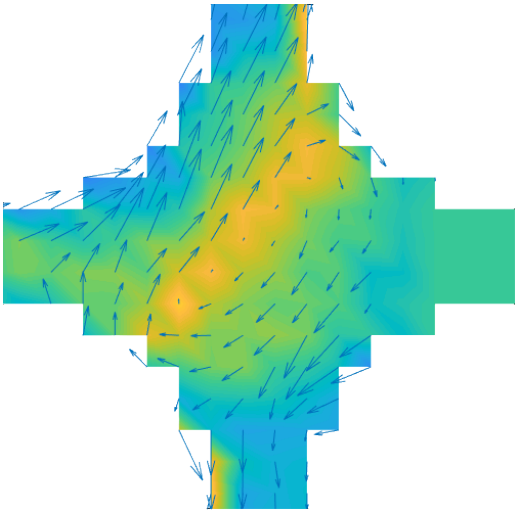

(b) Experimental lateral velocity vectors in the injection sub-channel at 50 mm from the back edge of the spacer body.

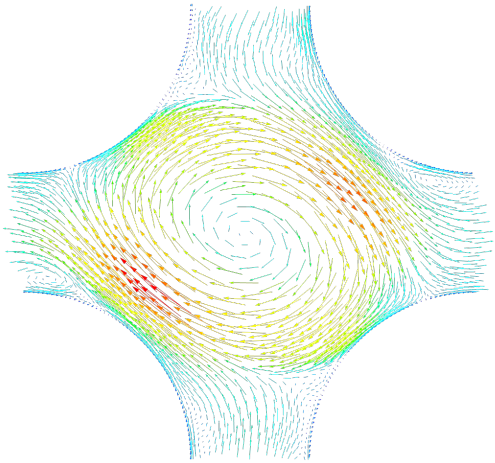

(c) Simulated lateral velocity vectors in the injection sub-channel at 150 mm from the back edge of the spacer body.

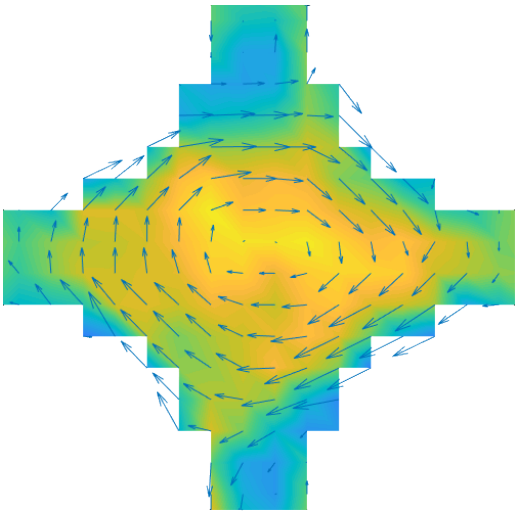

(d) Experimental lateral velocity vectors in the injection sub-channel at 150 mm from the back edge of the spacer body.

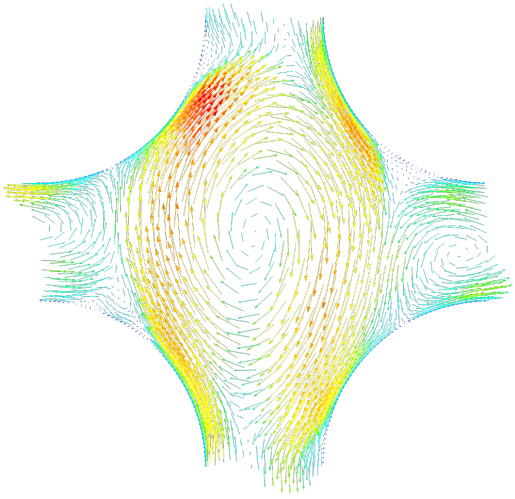

(e) Simulated lateral velocity vectors in the injection sub-channel at 250 mm from the back edge of the spacer body.

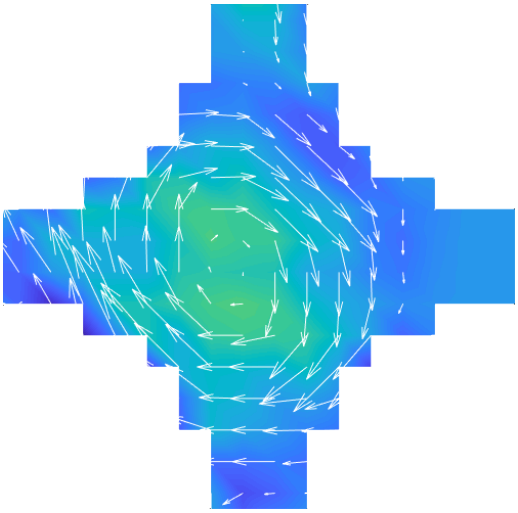

(f) Experimental lateral velocity vectors in the injection sub-channel at 250 mm from the back edge of the spacer body.

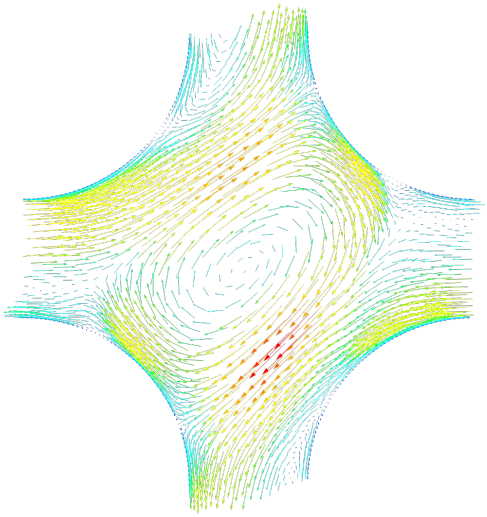

(a) Simulated lateral velocity vectors in the injection sub-channel at 350 mm from the back edge of the spacer body.

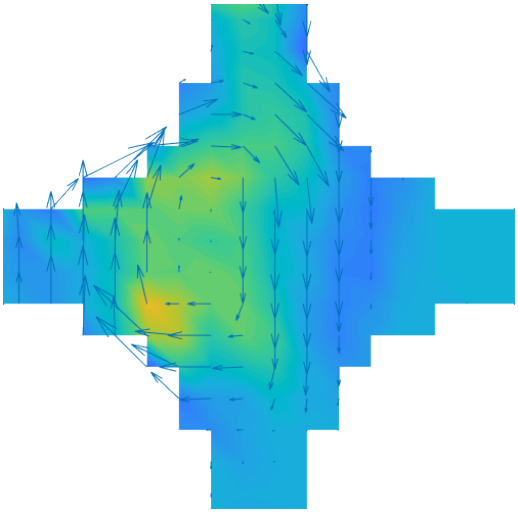

(b) Experimental lateral velocity vectors in the injection sub-channel at 350 mm from the back edge of the spacer body.

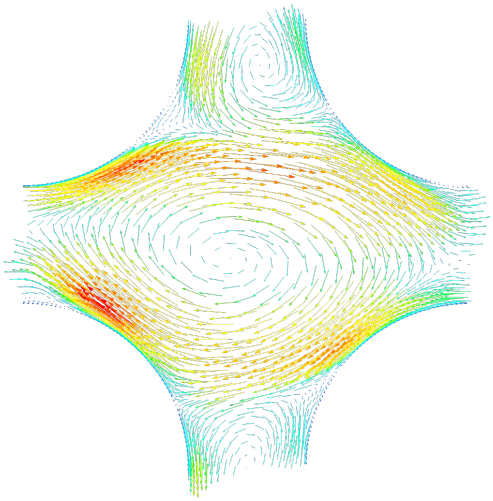

(c) Simulated lateral velocity vectors in the injection sub-channel at 450 mm from the back edge of the spacer body.

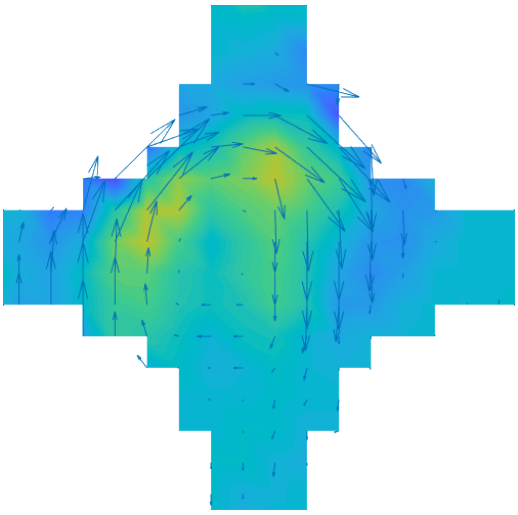

(d) Experimental lateral velocity vectors in the injection sub-channel at 450 mm from the back edge of the spacer body.

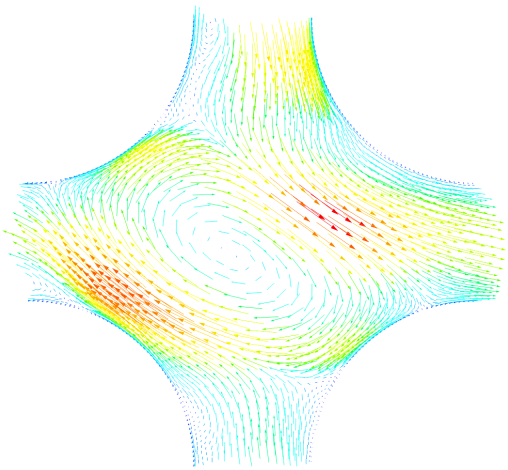

(e) Simulated lateral velocity vectors in the injection sub-channel at 550 mm from the back edge of the spacer body.

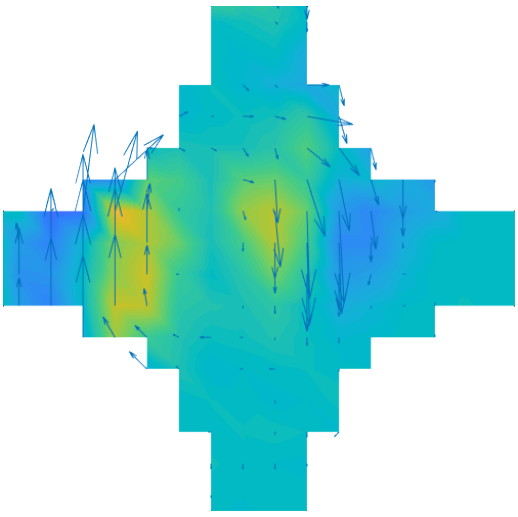

(f) Experimental lateral velocity vectors in the injection sub-channel at 550 mm from the back edge of the spacer body.

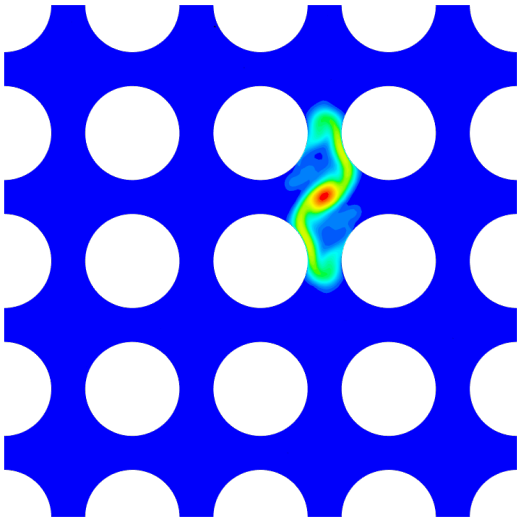

(a) Simulated tracer contour at 50 mm from the back edge of the spacer body.

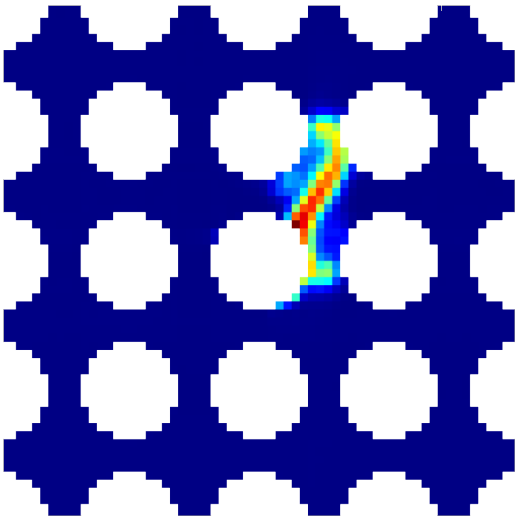

(b) Experimental tracer contour at 50 mm from the back edge of the spacer body.

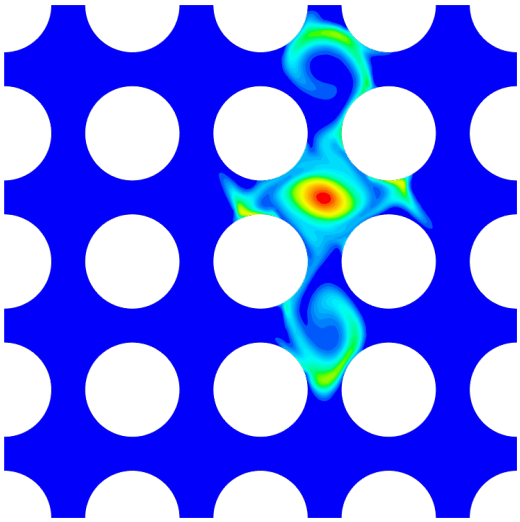

(c) Simulated tracer contour at 150 mm from the back edge of the spacer body.

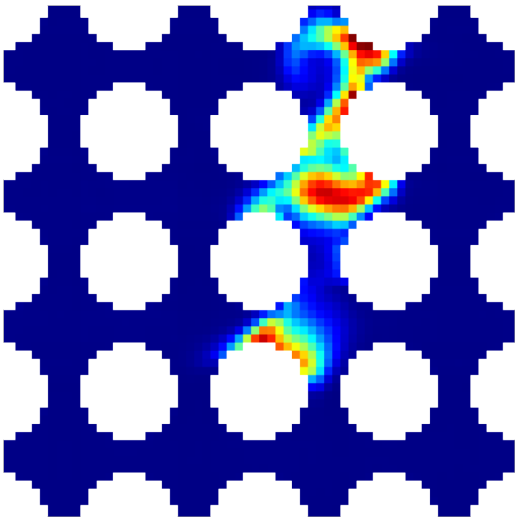

(d) Experimental tracer contour at 150 mm from the back edge of the spacer body.

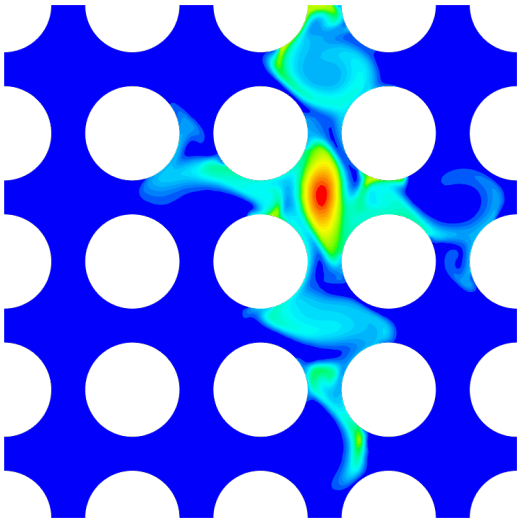

(e) Simulated tracer contour at 250 mm from the back edge of the spacer body.

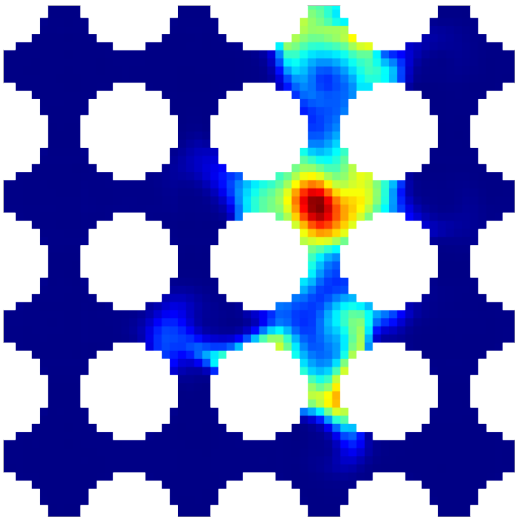

(f) Experimental tracer contour at 250 mm from the back edge of the spacer body.

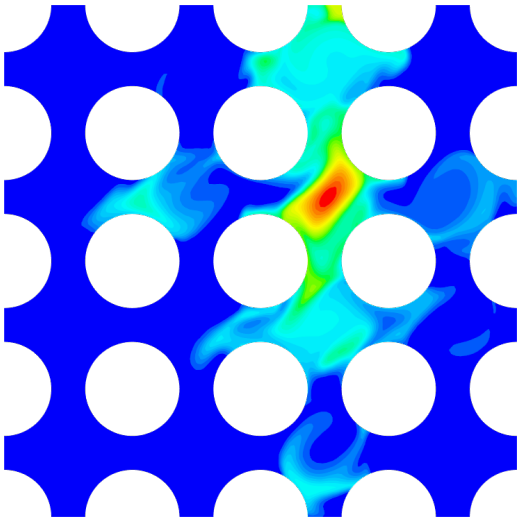

(a) Simulated tracer contour at 350 mm from the back edge of the spacer body.

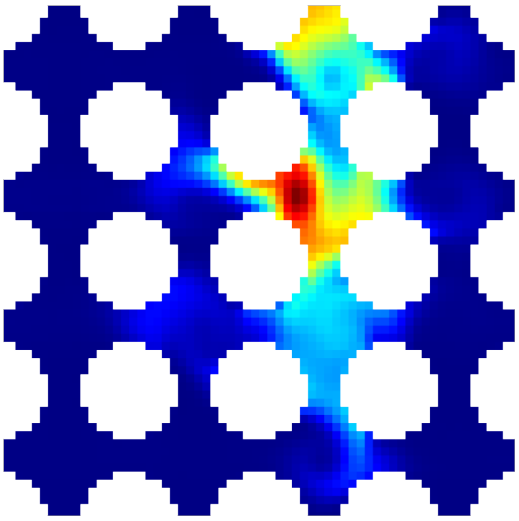

(b) Experimental tracer contour at 350 mm from the back edge of the spacer body.

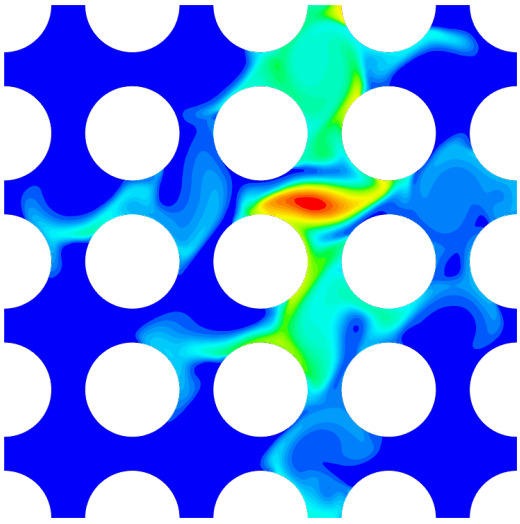

(c) Simulated tracer contour at 450 mm from the back edge of the spacer body.

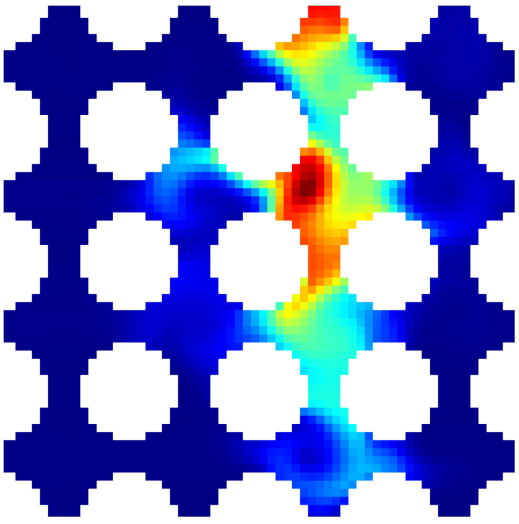

(d) Experimental tracer contour at 450 mm from the back edge of the spacer body.

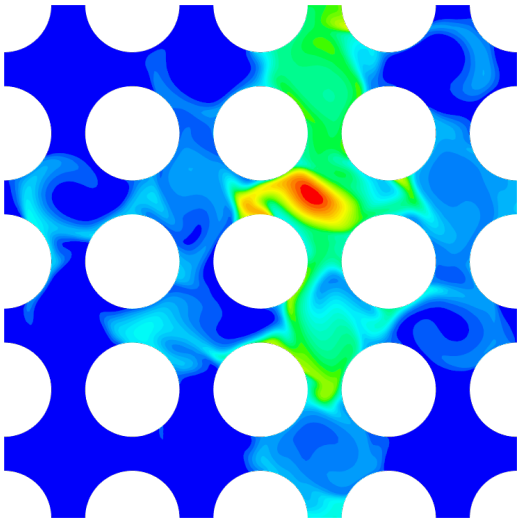

(e) Simulated tracer contour at 550 mm from the back edge of the spacer body.

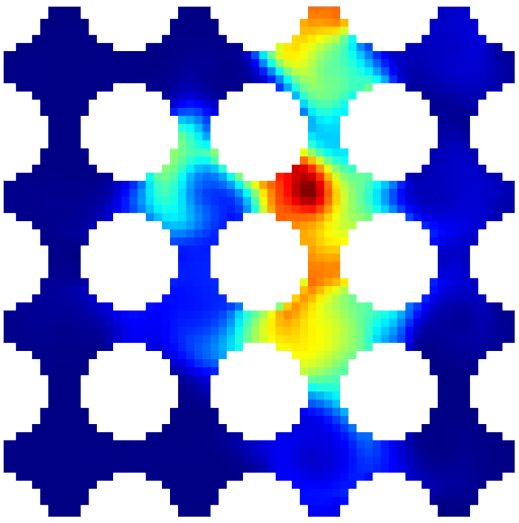

(f) Experimental tracer contour at 550 mm from the back edge of the spacer body.

4.4.2 Spacer 2 - Alternate 30°

The second type of spacer uses the alternate vane configuration with an angle of 30° between the mixing vanes and the direction of the flow. The results are presented below.

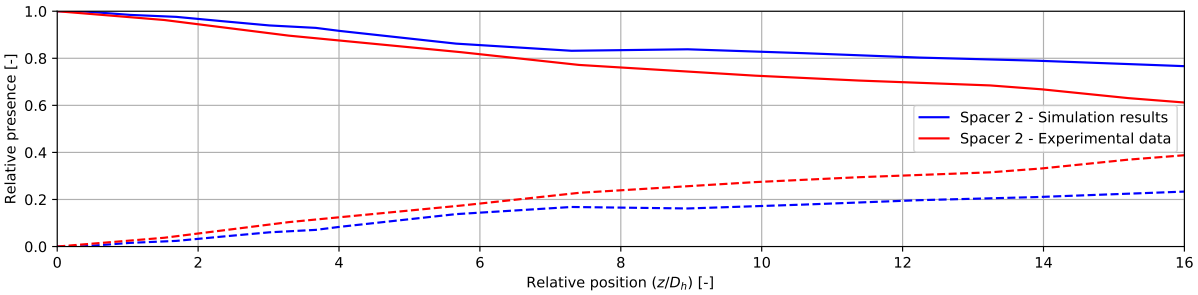

Figure 4.54: Tracer share comparison between experimental data and simulation results.

The results from the simulation show that there is less mixing between adjacent sub-channels compared to the experimental data. The relative difference between the two values increases along the z axis.

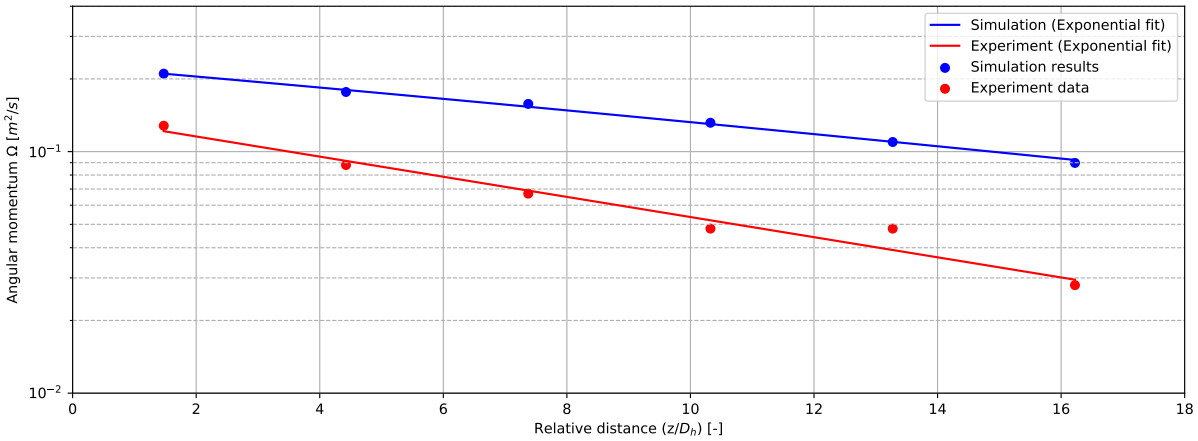

Figure 4.55: Swirl decay comparison between experimental data and simulation results.

The swirl decay from the simulation results presents some differences against the experimental one in both the initial angular momentum and the decay rate. The exponential fit was calculated using the data from the six monitoring planes, following Dr. Ing. Arto's methodology.

	A	ϵA	ϵ_RA	B	ϵB	ϵ_RB
Simulation results	0.051	0.034	40.00%	0.232	0.092	66.21%
Experimental results	0.085	-	-	0.139	-	-

Table 4.6: Parameters of the exponential fit for spacer 2.

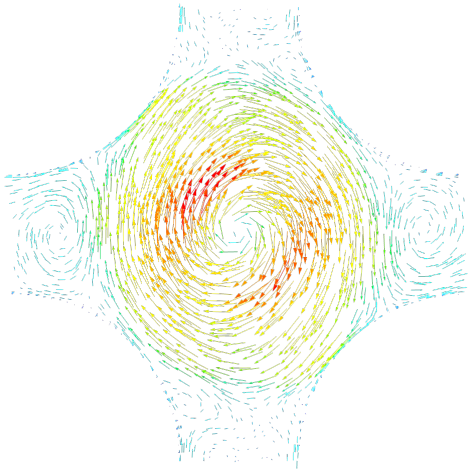

(a) Simulated lateral velocity vectors in the injection sub-channel at 50 mm from the back edge of the spacer body.

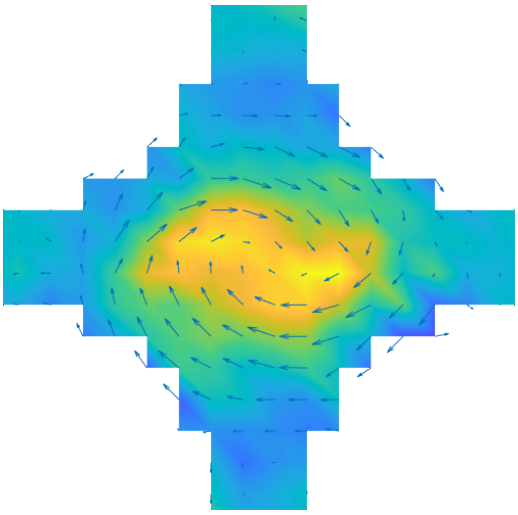

(b) Experimental lateral velocity vectors in the injection sub-channel at 50 mm from the back edge of the spacer body.

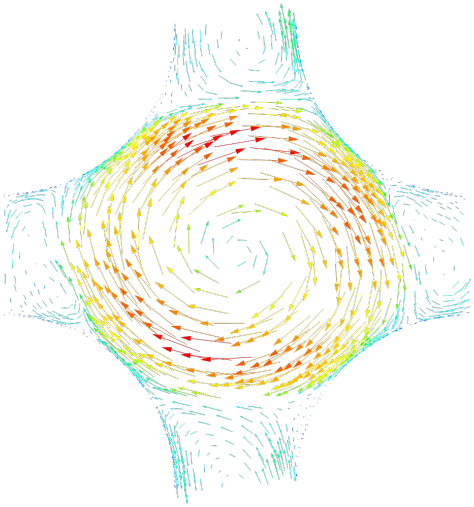

(c) Simulated lateral velocity vectors in the injection sub-channel at 150 mm from the back edge of the spacer body.

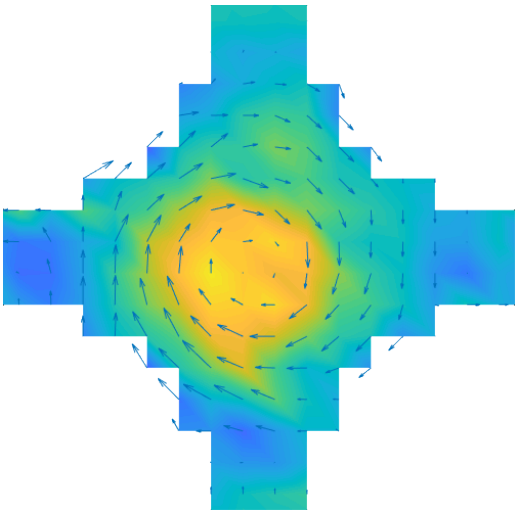

(d) Experimental lateral velocity vectors in the injection sub-channel at 150 mm from the back edge of the spacer body.

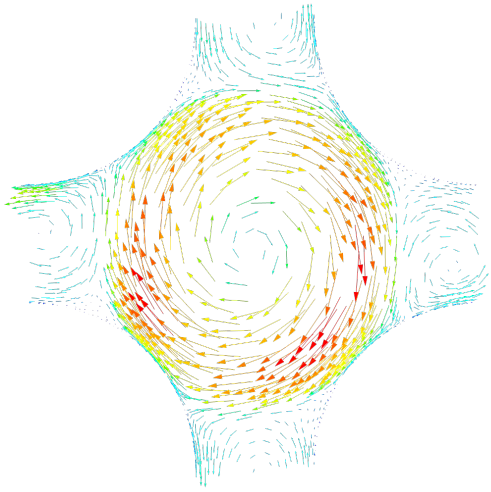

(e) Simulated lateral velocity vectors in the injection sub-channel at 250 mm from the back edge of the spacer body.

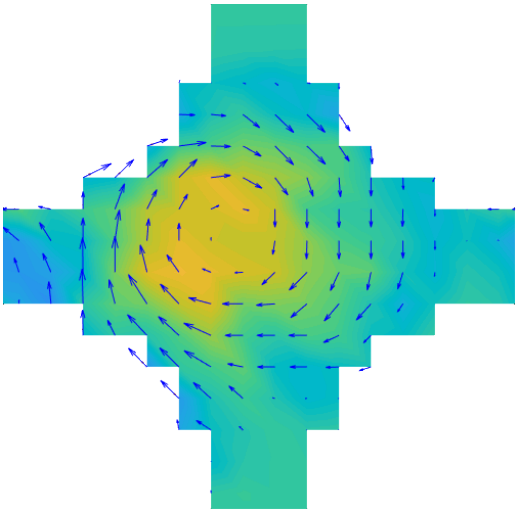

(f) Experimental lateral velocity vectors in the injection sub-channel at 250 mm from the back edge of the spacer body.

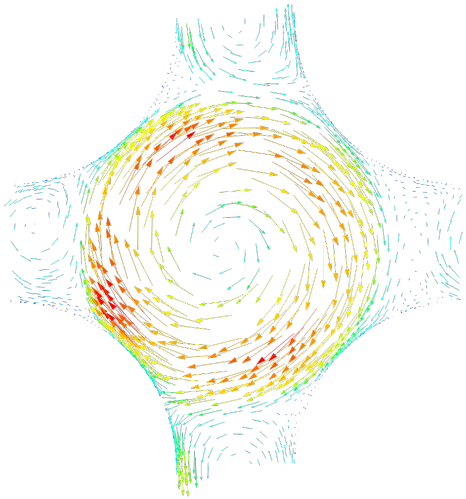

(a) Simulated lateral velocity vectors in the injection sub-channel at 350 mm from the back edge of the spacer body.

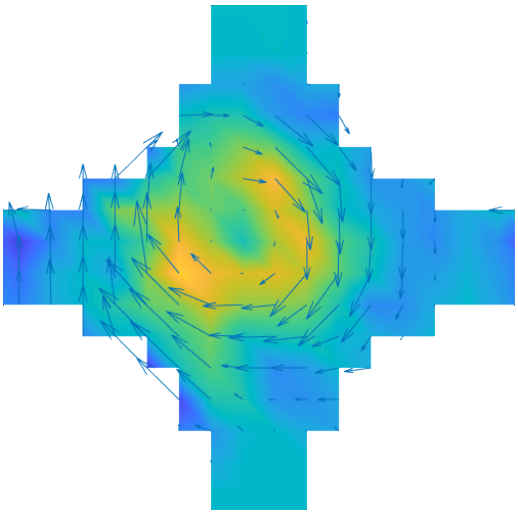

(b) Experimental lateral velocity vectors in the injection sub-channel at 350 mm from the back edge of the spacer body.

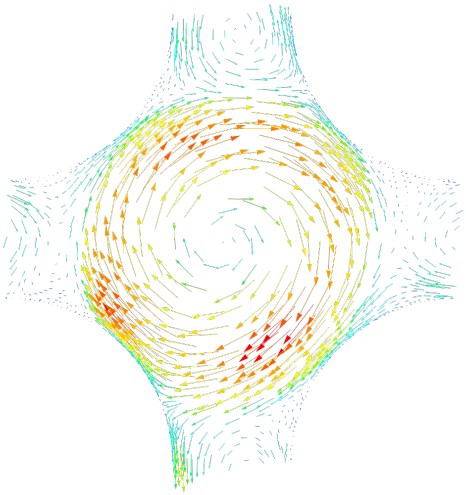

(c) Simulated lateral velocity vectors in the injection sub-channel at 450 mm from the back edge of the spacer body.

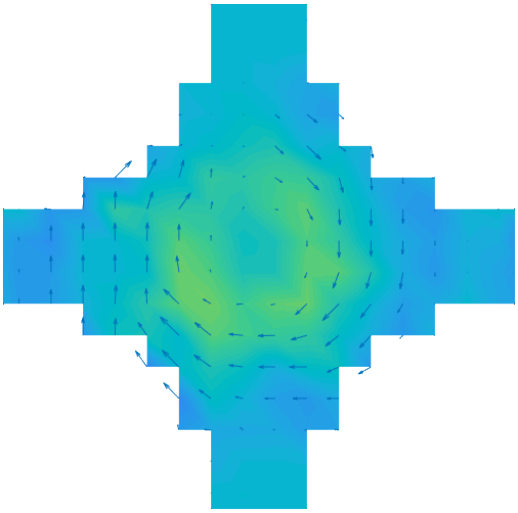

(d) Experimental lateral velocity vectors in the injection sub-channel at 450 mm from the back edge of the spacer body.

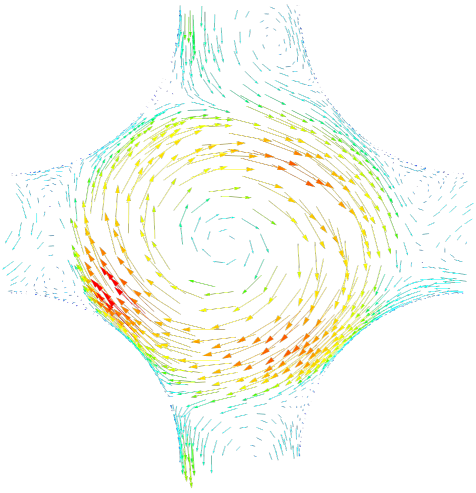

(e) Simulated lateral velocity vectors in the injection sub-channel at 550 mm from the back edge of the spacer body.

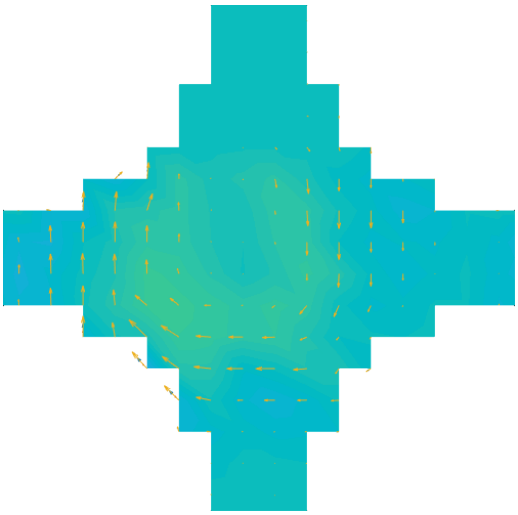

(f) Experimental lateral velocity vectors in the injection sub-channel at 550 mm from the back edge of the spacer body.

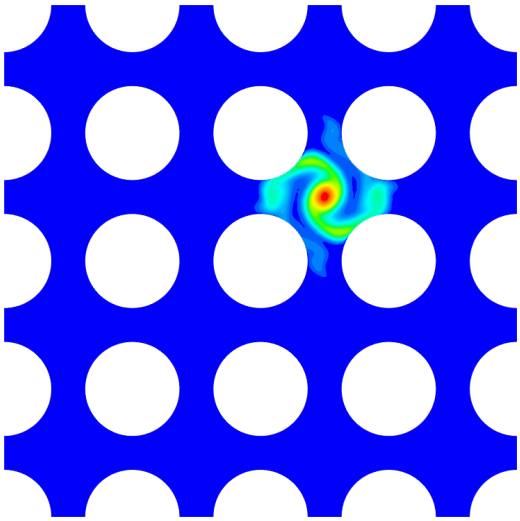

(a) Simulated tracer contour at 50 mm from the back edge of the spacer body.

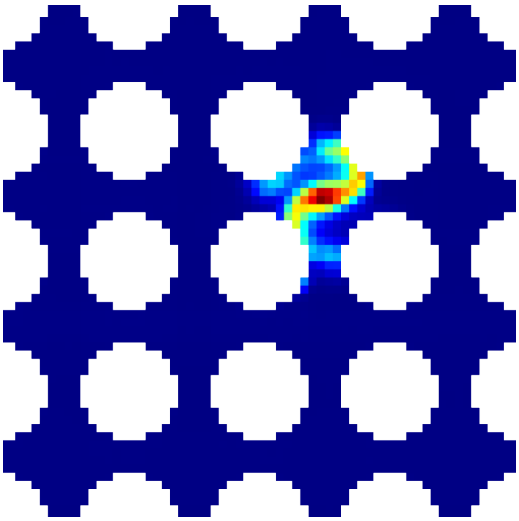

(b) Experimental tracer contour at 50 mm from the back edge of the spacer body.

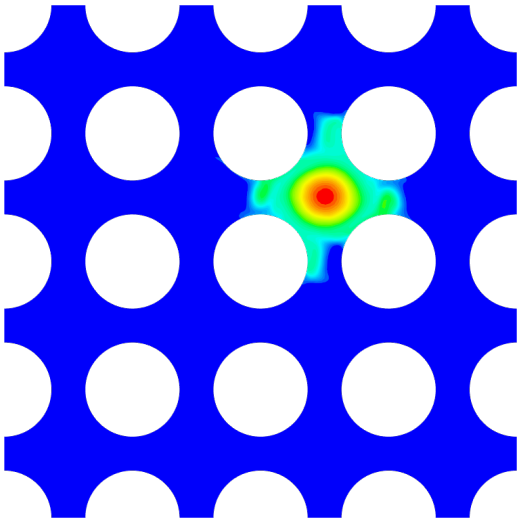

(c) Simulated tracer contour at 150 mm from the back edge of the spacer body.

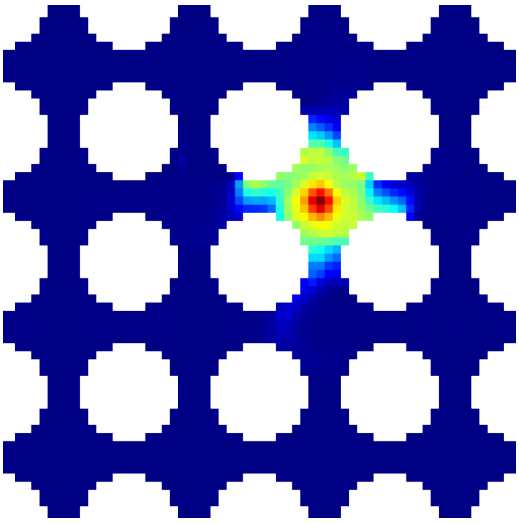

(d) Experimental tracer contour at 150 mm from the back edge of the spacer body.

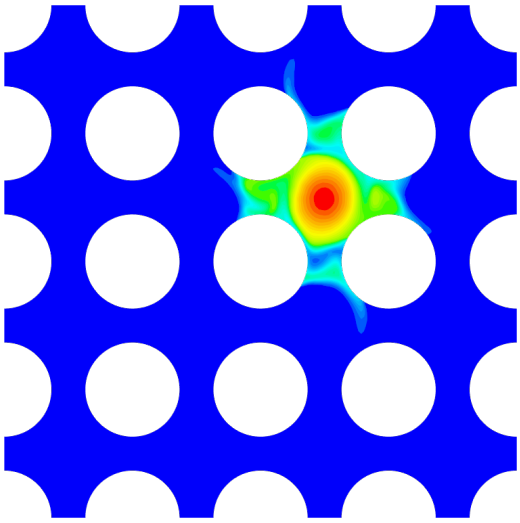

(e) Simulated tracer contour at 250 mm from the back edge of the spacer body.

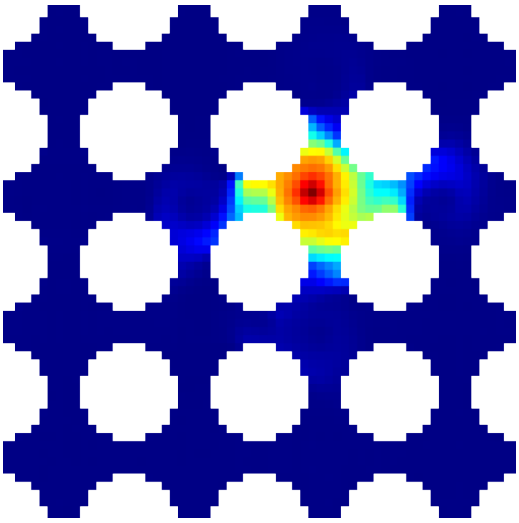

(f) Experimental tracer contour at 250 mm from the back edge of the spacer body.

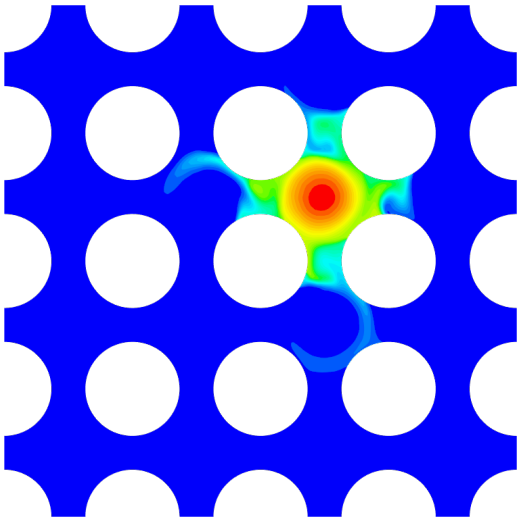

(a) Simulated tracer contour at 350 mm from the back edge of the spacer body.

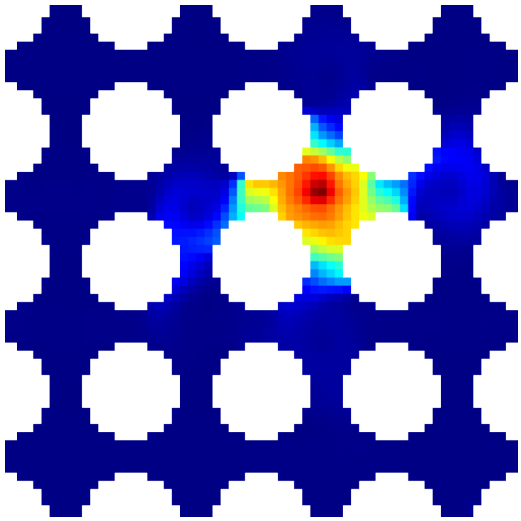

(b) Experimental tracer contour at 350 mm from the back edge of the spacer body.

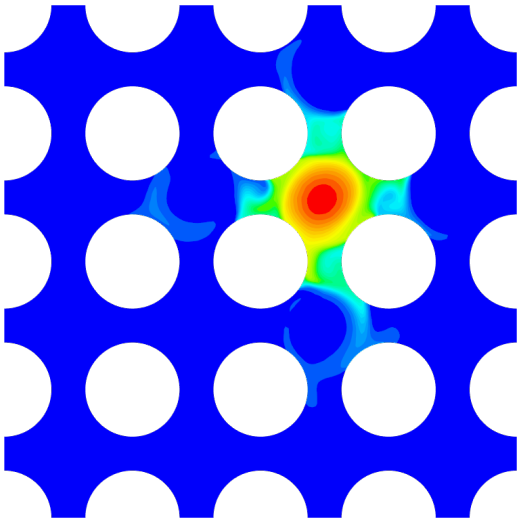

(c) Simulated tracer contour at 450 mm from the back edge of the spacer body.

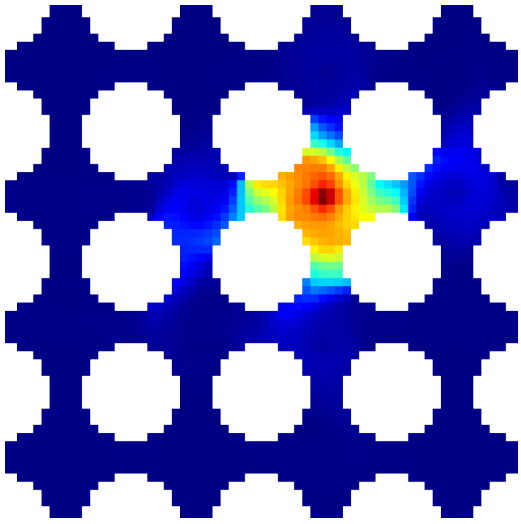

(d) Experimental tracer contour at 450 mm from the back edge of the spacer body.

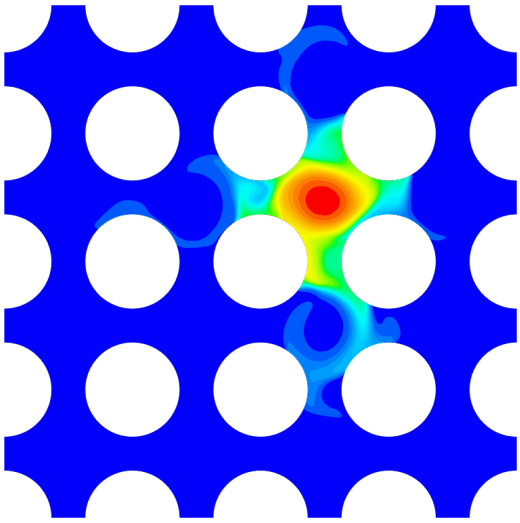

(e) Simulated tracer contour at 550 mm from the back edge of the spacer body.

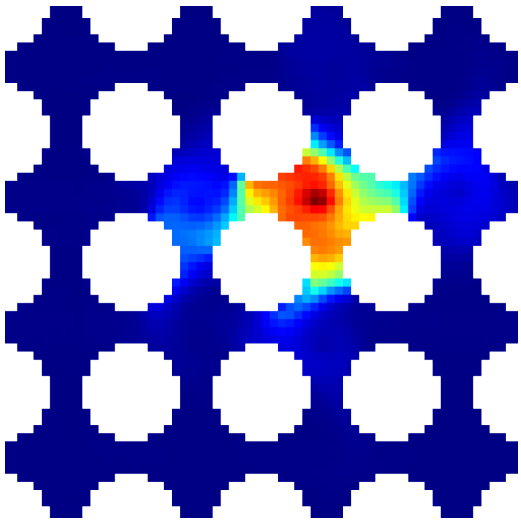

(f) Experimental tracer contour at 550 mm from the back edge of the spacer body.

4.4.3 Spacer 3 - Standard 15°

The second type of spacer uses the standard vane configuration with an angle of 15° between the mixing vanes and the direction of the flow. This type of spacer was used for the polyhedral mesh sensitivity analysis. The results are presented below.

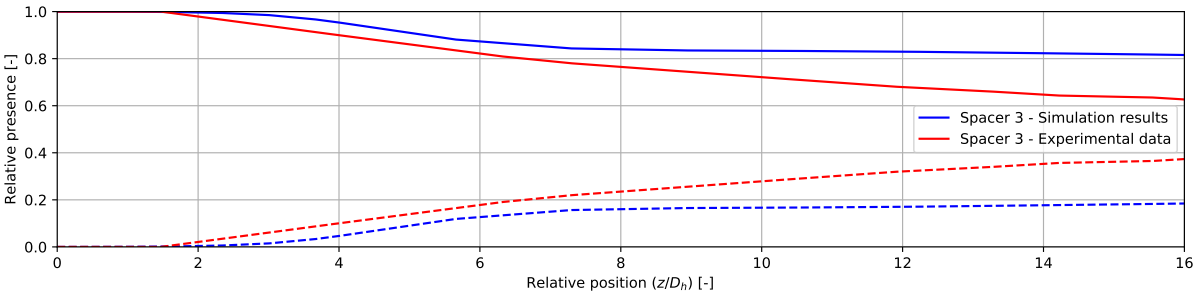

Figure 4.60: Tracer share comparison between experimental data and simulation results.

The results from the simulation show that there is less mixing between adjacent sub-channels compared to the experimental data. The relative difference between the two values increases along the z axis.

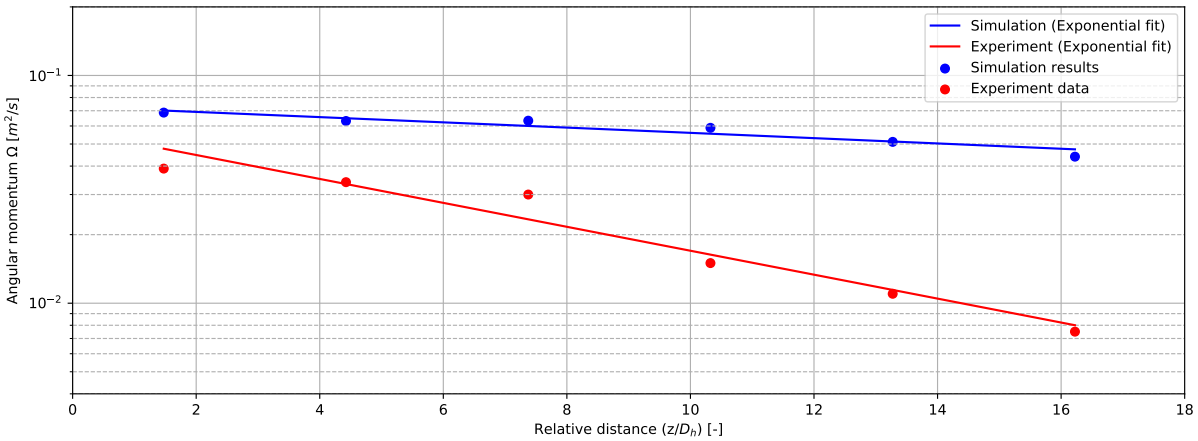

Figure 4.61: Swirl decay comparison between experimental data and simulation results.

The swirl decay from the simulation results presents some differences against the experimental one especially in terms of decay rate. The exponential fit was calculated using the data from the six monitoring planes, following Dr. Ing. Arto's methodology.

	A	ϵA	ϵ_RA	B	ϵB	ϵ_RB
Simulation results	0.025	0.082	76.64%	0.044	0.036	450.00%
Experimental results	0.107	-	-	0.008	-	-

Table 4.7: Parameters of the exponential fit for spacer 3.

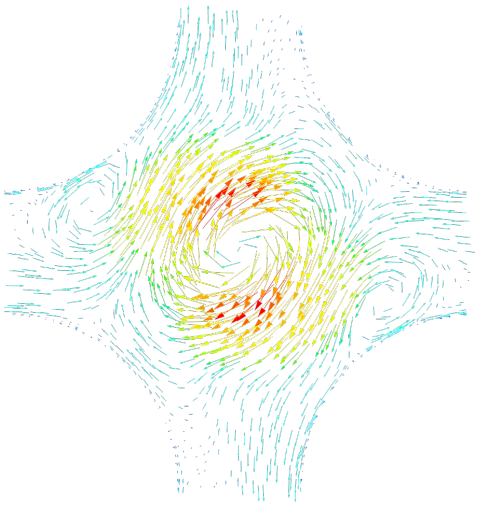

(a) Simulated lateral velocity vectors in the injection sub-channel at 50 mm from the back edge of the spacer body.

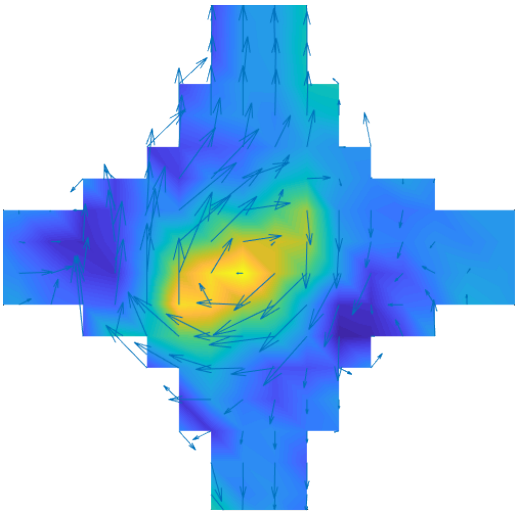

(b) Experimental lateral velocity vectors in the injection sub-channel at 50 mm from the back edge of the spacer body.

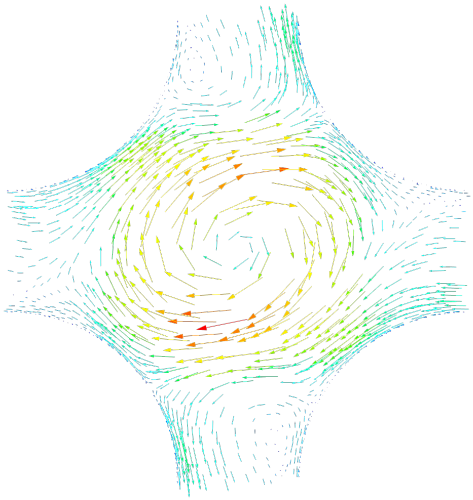

(c) Simulated lateral velocity vectors in the injection sub-channel at 150 mm from the back edge of the spacer body.

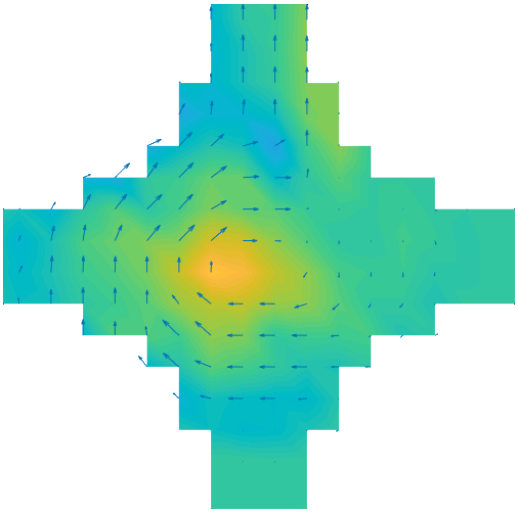

(d) Experimental lateral velocity vectors in the injection sub-channel at 150 mm from the back edge of the spacer body.

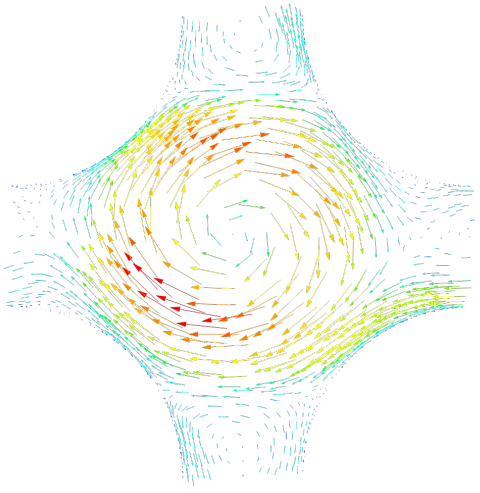

(e) Simulated lateral velocity vectors in the injection sub-channel at 250 mm from the back edge of the spacer body.

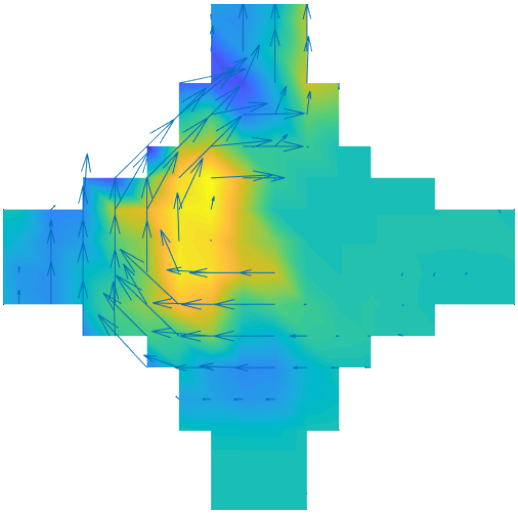

(f) Experimental lateral velocity vectors in the injection sub-channel at 250 mm from the back edge of the spacer body.

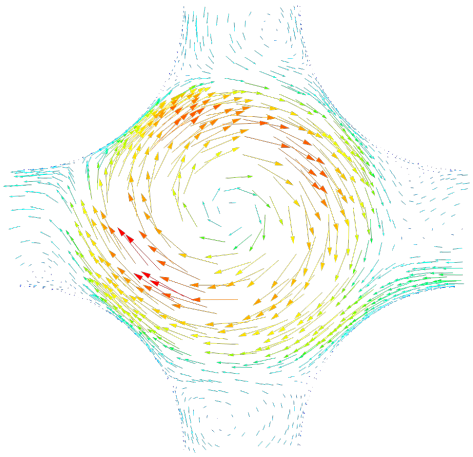

(a) Simulated lateral velocity vectors in the injection sub-channel at 350 mm from the back edge of the spacer body.

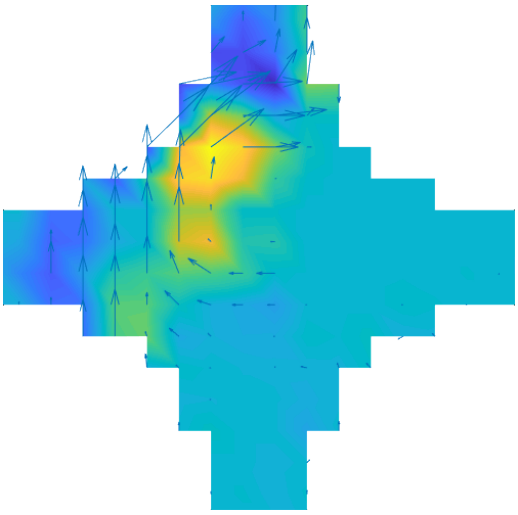

(b) Experimental lateral velocity vectors in the injection sub-channel at 350 mm from the back edge of the spacer body.

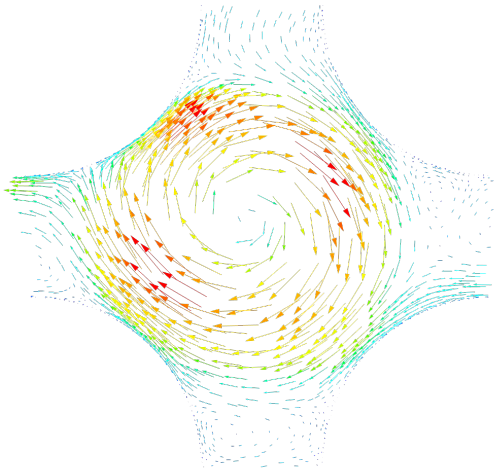

(c) Simulated lateral velocity vectors in the injection sub-channel at 450 mm from the back edge of the spacer body.

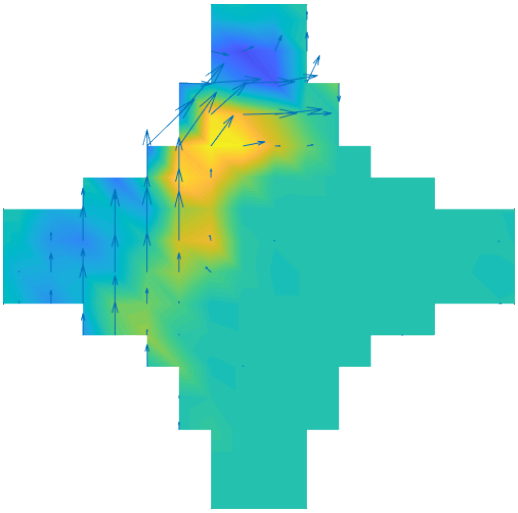

(d) Experimental lateral velocity vectors in the injection sub-channel at 450 mm from the back edge of the spacer body.

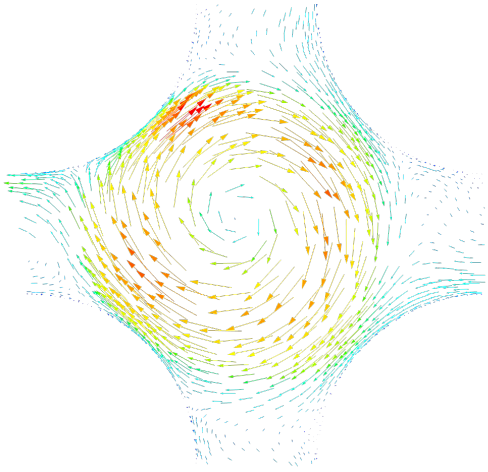

(e) Simulated lateral velocity vectors in the injection sub-channel at 550 mm from the back edge of the spacer body.

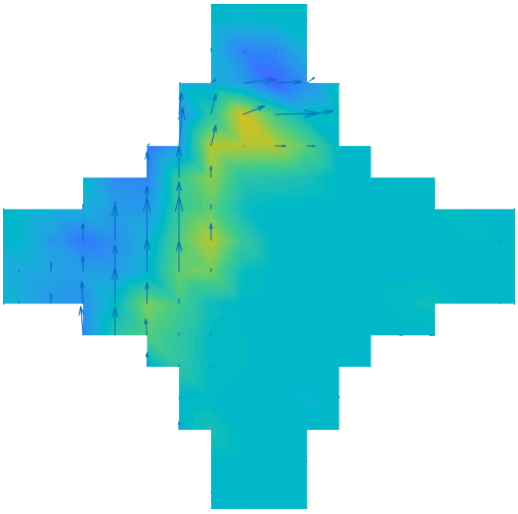

(f) Experimental lateral velocity vectors in the injection sub-channel at 550 mm from the back edge of the spacer body.

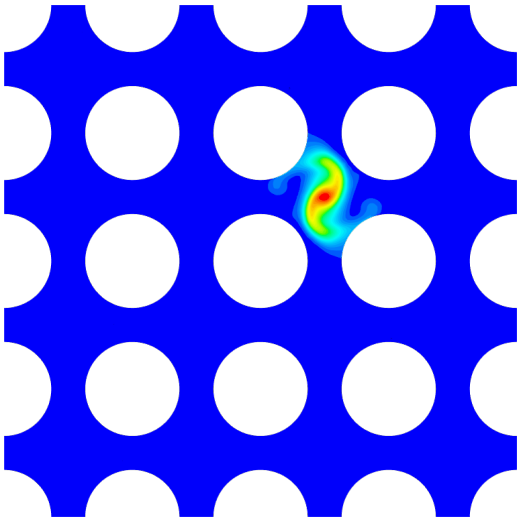

(a) Simulated tracer contour at 50 mm from the back edge of the spacer body.

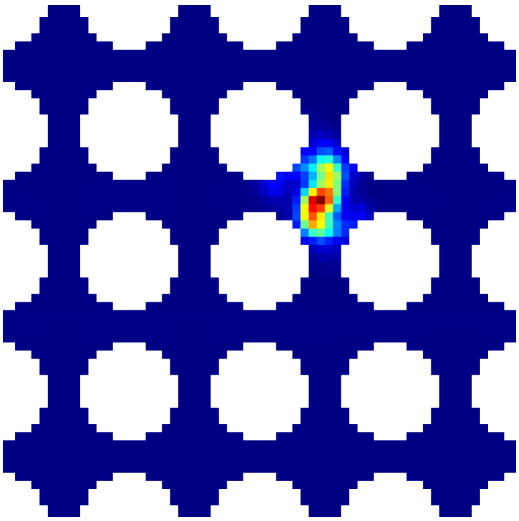

(b) Experimental tracer contour at 50 mm from the back edge of the spacer body.

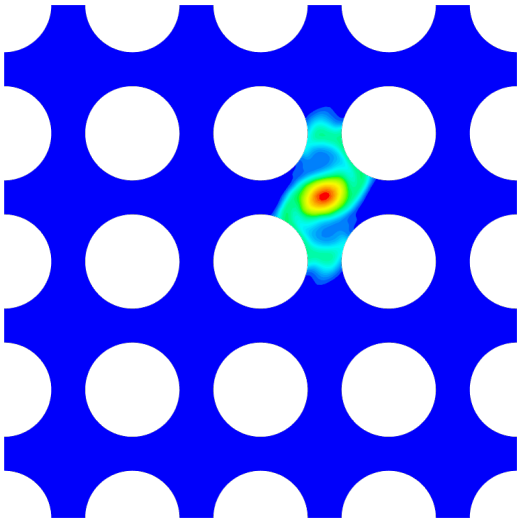

(c) Simulated tracer contour at 150 mm from the back edge of the spacer body.

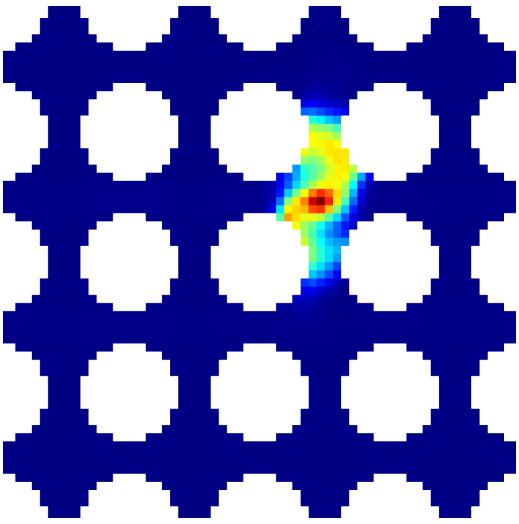

(d) Experimental tracer contour at 150 mm from the back edge of the spacer body.

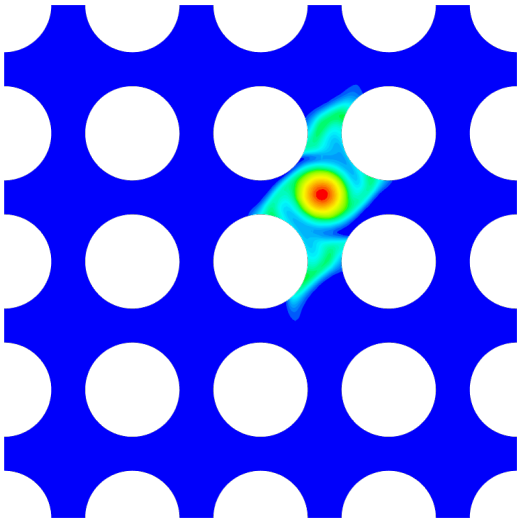

(e) Simulated tracer contour at 250 mm from the back edge of the spacer body.

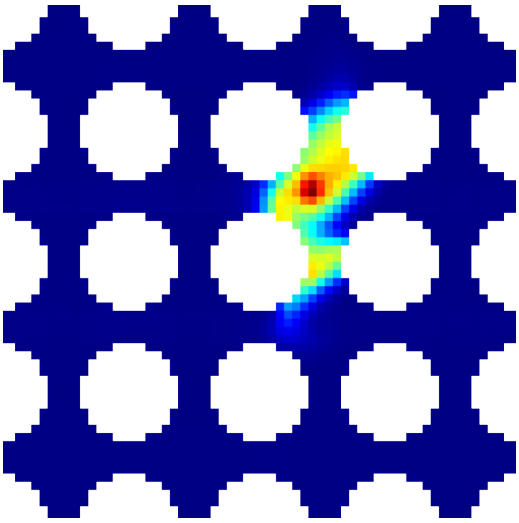

(f) Experimental tracer contour at 250 mm from the back edge of the spacer body.

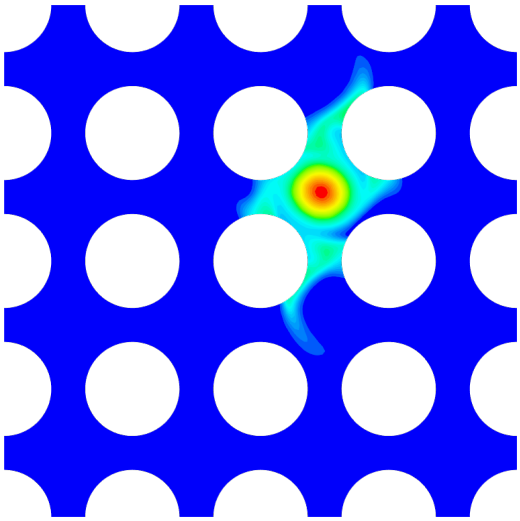

(a) Simulated tracer contour at 350 mm from the back edge of the spacer body.

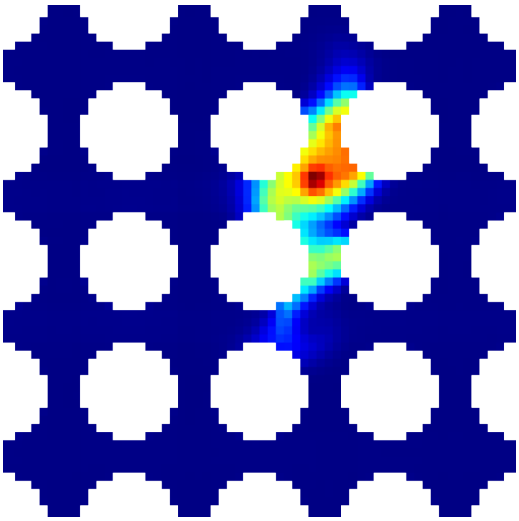

(b) Experimental tracer contour at 350 mm from the back edge of the spacer body.

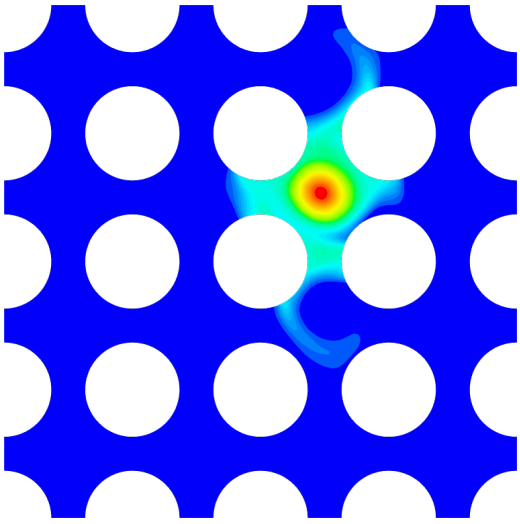

(c) Simulated tracer contour at 450 mm from the back edge of the spacer body.

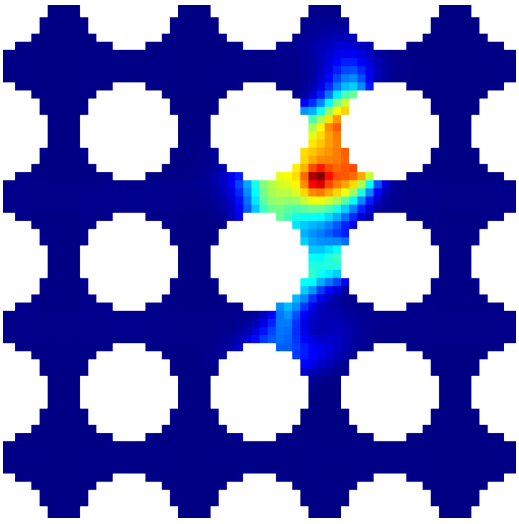

(d) Experimental tracer contour at 450 mm from the back edge of the spacer body.

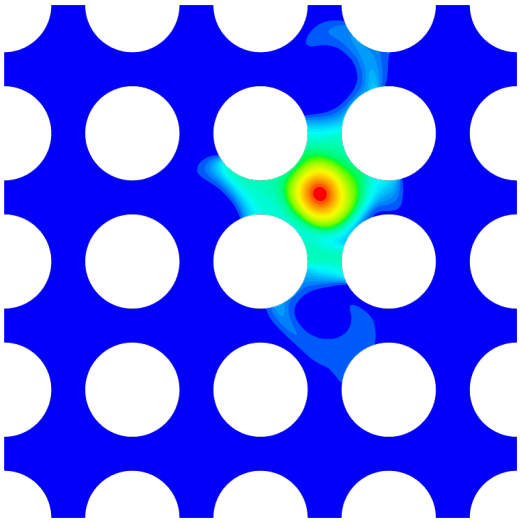

(e) Simulated tracer contour at 550 mm from the back edge of the spacer body.

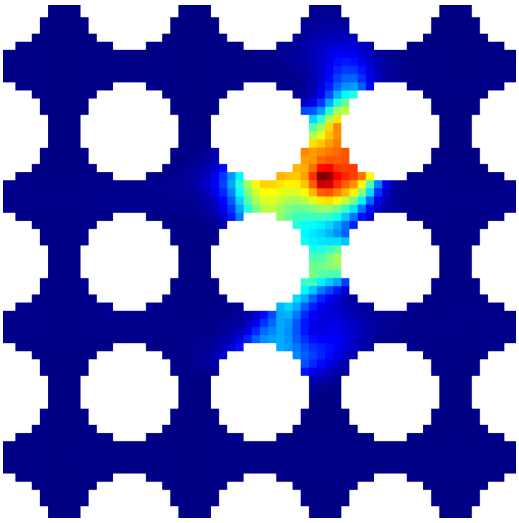

(f) Experimental tracer contour at 550 mm from the back edge of the spacer body.

4.4.4 Spacer 4 - Alternate 15°

The second type of spacer uses the alternate vane configuration with an angle of 15° between the mixing vanes and the direction of the flow. The results are presented below.

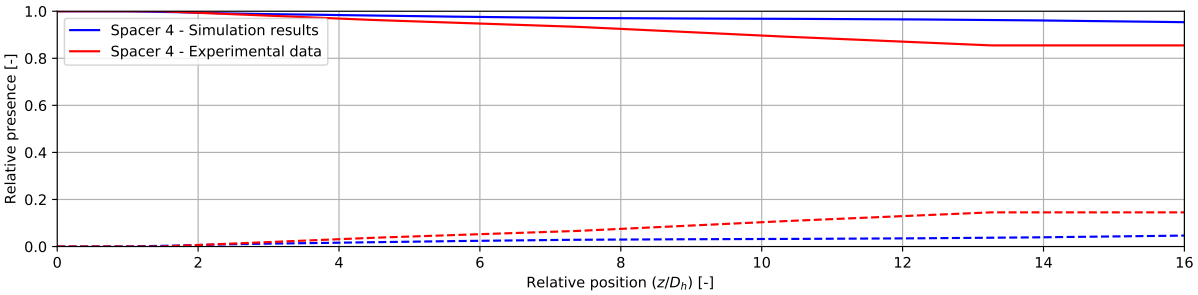

Figure 4.66: Tracer share comparison between experimental data and simulation results.

The results from the simulation show that there is less mixing between adjacent sub-channels compared to the experimental data. The simulation is not able to capture the mixing and it remains quite constant along the z axis, with minor improvements. The experimental data, however, shows an increasing tracer share along the former axis.

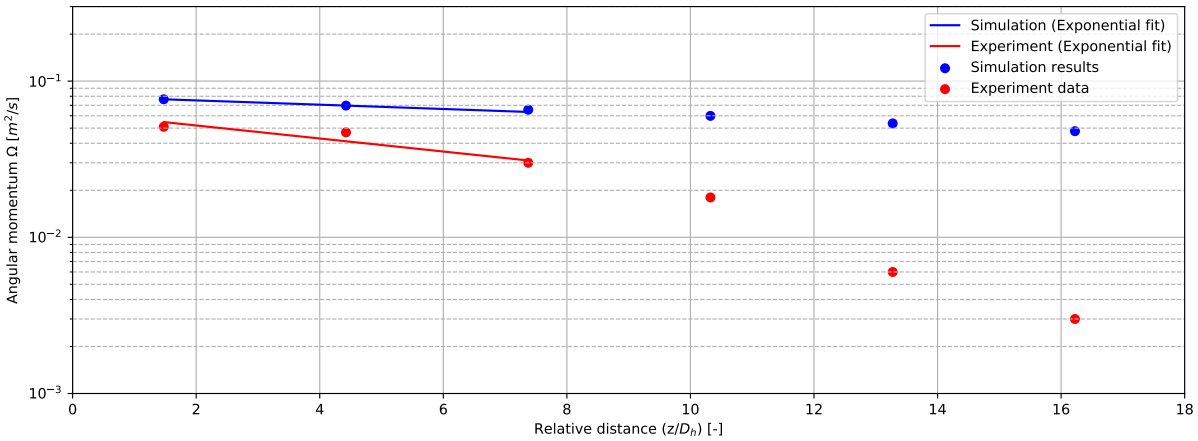

Figure 4.67: Swirl decay comparison between experimental data and simulation results.

The swirl decay from the simulation results presents some differences against the experimental one especially in terms of decay rate. The exponential fit was calculated using the data from the first, second and third monitoring planes, following Dr. Ing. Arto's methodology.

	A	ϵA	ϵ_RA	B	ϵB	ϵ_RB
Simulation results	0.023	0.058	71.60%	0.079	0.017	27.79%
Experimental results	0.081	-	-	0.062	-	-

Table 4.8: Parameters of the exponential fit for spacer 4.

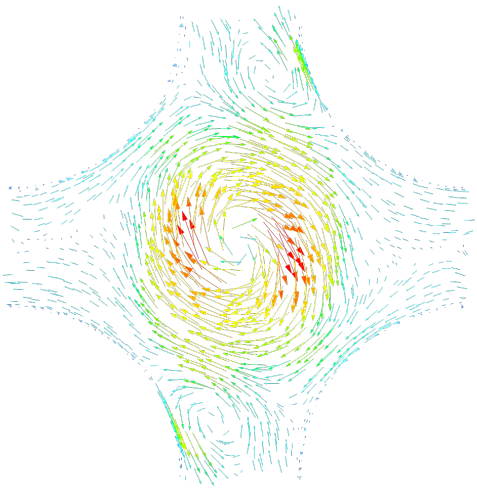

(a) Simulated lateral velocity vectors in the injection sub-channel at 50 mm from the back edge of the spacer body.

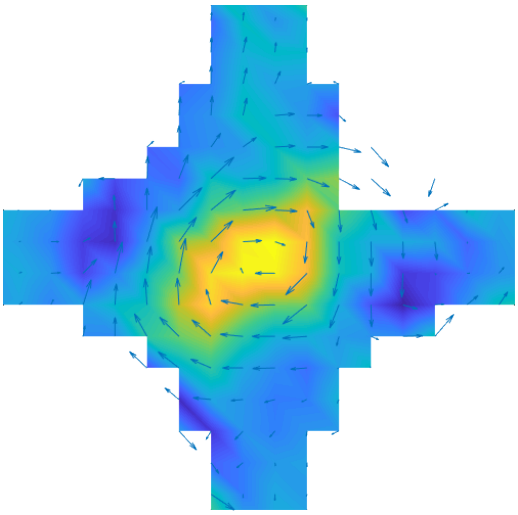

(b) Experimental lateral velocity vectors in the injection sub-channel at 50 mm from the back edge of the spacer body.

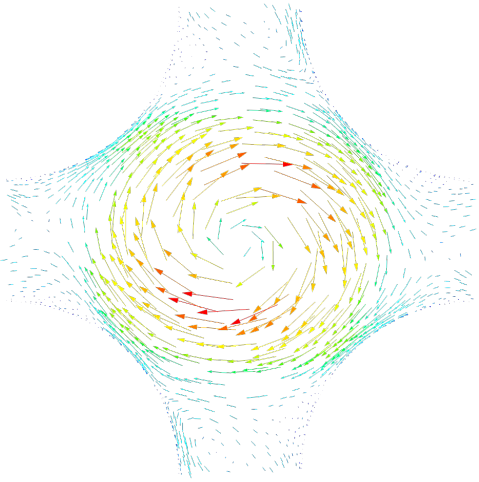

(c) Simulated lateral velocity vectors in the injection sub-channel at 150 mm from the back edge of the spacer body.

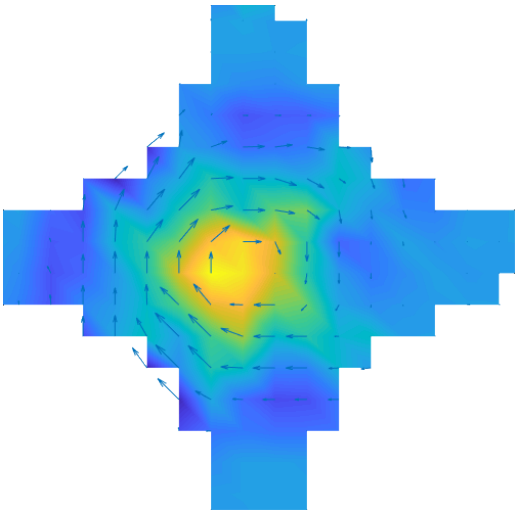

(d) Experimental lateral velocity vectors in the injection sub-channel at 150 mm from the back edge of the spacer body.

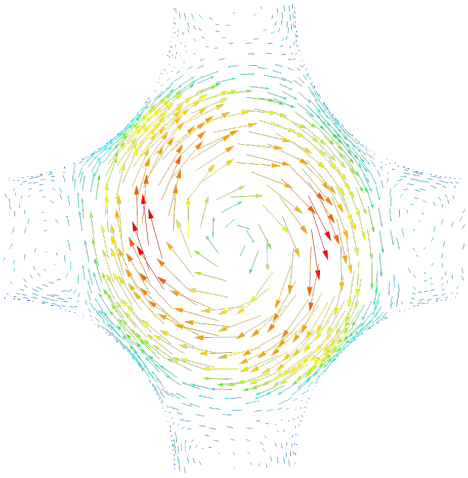

(e) Simulated lateral velocity vectors in the injection sub-channel at 250 mm from the back edge of the spacer body.

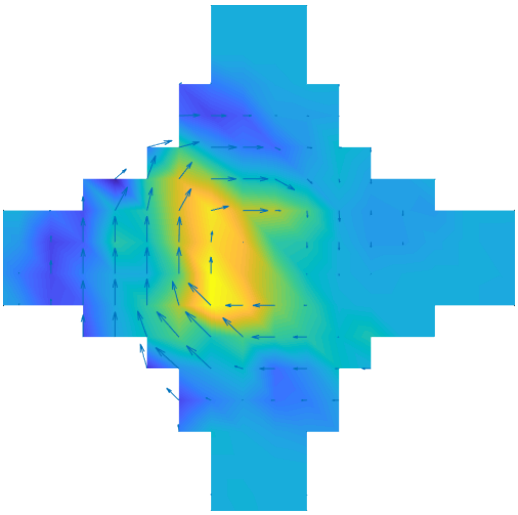

(f) Experimental lateral velocity vectors in the injection sub-channel at 250 mm from the back edge of the spacer body.

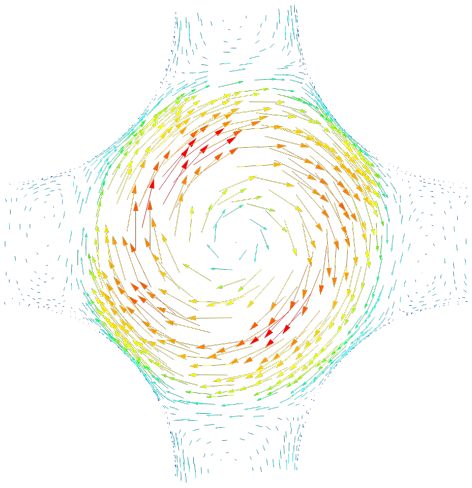

(a) Simulated lateral velocity vectors in the injection sub-channel at 350 mm from the back edge of the spacer body.

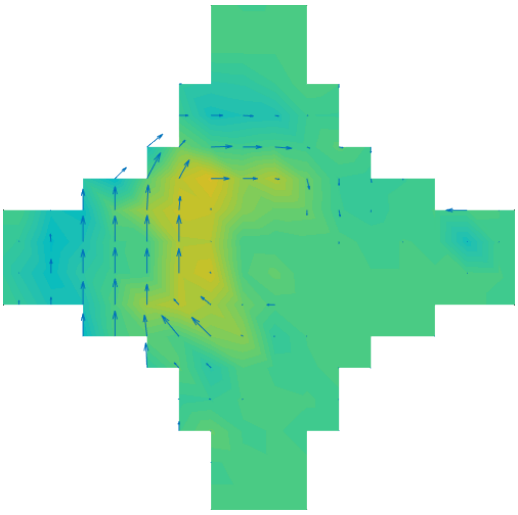

(b) Experimental lateral velocity vectors in the injection sub-channel at 350 mm from the back edge of the spacer body.

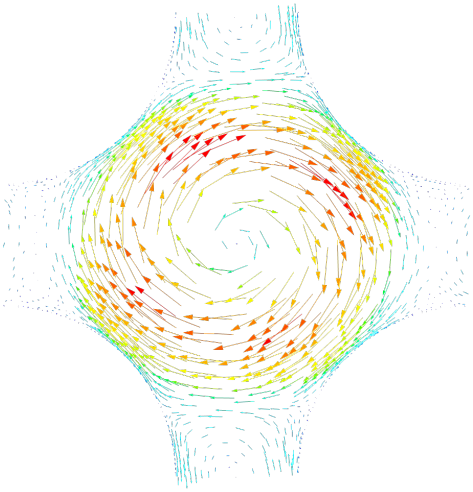

(c) Simulated lateral velocity vectors in the injection sub-channel at 450 mm from the back edge of the spacer body.

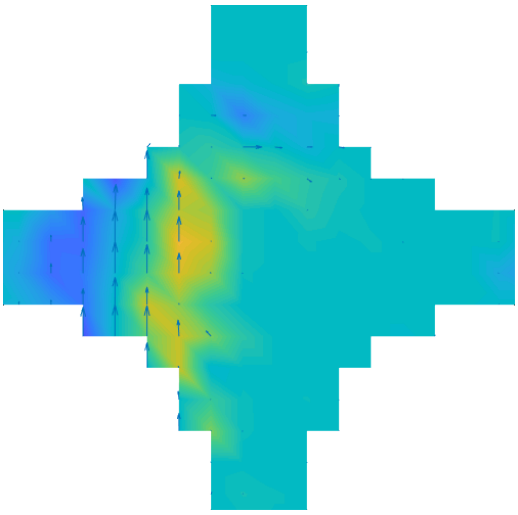

(d) Experimental lateral velocity vectors in the injection sub-channel at 450 mm from the back edge of the spacer body.

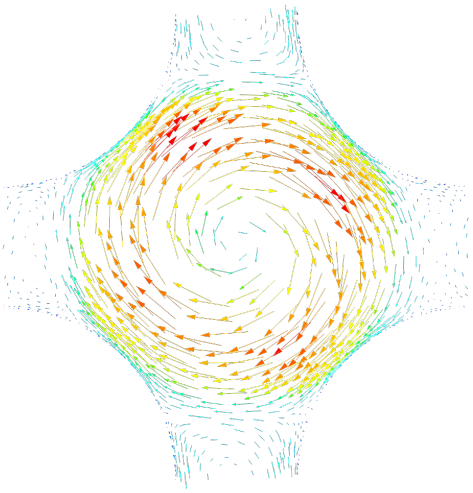

(e) Simulated lateral velocity vectors in the injection sub-channel at 550 mm from the back edge of the spacer body.

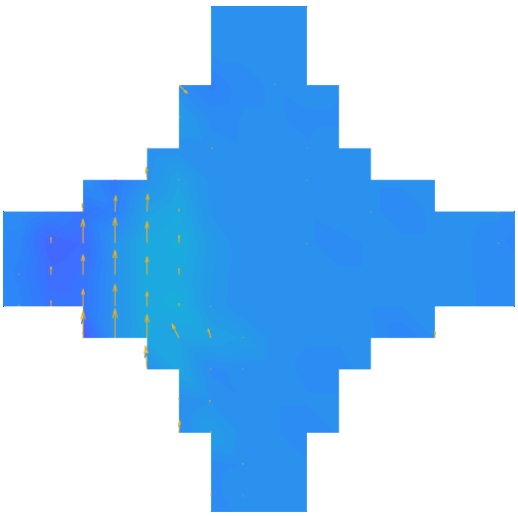

(f) Experimental lateral velocity vectors in the injection sub-channel at 550 mm from the back edge of the spacer body.

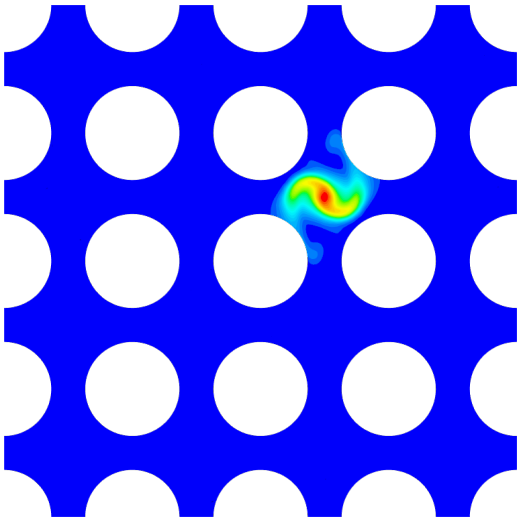

(a) Simulated tracer contour at 50 mm from the back edge of the spacer body.

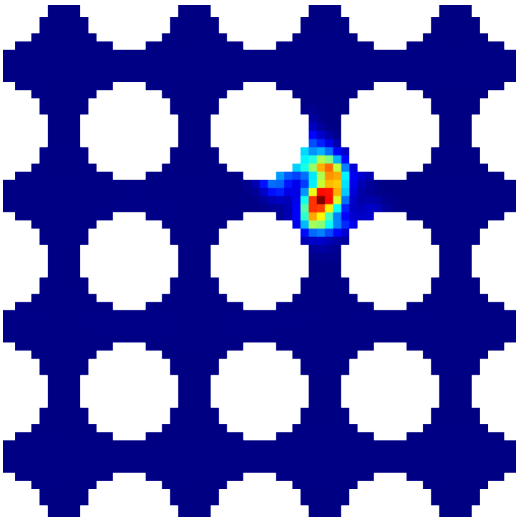

(b) Experimental tracer contour at 50 mm from the back edge of the spacer body.

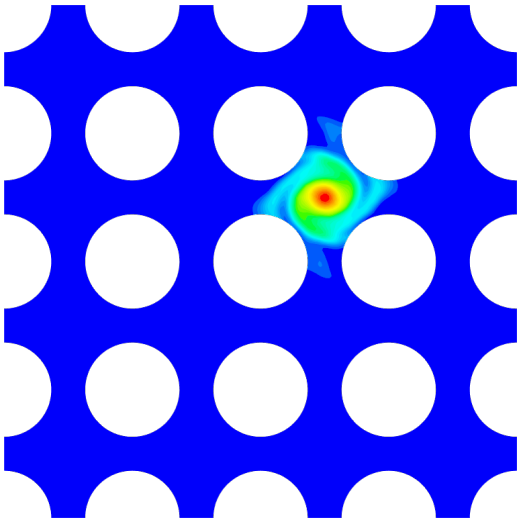

(c) Simulated tracer contour at 150 mm from the back edge of the spacer body.

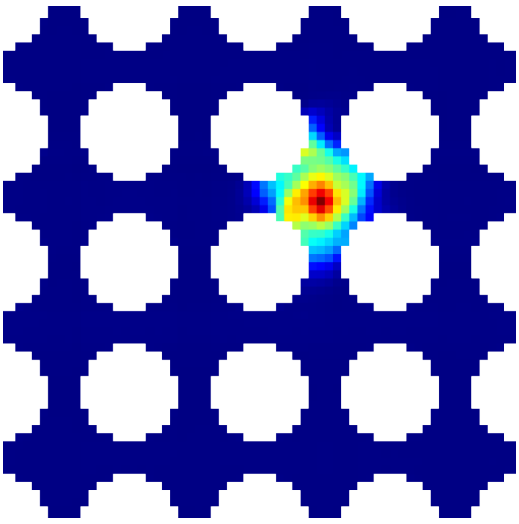

(d) Experimental tracer contour at 150 mm from the back edge of the spacer body.

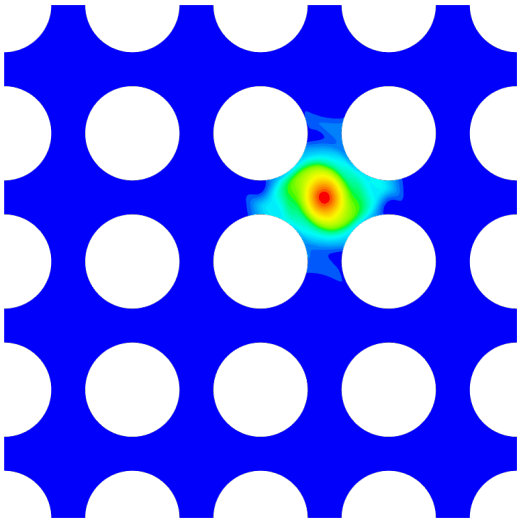

(e) Simulated tracer contour at 250 mm from the back edge of the spacer body.

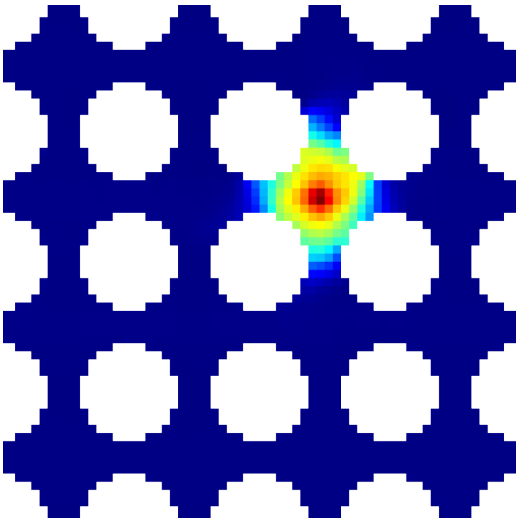

(f) Experimental tracer contour at 250 mm from the back edge of the spacer body.

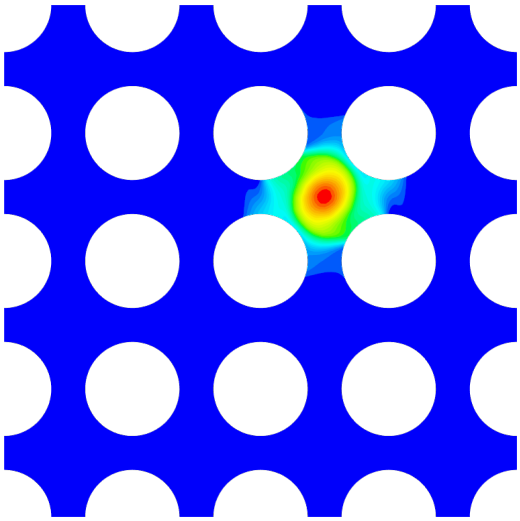

(a) Simulated tracer contour at 350 mm from the back edge of the spacer body.

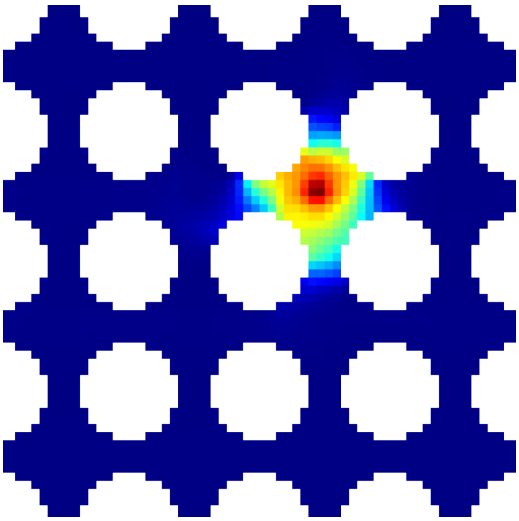

(b) Experimental tracer contour at 350 mm from the back edge of the spacer body.

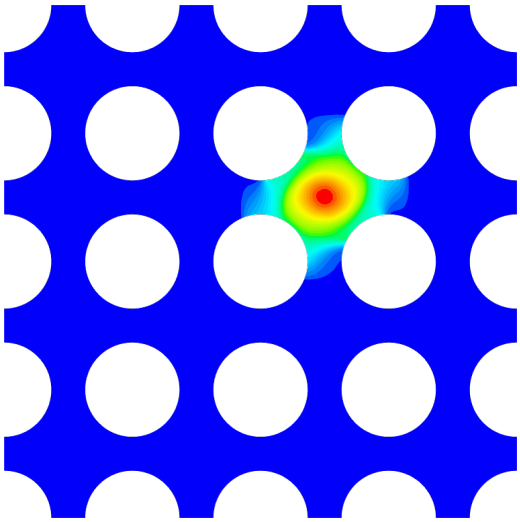

(c) Simulated tracer contour at 450 mm from the back edge of the spacer body.

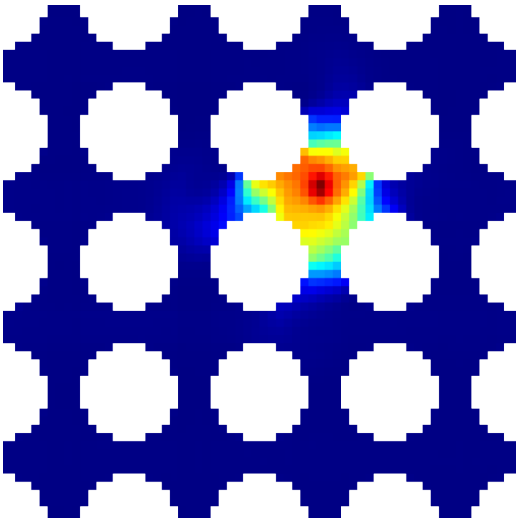

(d) Experimental tracer contour at 450 mm from the back edge of the spacer body.

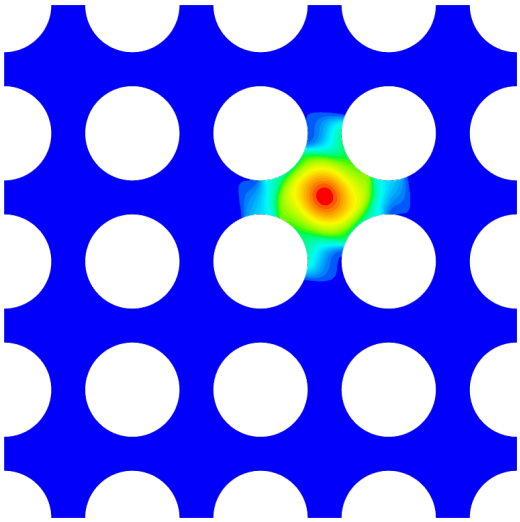

(e) Simulated tracer contour at 550 mm from the back edge of the spacer body.

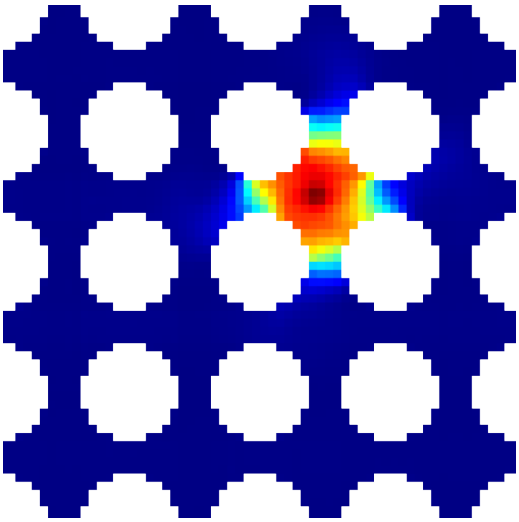

(f) Experimental tracer contour at 550 mm from the back edge of the spacer body.

Chapter 5

Summary and outlook

In this project, CFD methodologies have been developed to study the flow inside a 4x4 rod bundle with different spacers in a nuclear reactor.

For bare bundle case, a model with hexahedral mesh and periodic boundary conditions is used and mesh independence was achieved.

For cases with spacer and mixing vanes, the calculation domain was divided into different parts for a more efficient analysis in terms of computational resources. Two mesh strategies are proposed: hexahedral-trimmed hybrid mesh and automated / directed polyhedral mesh.

The trimmed part of the first mesh strategy did not achieve mesh convergence. On fine mesh, it was necessary to use unsteady solver, and fluctuating behaviours were observed in the flow field. Due to a time and computational capability limitation, the fine mesh was used for further calculations, but it is necessary to be cautious with the results, since future mesh validation is still needed.

Regarding the automated / directed polyhedral strategy, mesh convergence was achieved with respect to tracer share and swirl decay.

The following four simulations were performed using the two mentioned meshes and two different turbulence models:

- Hexahedral-Trimmed mesh with k-ω turbulence model.
- Hexahedral-Trimmed mesh with V^2F k-ε turbulence model.
- Polyhedral mesh with k-ω turbulence model.
- Polyhedral mesh with V^2F k-ε turbulence model.

From the results, it can be concluded that polyhedral mesh with k-ω turbulence model and also the hexahedral-trimmed mesh with V^2F k-ε turbulence model have relatively better performances compared to the other two. However, due to limited time, the simulations for spacers 2, 3 and 4 were performed only on the polyhedral mesh with k-ω turbulence model.

Looking at the simulations of different spacer vane configurations, it could be concluded that, with respect to the tracer share, only the case of spacer 1 (Standard, 30°) was predicted with acceptable discrepancy; swirl decay rate was obviously slower than the experimental one. Discrepancies in cases of other spacer and mixing vanes configurations are quite large.

It is worth attention that the preliminary results from the simulation with V^2F k-ε model showed promising results. Thanks to the fine mesh and the unsteady solver used for the calculations, it was possible predict the instabilities in the flow, which enhanced the lateral mixing between sub-channels.

Future work

Further studies with hybrid mesh and V^2F k-ε model are recommended, performing time-step and mesh sensitivity analysis to be able to capture the dynamic behaviour of the flow and predict mixing phenomenon better.

It could also be a promising idea to consider the local effect of the wire mesh sensor and include it in the simulations to see the influence of an additional small pressure drop on the flow field.

Appendix A

Extra figures

The data acquisition and posterior post-processing of the simulations generated a very big amount of graphical information. This appendix tries to summarize all the figures so that they can be easily found and referenced in chapter 4.

However, the most important and characteristic figures in the appendix were also placed in the chapter body for the convenience of the reader.

A.1 Trimmed mesh study - 2^{nd} part

Spacer region

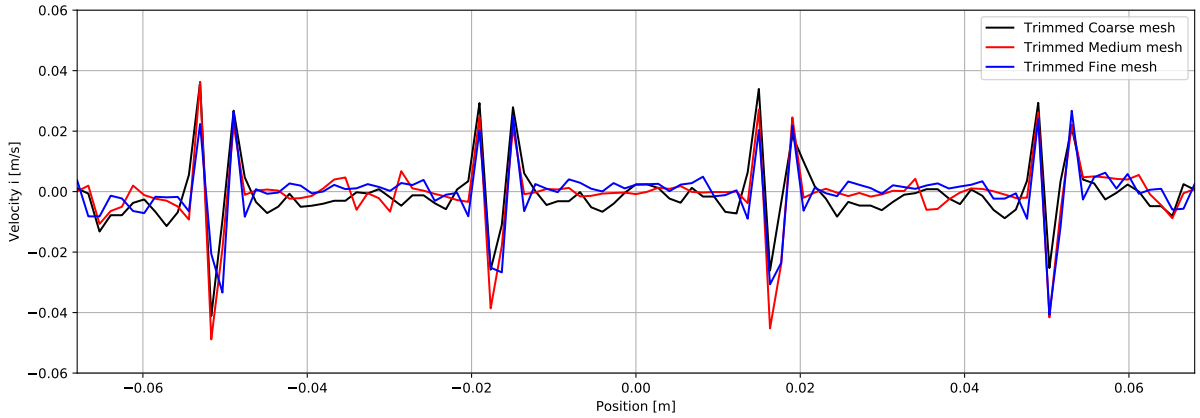

Figure A.1: i component of velocity along the probe line in a plane cutting the spacer body.

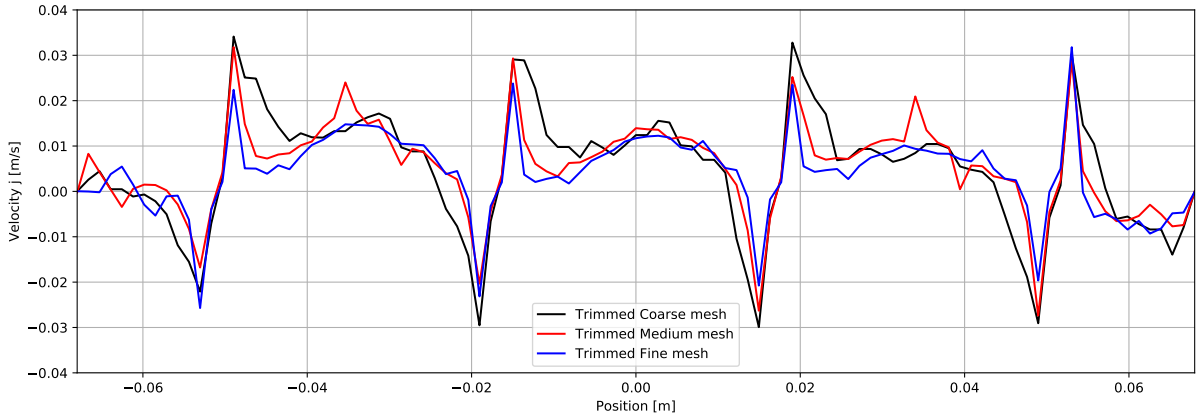

Figure A.2: j component of velocity along the probe line in a plane cutting the spacer body.

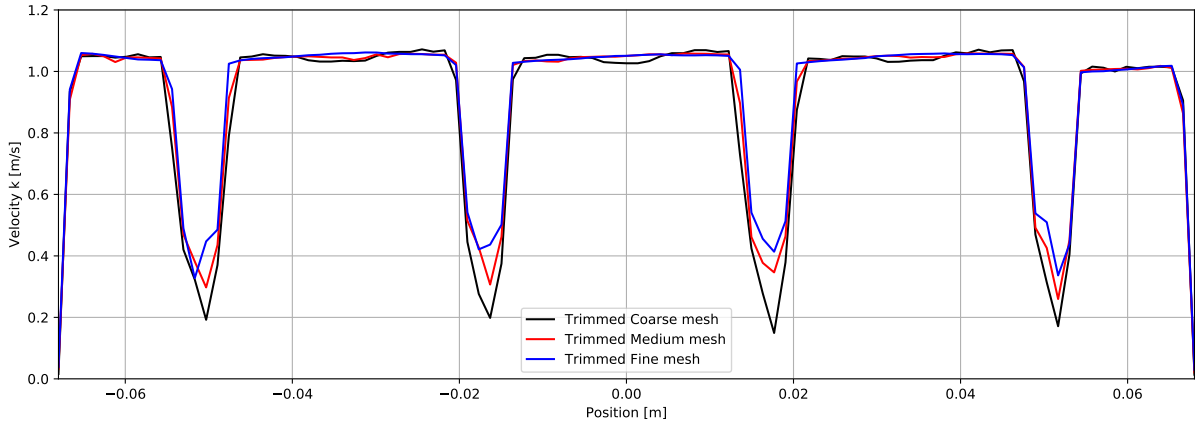

Figure A.3: k component of velocity along the probe line in a plane cutting the spacer body.

Vanes region

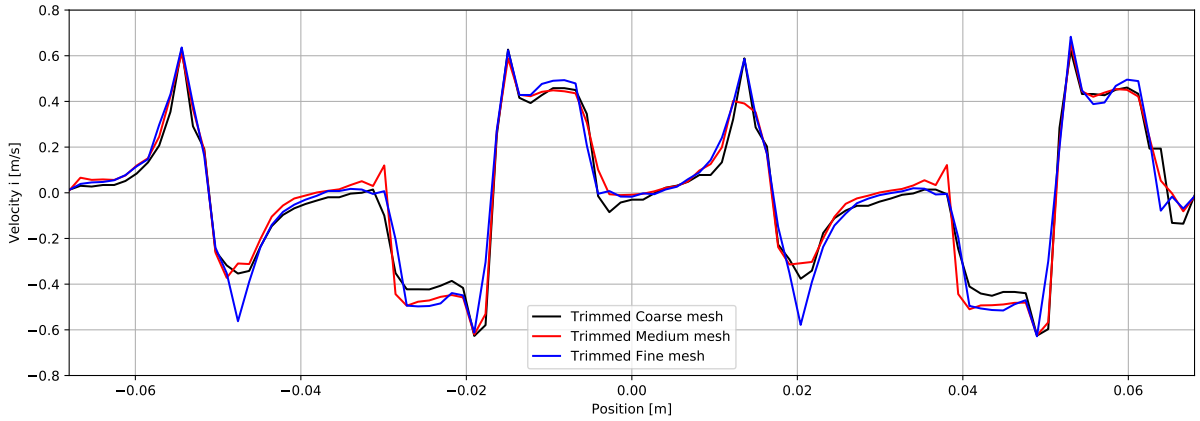

Figure A.4: i component of velocity along the probe line in a plane cutting the vanes.

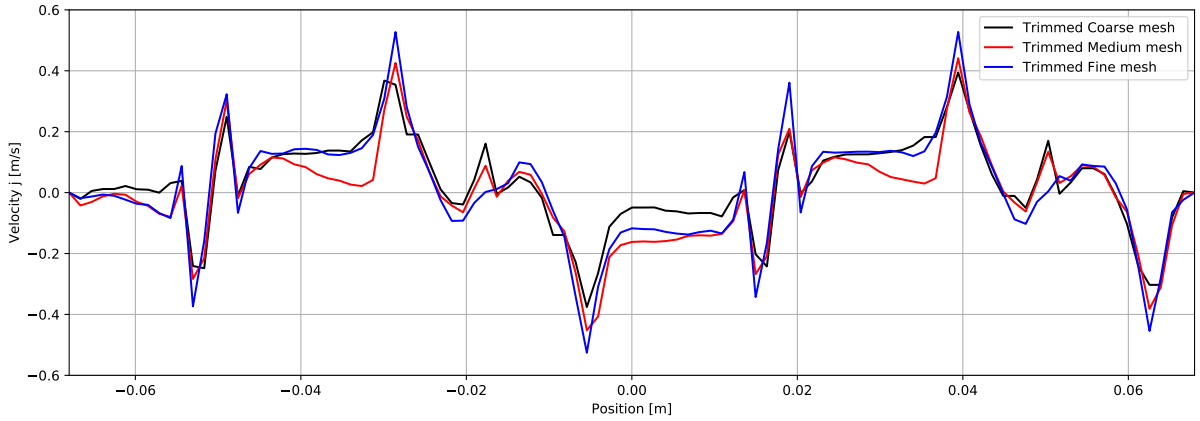

Figure A.5: j component of velocity along the probe line in a plane cutting the vanes.

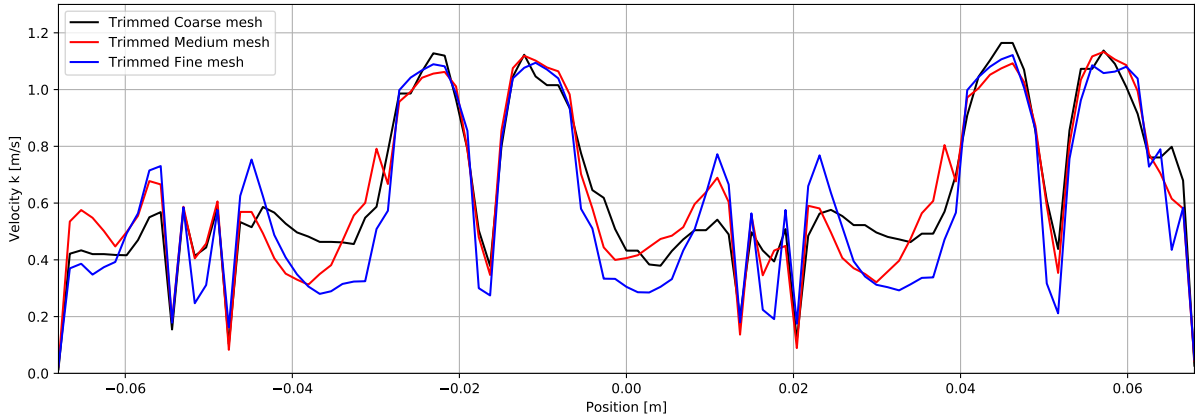

Figure A.6: k component of velocity along the probe line in a plane cutting the vanes.

Near 2^{nd} region outlet

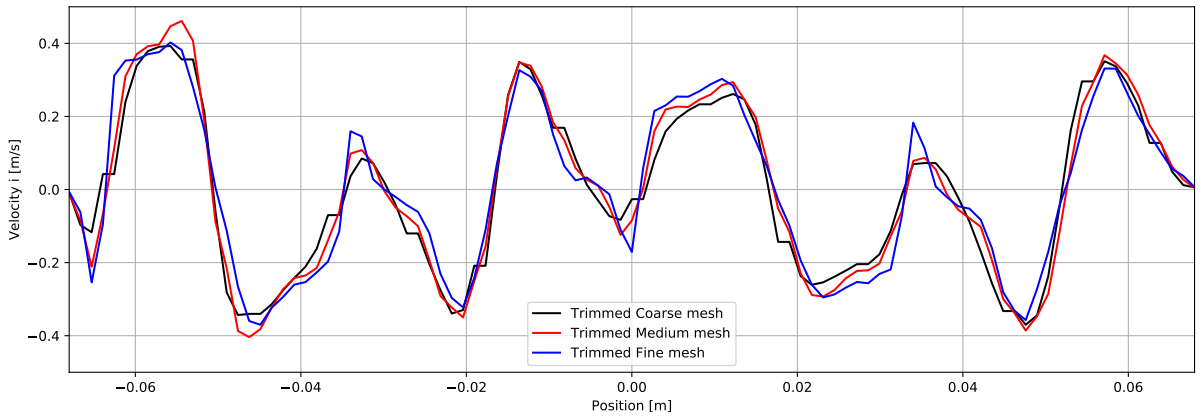

Figure A.7: i component of velocity along the probe line in a plane near the outlet of the second region.

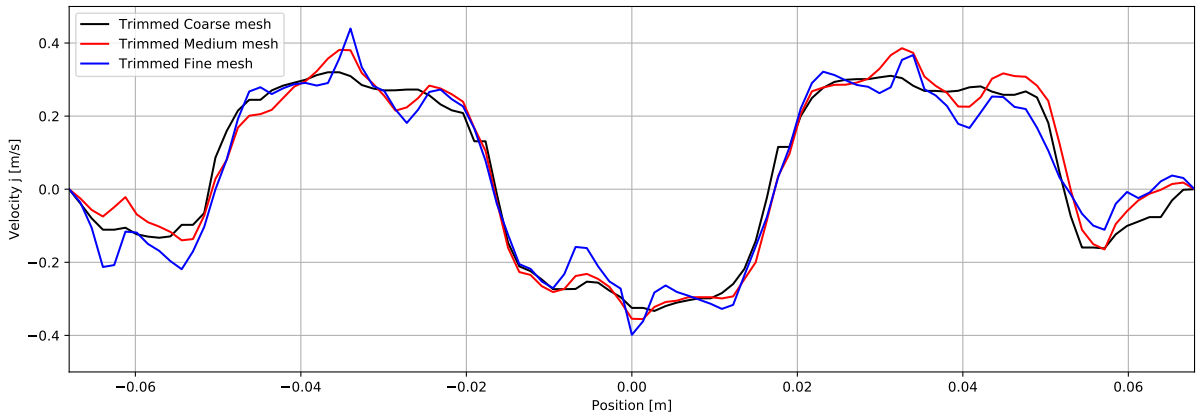

Figure A.8: j component of velocity along the probe line in a plane near the outlet of the second region.

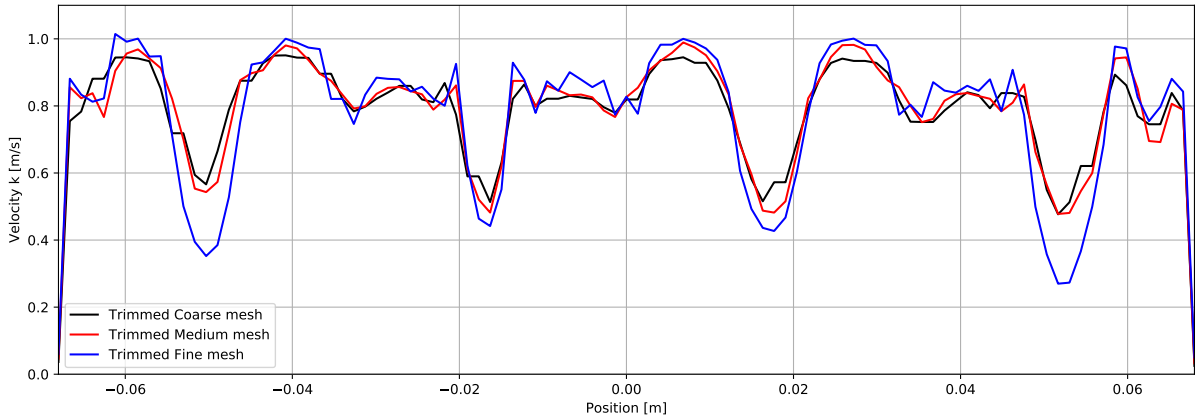

Figure A.9: k component of velocity along the probe line in a plane near the outlet of the second region.

A.2 Polyhedral mesh study - 2^{nd} part

Spacer region

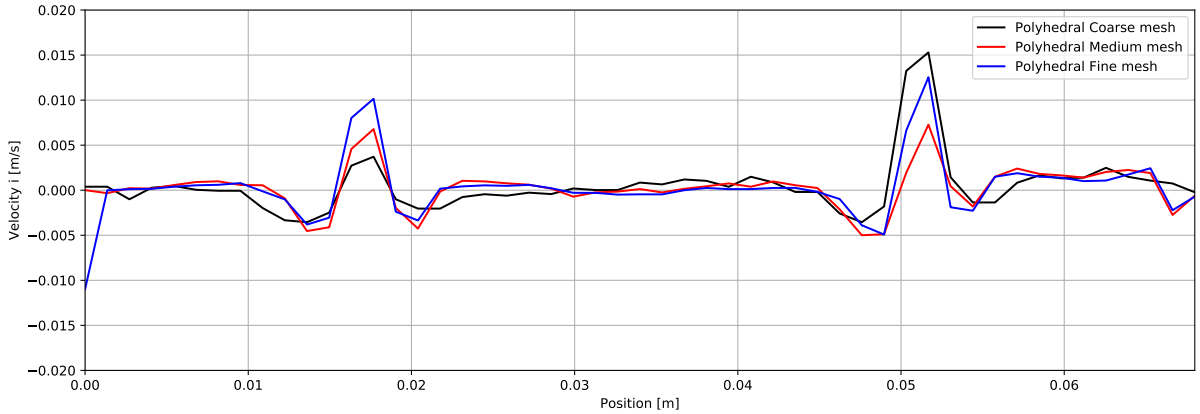

Figure A.10: i component of velocity along the probe line in a plane cutting the spacer body.

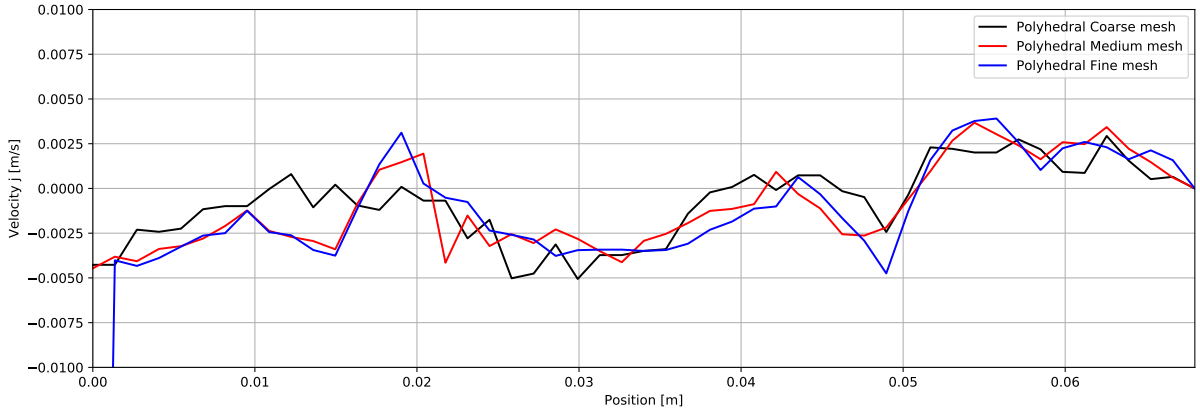

Figure A.11: j component of velocity along the probe line in a plane cutting the spacer body.

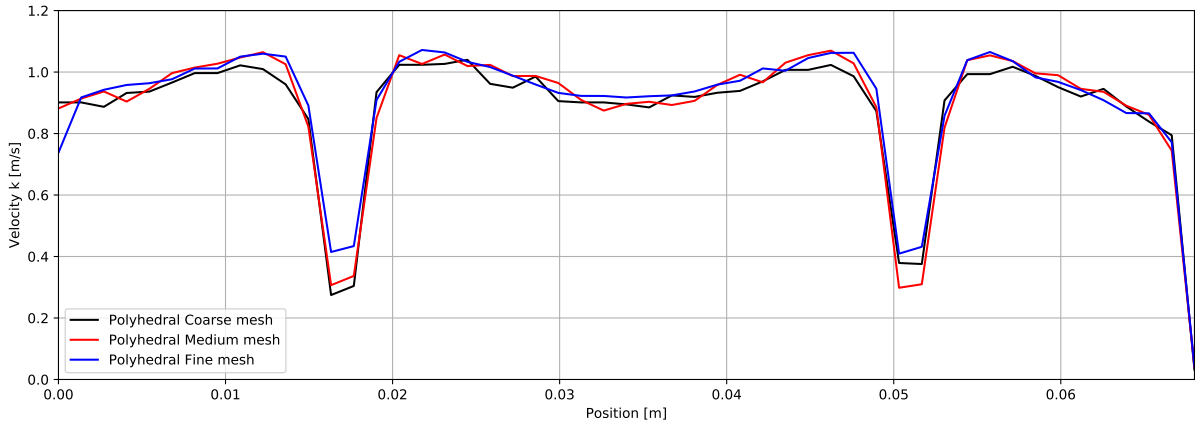

Figure A.12: k component of velocity along the probe line in a plane cutting the spacer body.

Vanes region

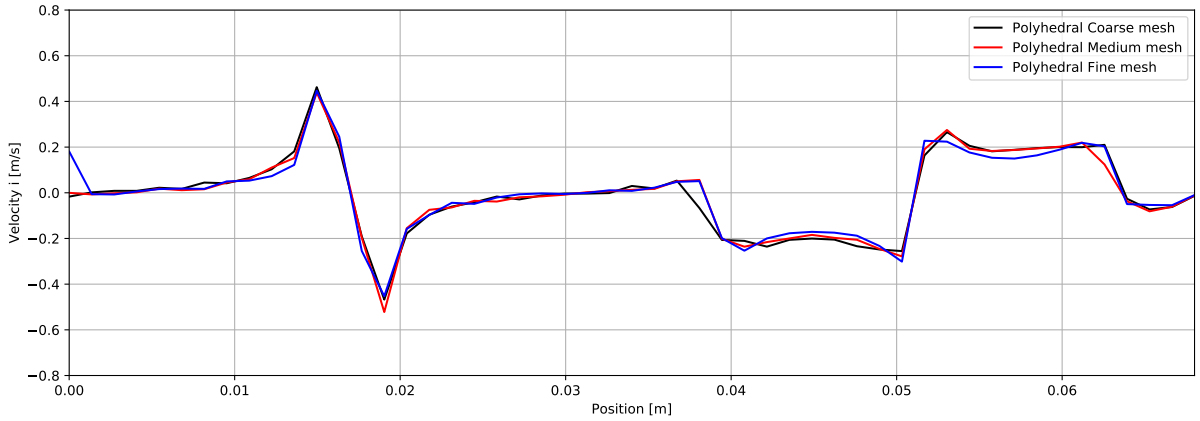

Figure A.13: i component of velocity along the probe line in a plane cutting the vanes.

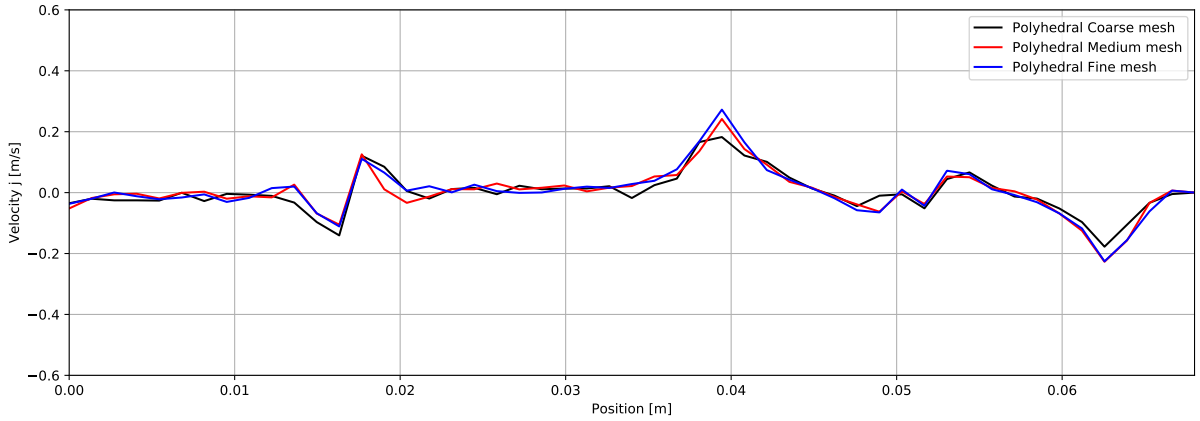

Figure A.14: j component of velocity along the probe line in a plane cutting the vanes.

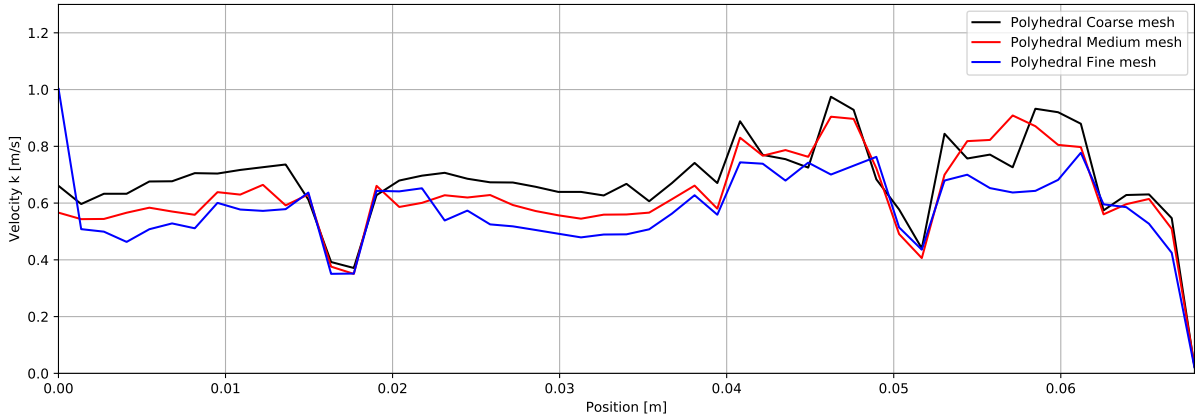

Figure A.15: k component of velocity along the probe line in a plane cutting the vanes.

Near 2^{nd} region outlet

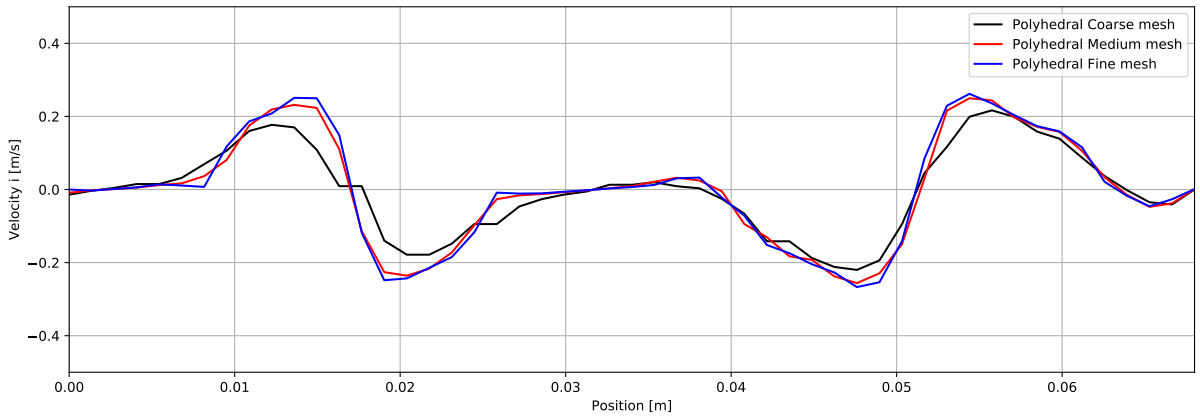

Figure A.16: i component of velocity along the probe line in a plane near the outlet of the second region.

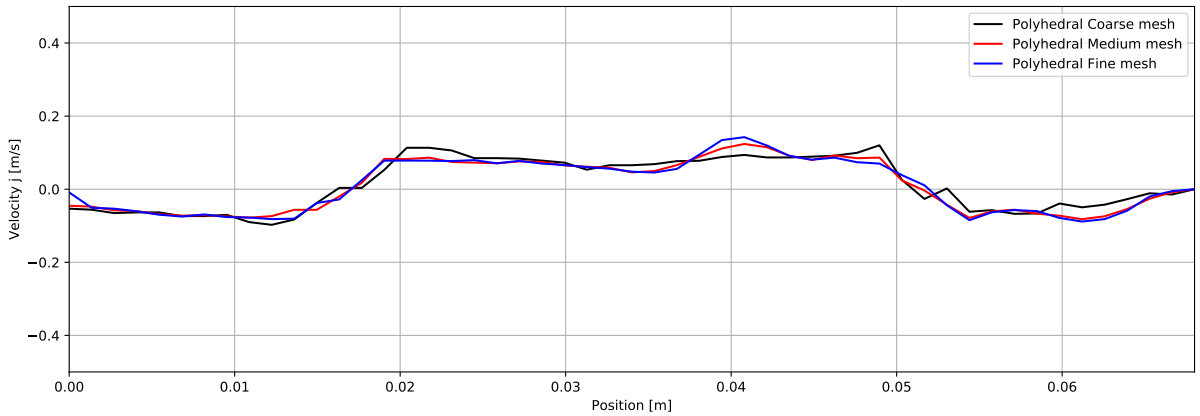

Figure A.17: j component of velocity along the probe line in a plane near the outlet of the second region.

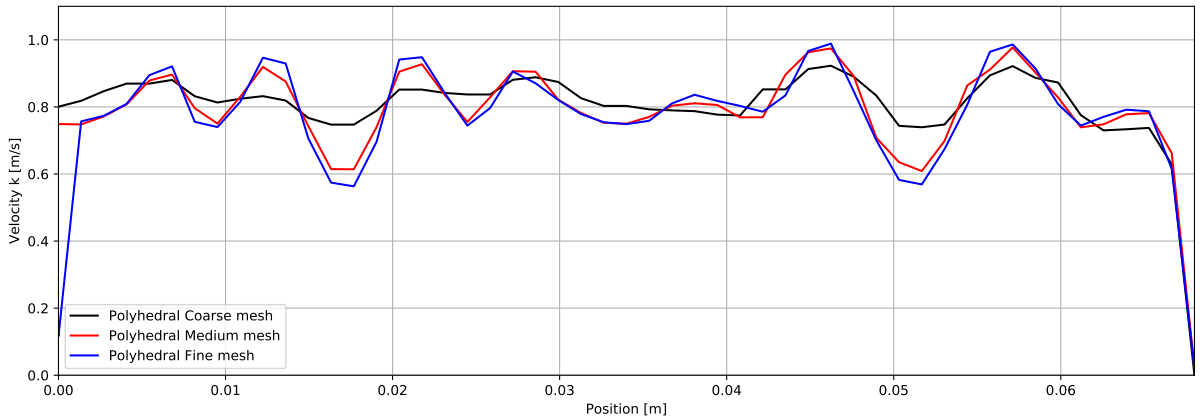

Figure A.18: k component of velocity along the probe line in a plane near the outlet of the second region.

A.3 Polyhedral mesh study - 3^{rd} part

50 mm measurements

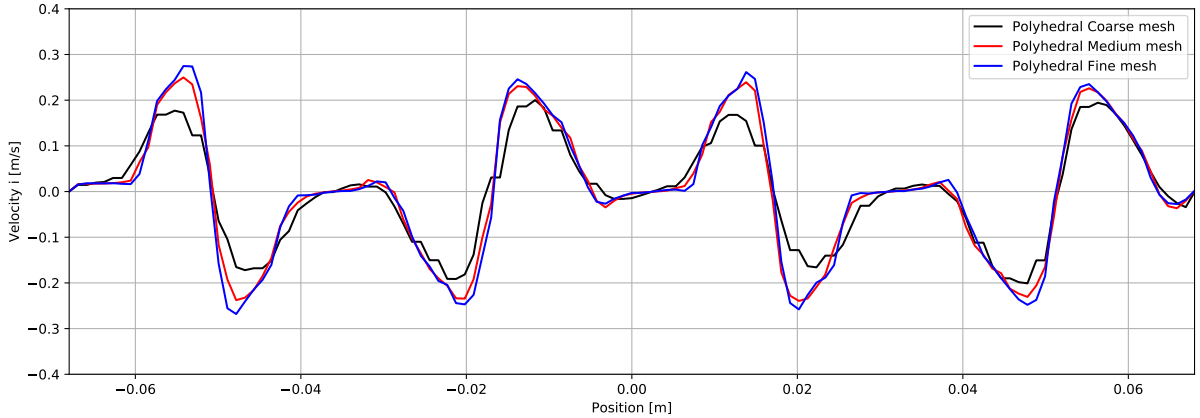

Figure A.19: i component of velocity along the probe line in a plane 50 mm from the tip of the spacer body.

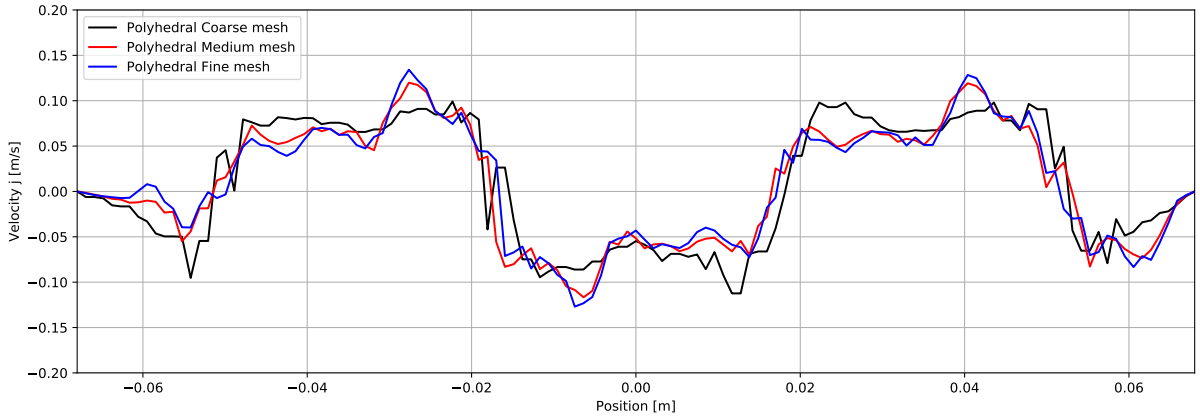

Figure A.20: j component of velocity along the probe line in a plane 50 mm from the tip of the spacer body.

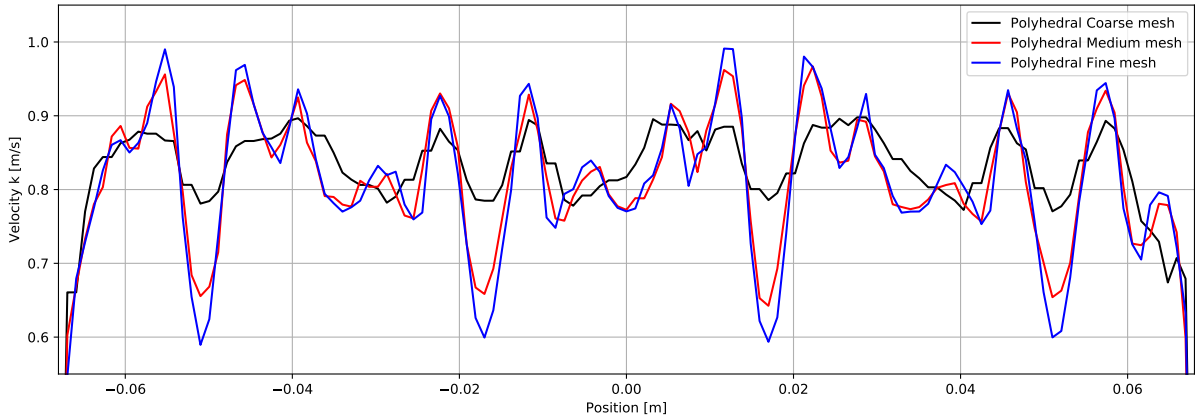

Figure A.21: k component of velocity along the probe line in a plane 50 mm from the tip of the spacer body.

150 mm measurements

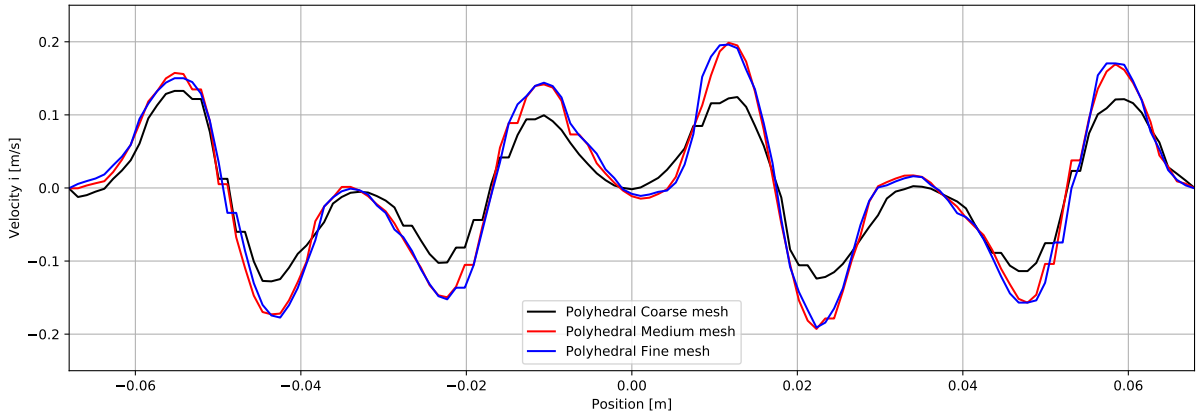

Figure A.22: i component of velocity along the probe line in a plane 150 mm from the tip of the spacer body.

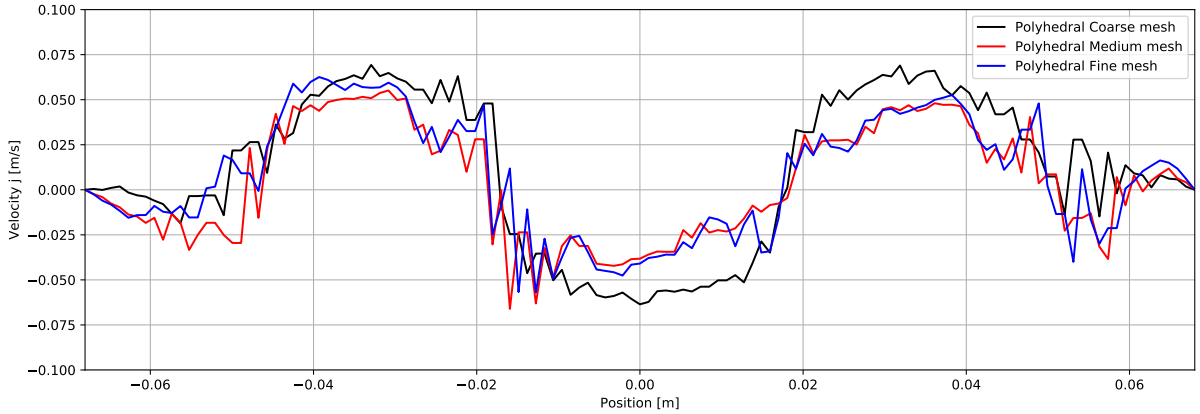

Figure A.23: j component of velocity along the probe line in a plane 150 mm from the tip of the spacer body.

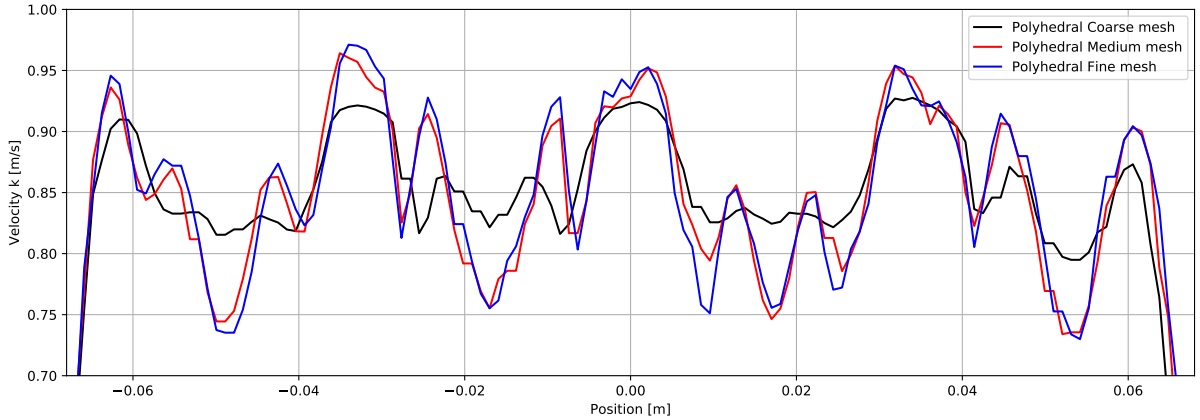

Figure A.24: k component of velocity along the probe line in a plane 150 mm from the tip of the spacer body.

250 mm measurements

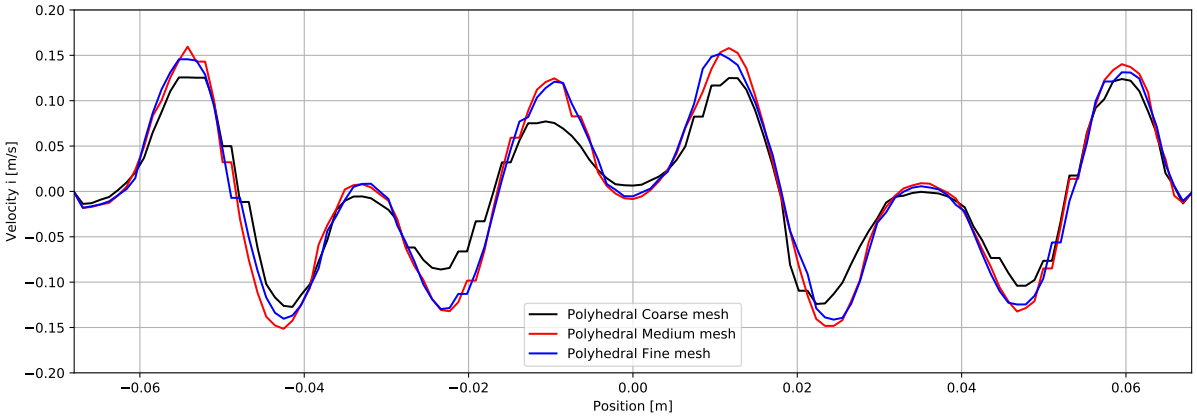

Figure A.25: i component of velocity along the probe line in a plane 250 mm from the tip of the spacer body.

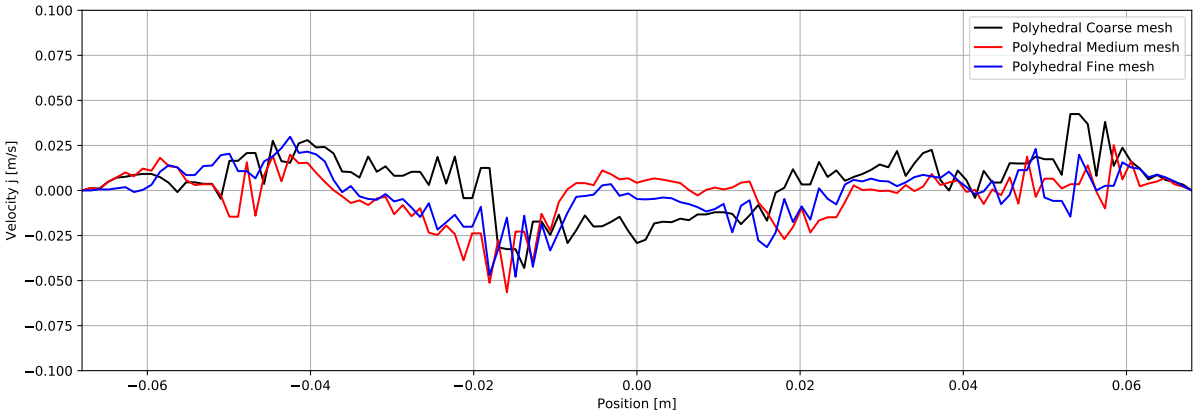

Figure A.26: j component of velocity along the probe line in a plane 250 mm from the tip of the spacer body.

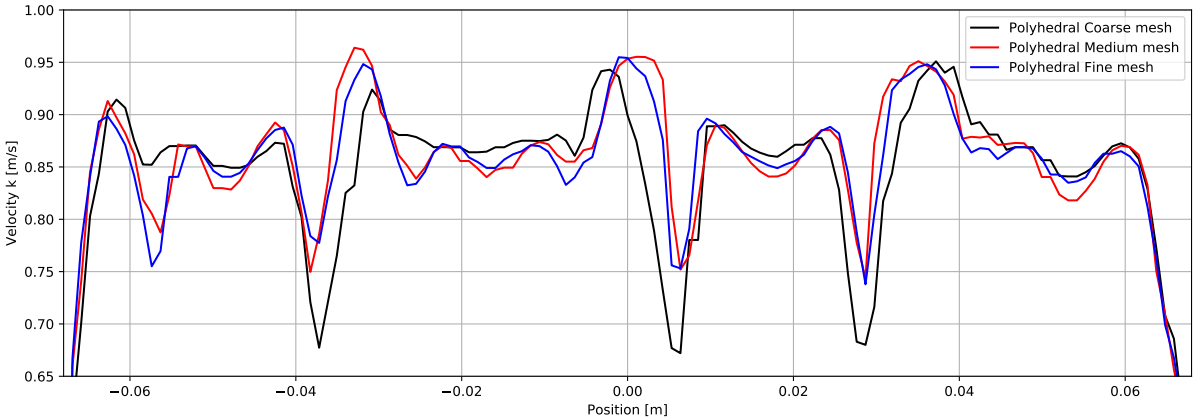

Figure A.27: k component of velocity along the probe line in a plane 250 mm from the tip of the spacer body.

350 mm measurements

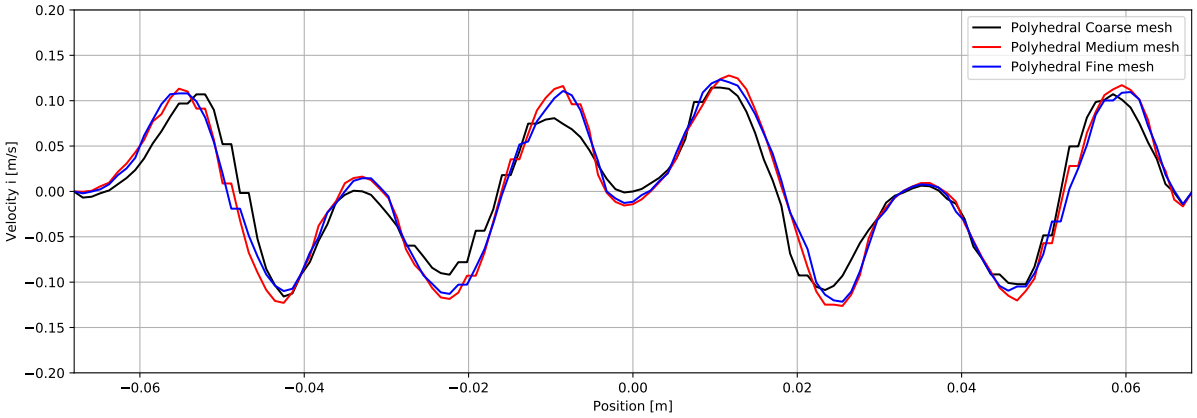

Figure A.28: i component of velocity along the probe line in a plane 350 mm from the tip of the spacer body.

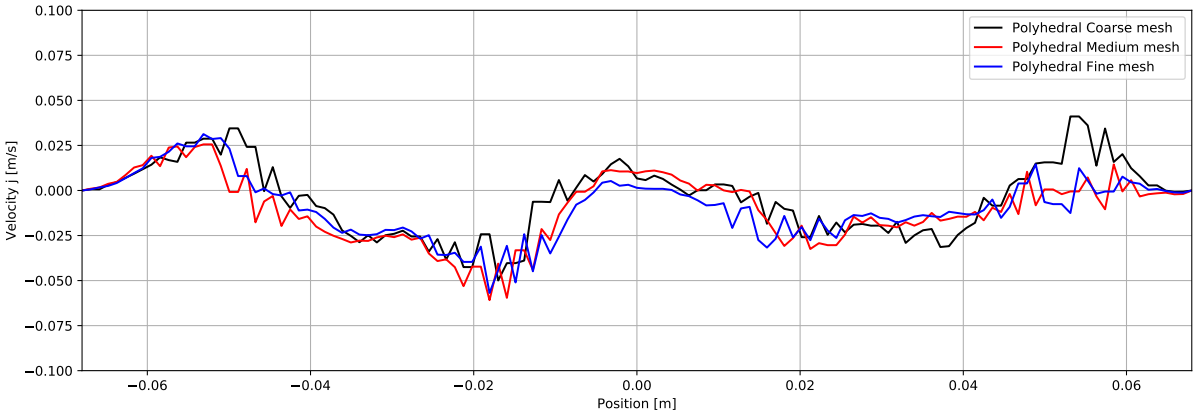

Figure A.29: j component of velocity along the probe line in a plane 350 mm from the tip of the spacer body.

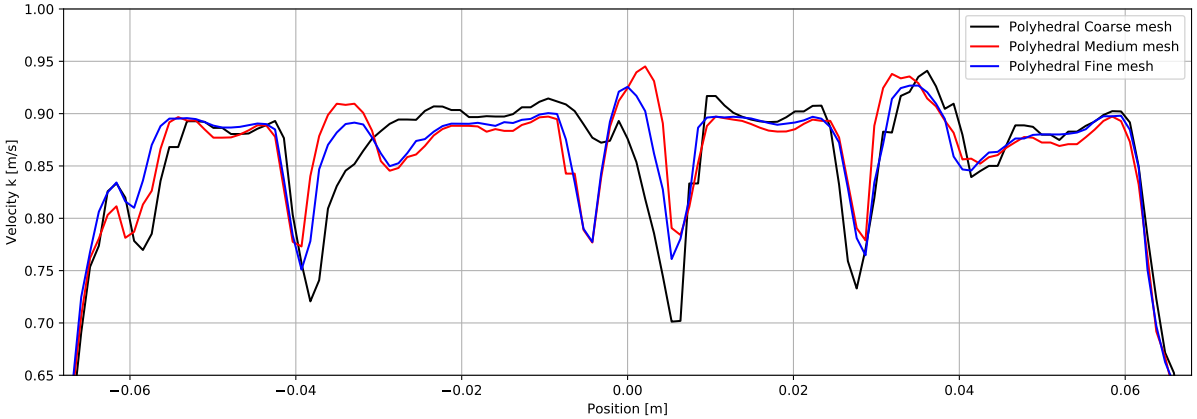

Figure A.30: k component of velocity along the probe line in a plane 350 mm from the tip of the spacer body.

450 mm measurements

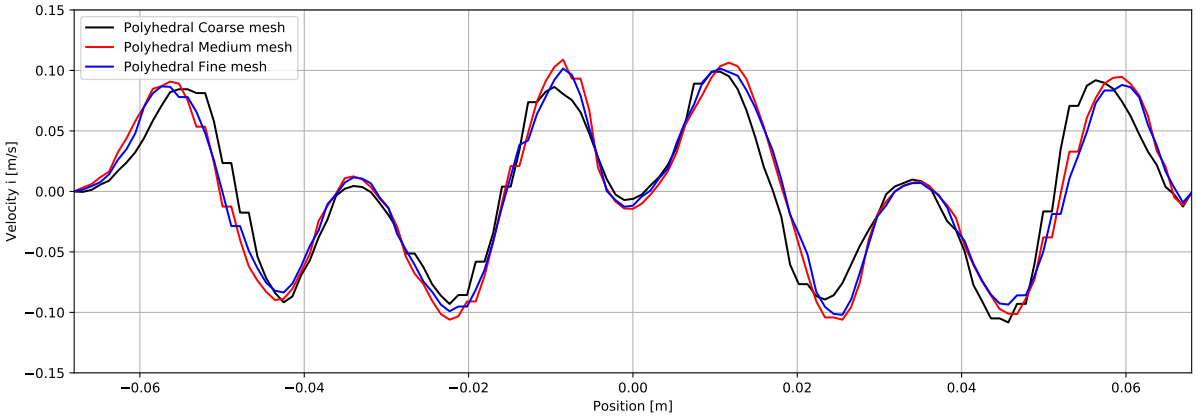

Figure A.31: i component of velocity along the probe line in a plane 450 mm from the tip of the spacer body.

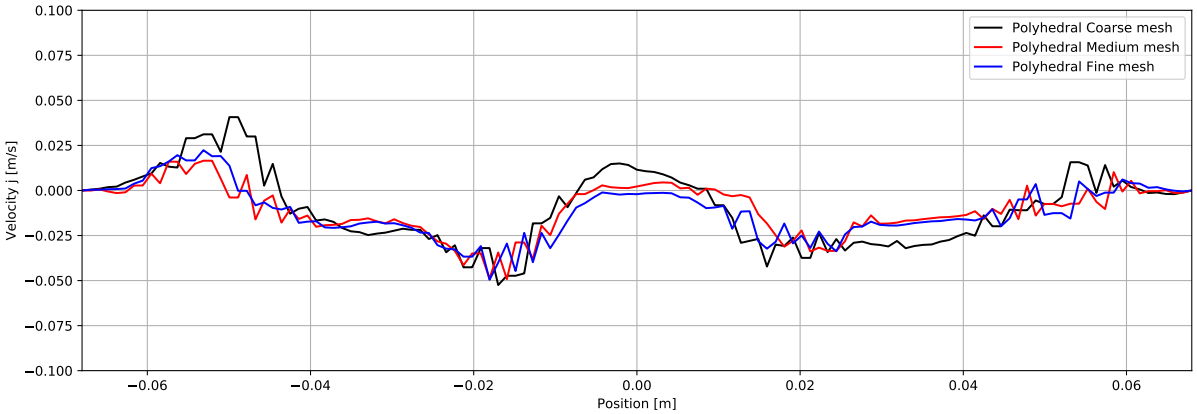

Figure A.32: j component of velocity along the probe line in a plane 450 mm from the tip of the spacer body.

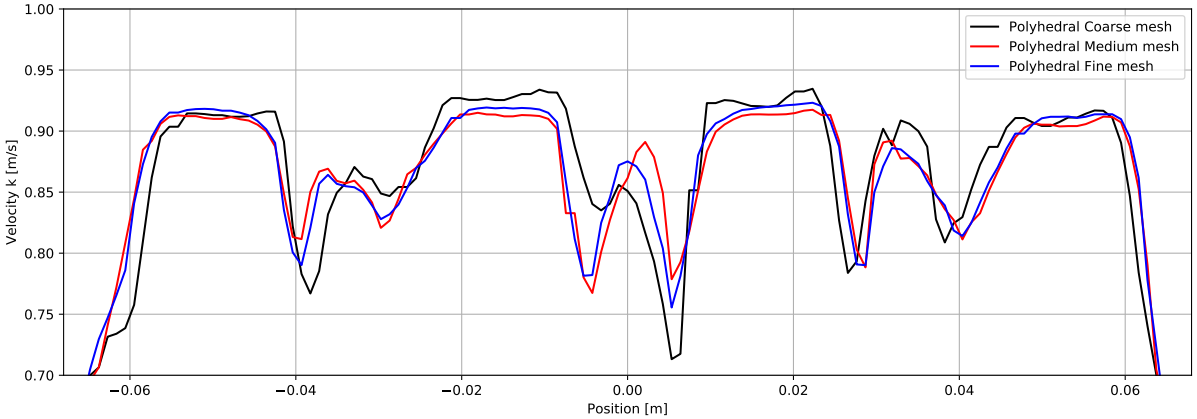

Figure A.33: k component of velocity along the probe line in a plane 450 mm from the tip of the spacer body.

550 mm measurements

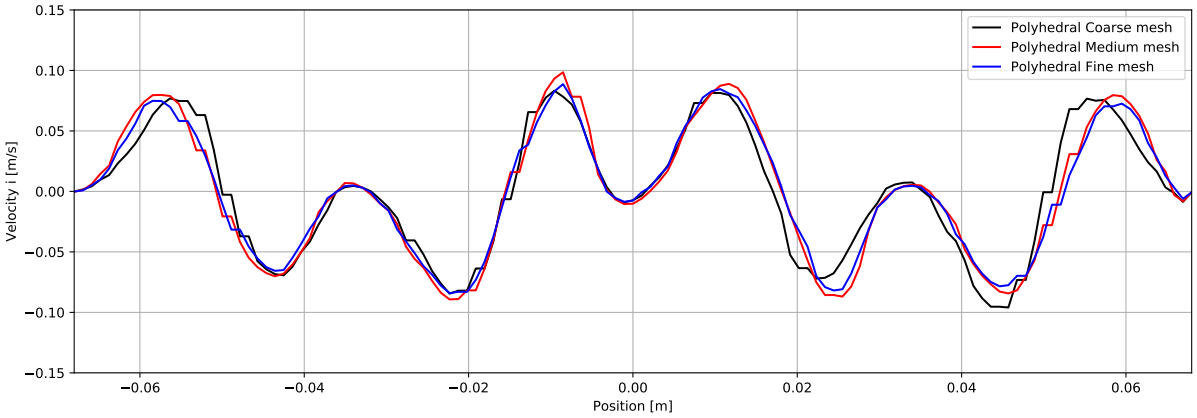

Figure A.34: i component of velocity along the probe line in a plane 550 mm from the tip of the spacer body.

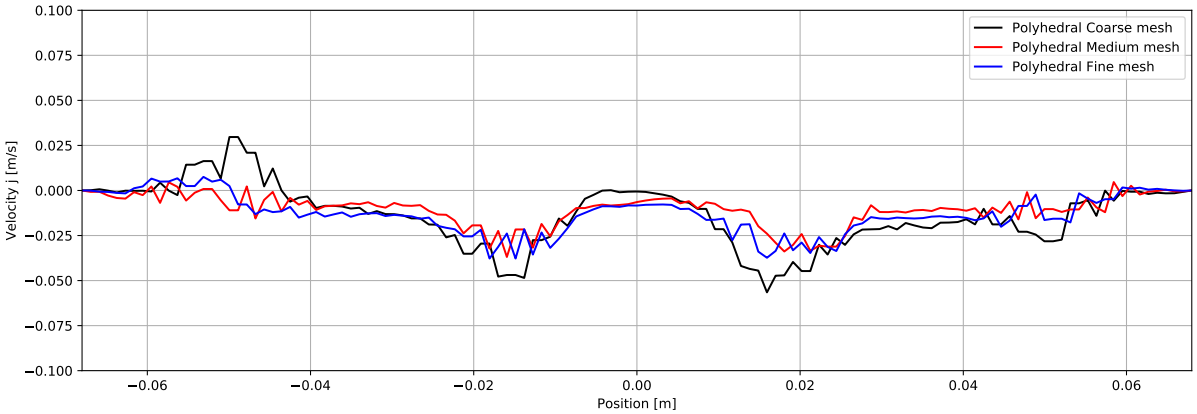

Figure A.35: j component of velocity along the probe line in a plane 550 mm from the tip of the spacer body.

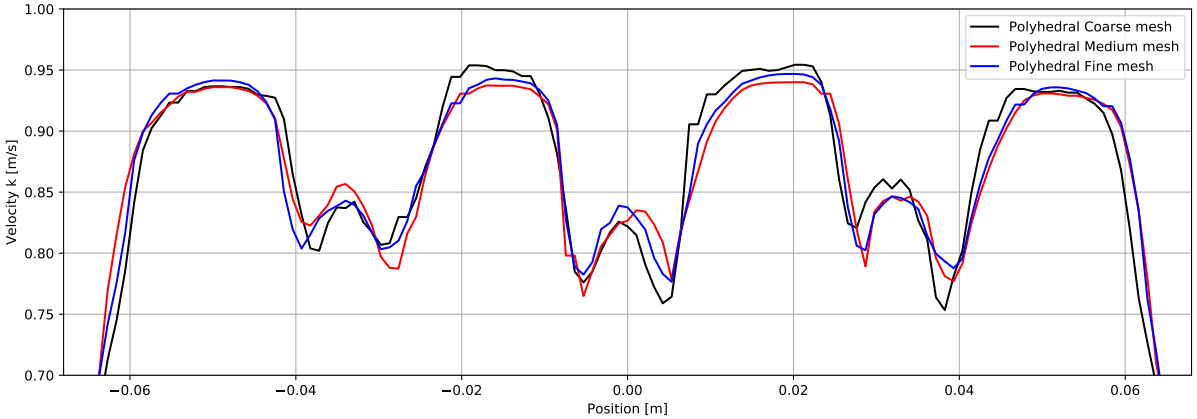

Figure A.36: k component of velocity along the probe line in a plane 550 mm from the tip of the spacer body.

A.4 Turbulence analysis

50 mm measurements

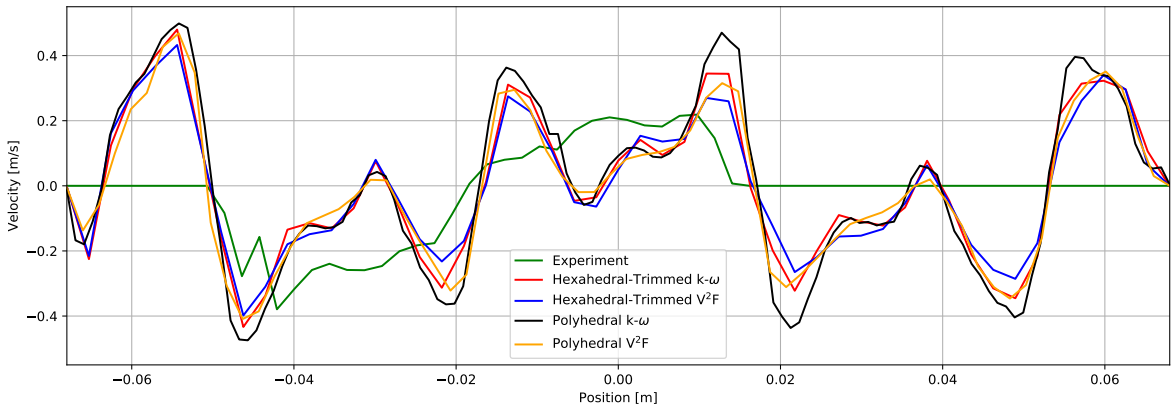

Figure A.37: i component of velocity along the probe line in a plane 50 mm from the tip of the spacer body.

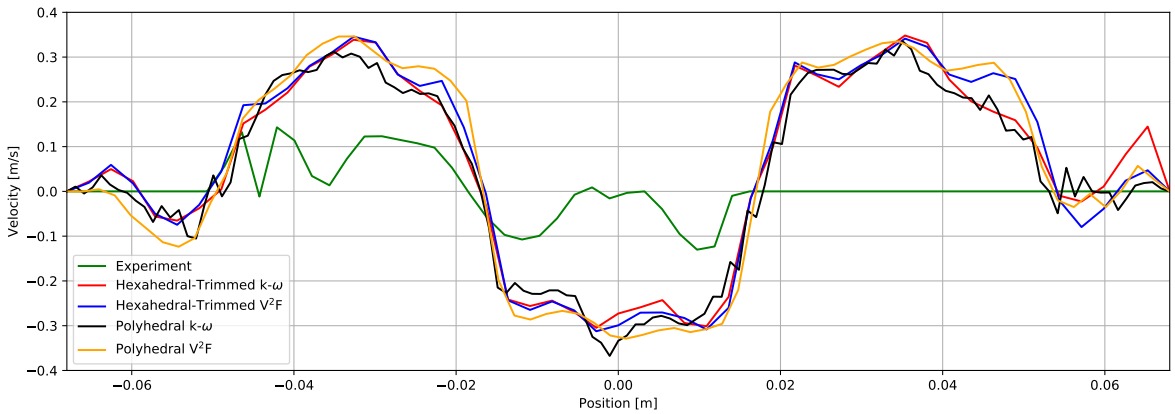

Figure A.38: j component of velocity along the probe line in a plane 50 mm from the tip of the spacer body.

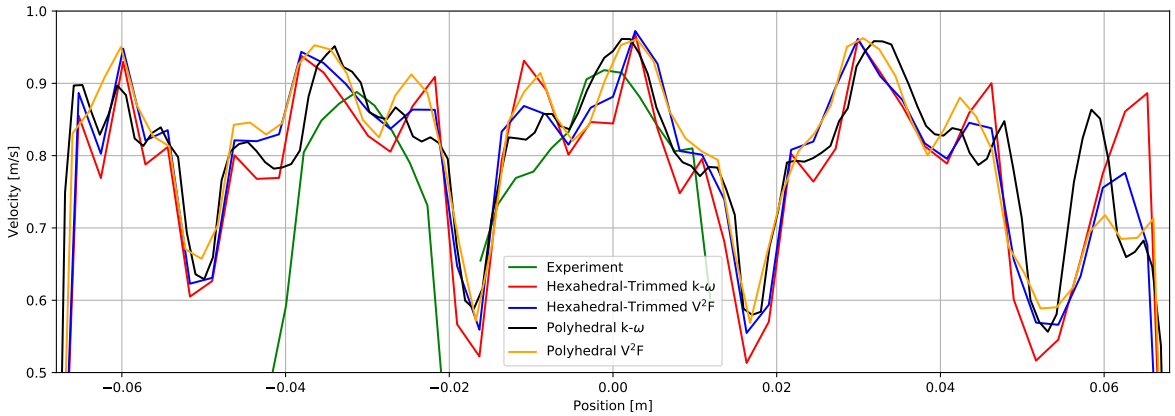

Figure A.39: k component of velocity along the probe line in a plane 50 mm from the tip of the spacer body.

150 mm measurements

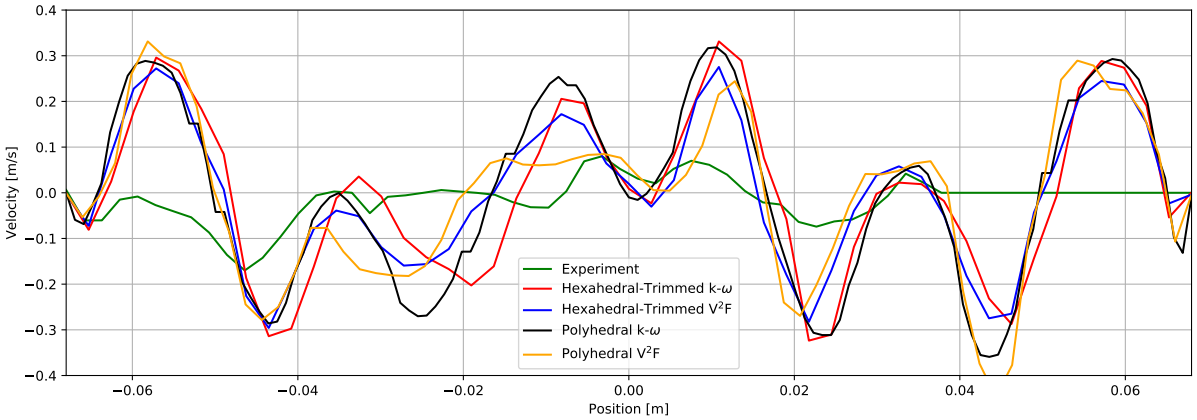

Figure A.40: i component of velocity along the probe line in a plane 150 mm from the tip of the spacer body.

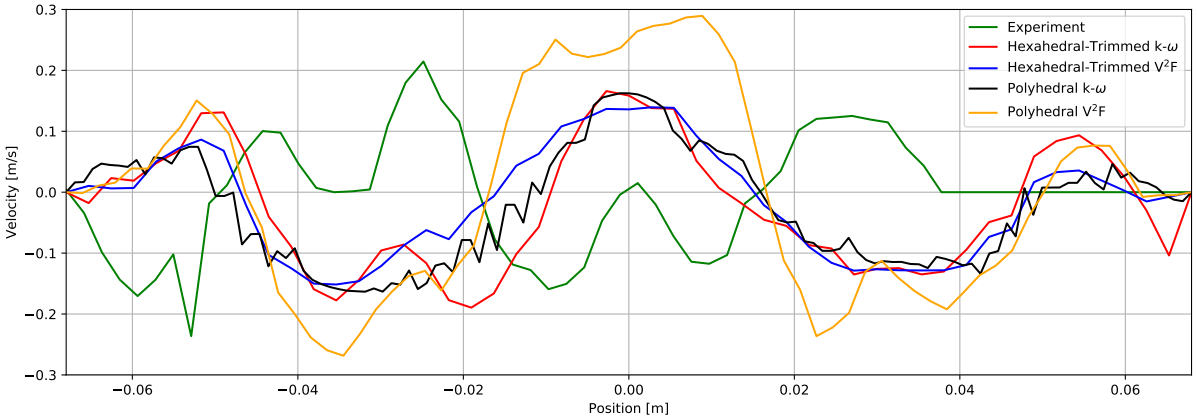

Figure A.41: j component of velocity along the probe line in a plane 150 mm from the tip of the spacer body.

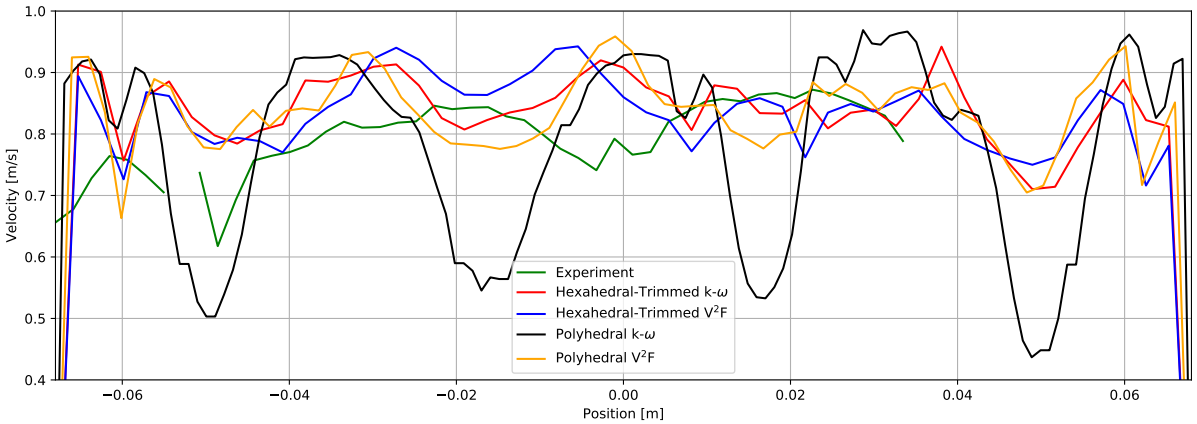

Figure A.42: k component of velocity along the probe line in a plane 150 mm from the tip of the spacer body.

250 mm measurements

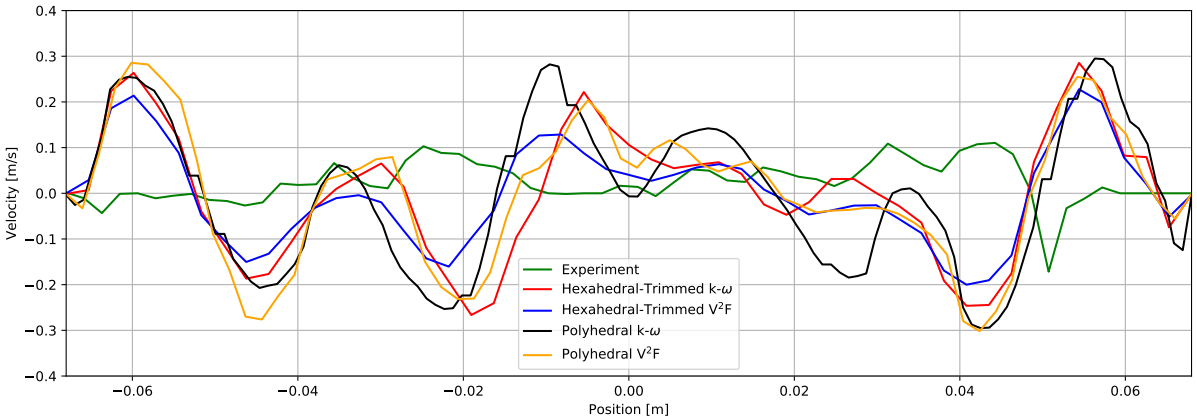

Figure A.43: i component of velocity along the probe line in a plane 250 mm from the tip of the spacer body.

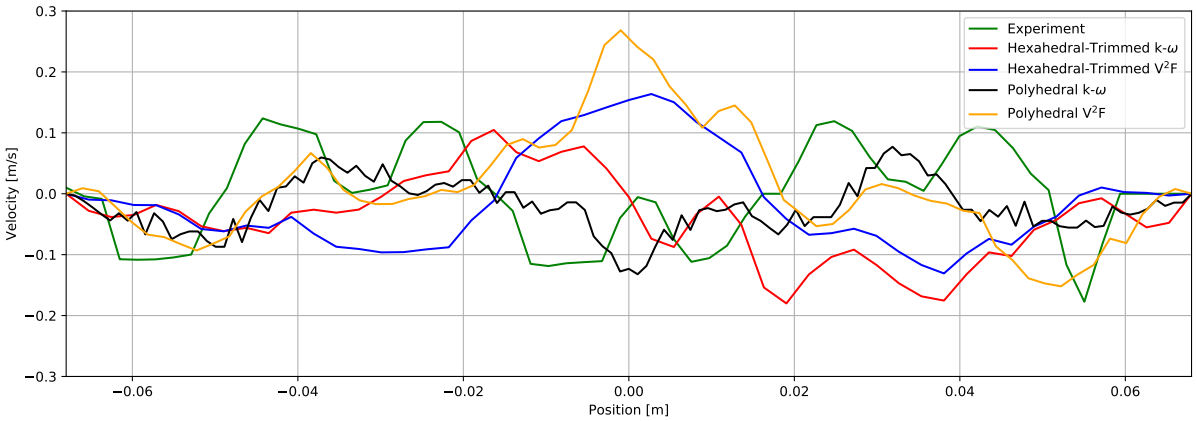

Figure A.44: j component of velocity along the probe line in a plane 250 mm from the tip of the spacer body.

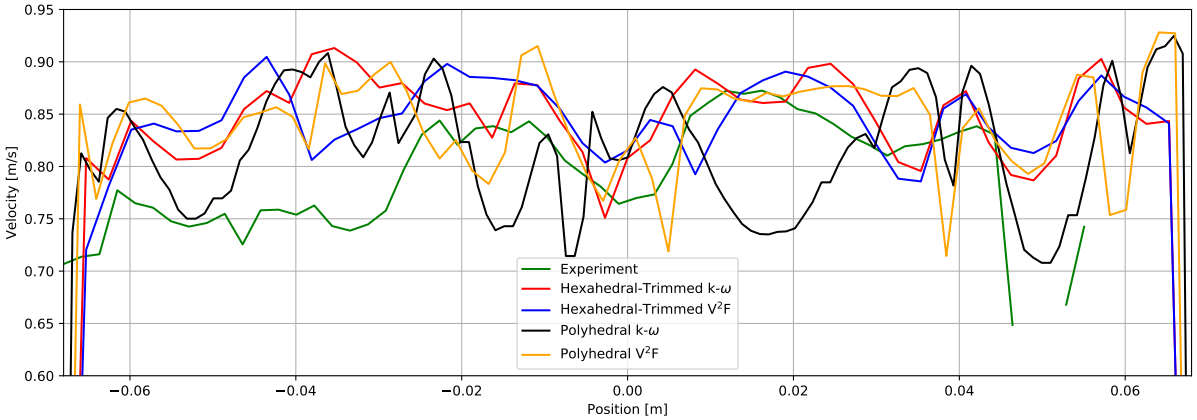

Figure A.45: k component of velocity along the probe line in a plane 250 mm from the tip of the spacer body.

350 mm measurements

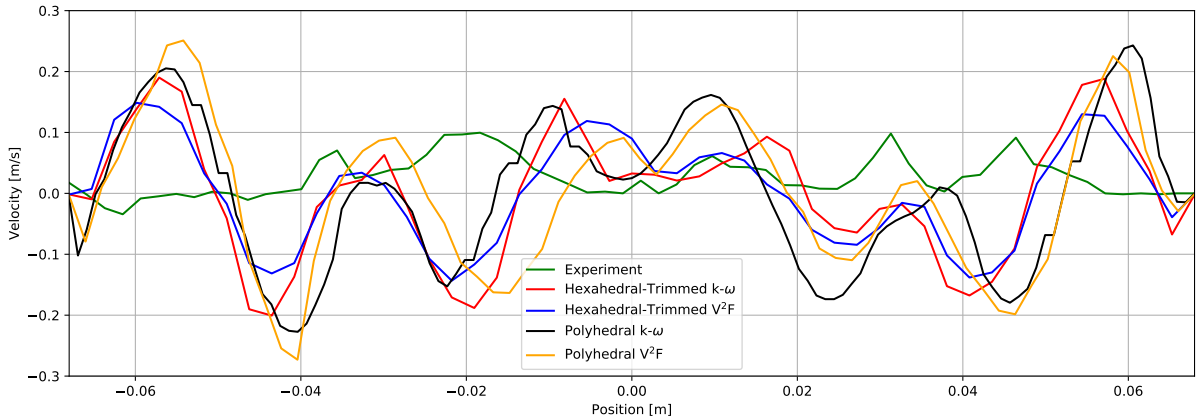

Figure A.46: i component of velocity along the probe line in a plane 350 mm from the tip of the spacer body.

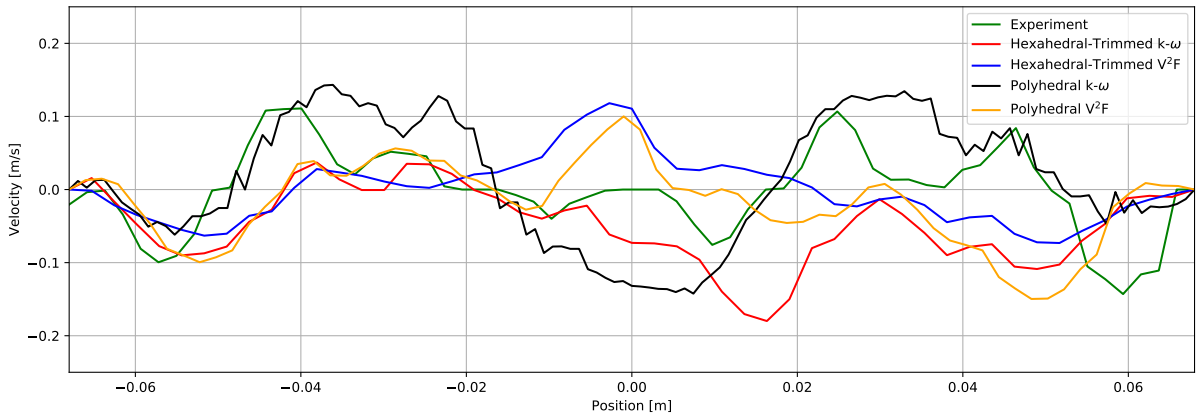

Figure A.47: j component of velocity along the probe line in a plane 350 mm from the tip of the spacer body.

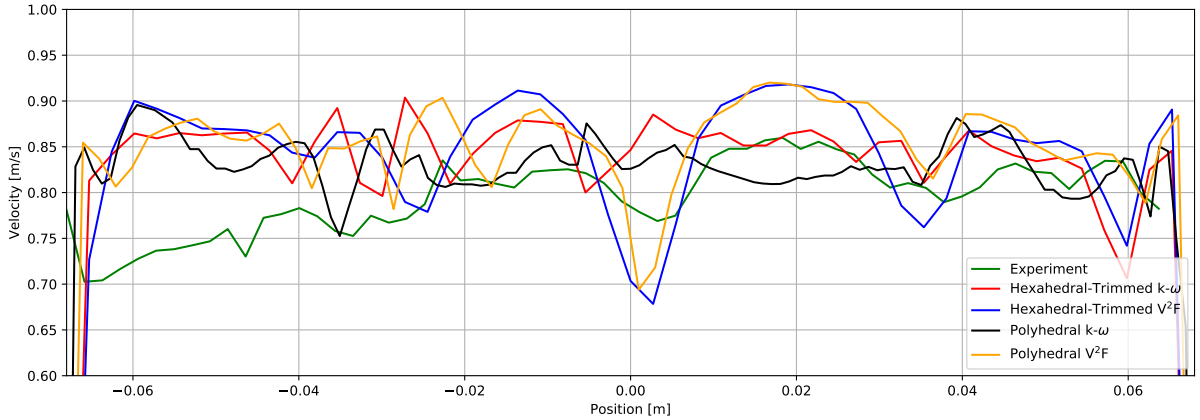

Figure A.48: k component of velocity along the probe line in a plane 350 mm from the tip of the spacer body.

450 mm measurements

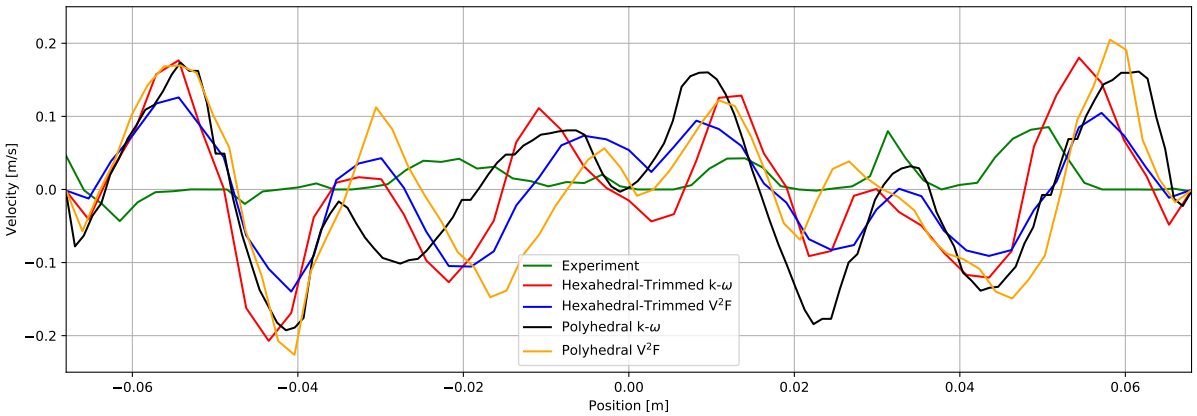

Figure A.49: i component of velocity along the probe line in a plane 450 mm from the tip of the spacer body.

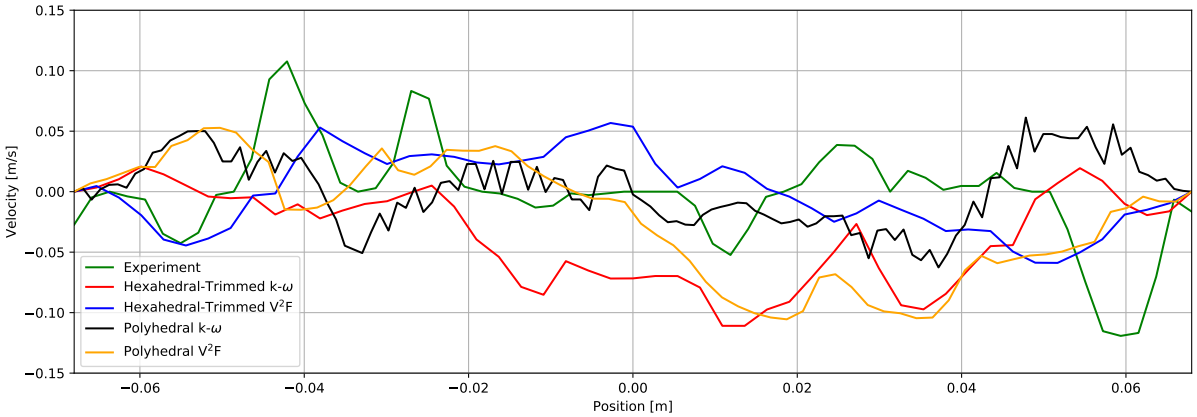

Figure A.50: j component of velocity along the probe line in a plane 450 mm from the tip of the spacer body.

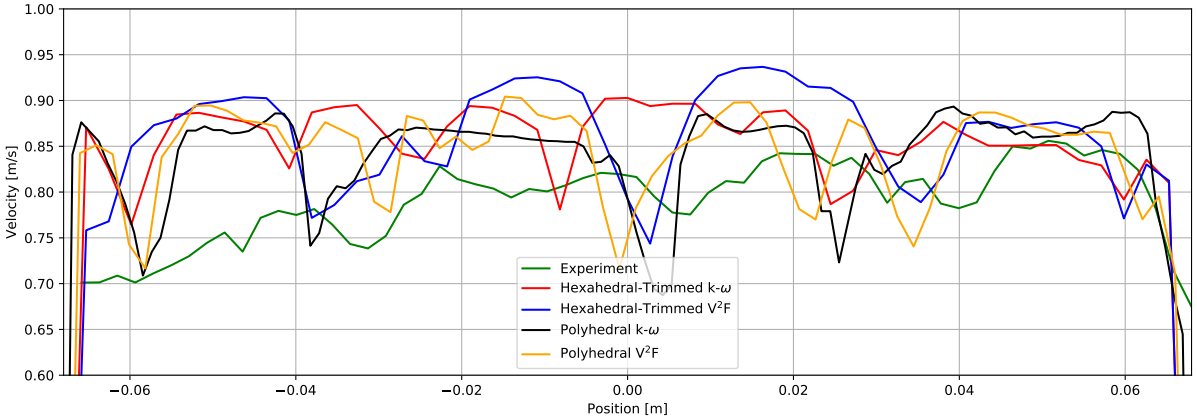

Figure A.51: k component of velocity along the probe line in a plane 450 mm from the tip of the spacer body.

550 mm measurements

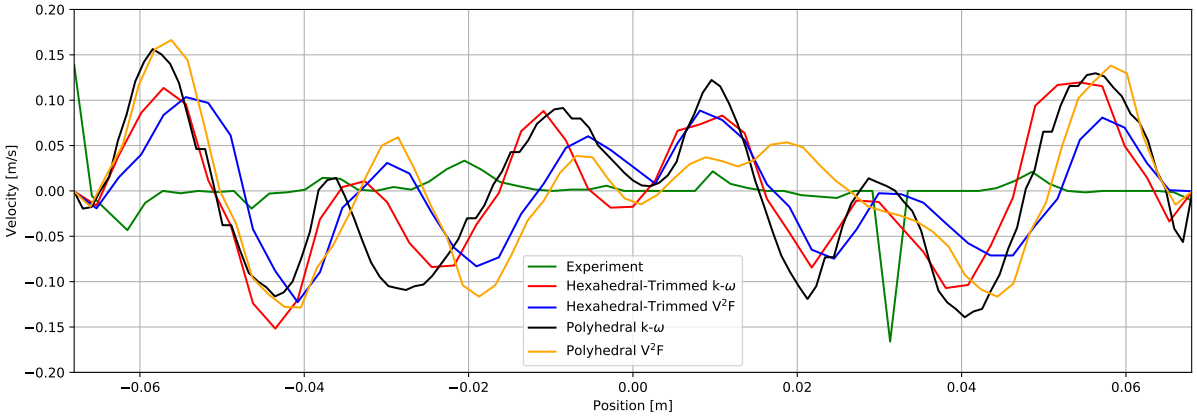

Figure A.52: i component of velocity along the probe line in a plane 550 mm from the tip of the spacer body.

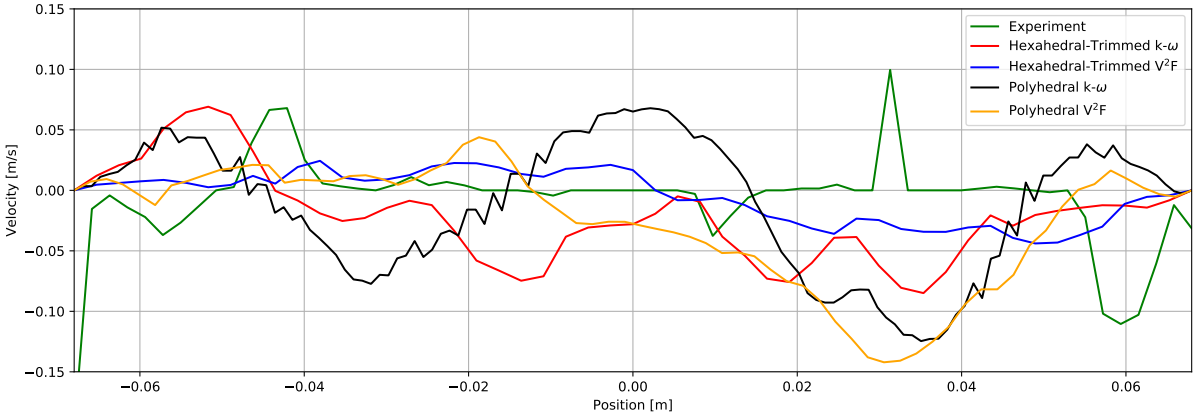

Figure A.53: j component of velocity along the probe line in a plane 550 mm from the tip of the spacer body.

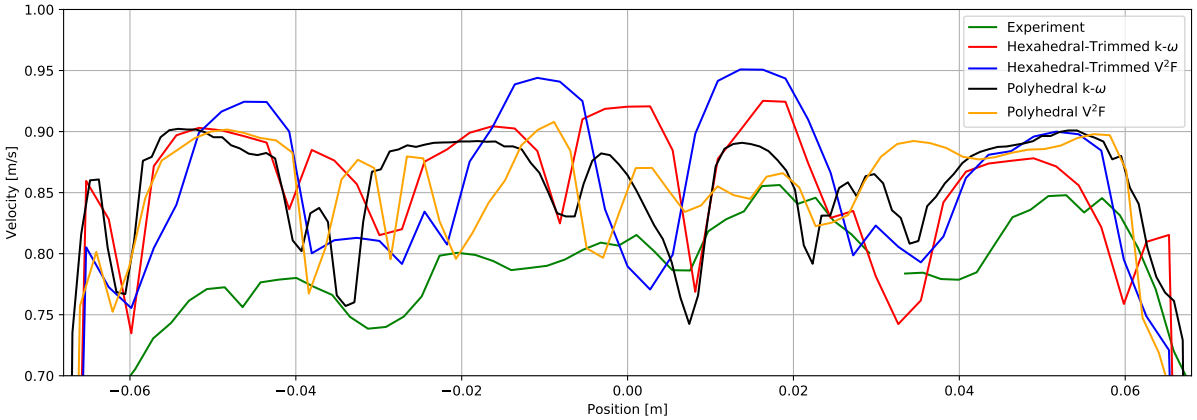

Figure A.54: k component of velocity along the probe line in a plane 550 mm from the tip of the spacer body.

References

[1] Conscious. Population of the world and its regions (in millions). https://commons.wikimedia.org/wiki/File:World_population_(UN).svg#filelinks, 2011. [Online; accessed June 26, 2018].

[2] Janssens-Maenhout G. Muntean M. Olivier, J.G.J. and J.A.H.W. Peters. Trends in global CO_2 emissions: 2016 Report. European Commission, Joint Research Centre (JRC), Directorate C - Energy, Transport and Climate. PBL Netherlands Environmental Assessment Agency, The Hague.

[3] Bundesamt für Energie BFE. Schweizerische Elektrizitätsstatistik 2016.

[4] Bundesamt für Energie BFE. Energy Strategy 2050 once the new energy act is in force.

[5] International Atomic Energy Agency. Operational & Long-Term Shutdown Reactors. https://pris.iaea.org/PRIS/WorldStatistics/OperationalReactorsByCountry.aspx, 2018. [Online; accessed June 13, 2018].

[6] International Atomic Energy Agency. Nuclear Share of Electricity Generation in 2017. https://pris.iaea.org/PRIS/WorldStatistics/NuclearShareofElectricityGeneration.aspx, 2018. [Online; accessed June 13, 2018].

[7] International Atomic Energy Agency. Contry statistics. https://pris.iaea.org/PRIS/CountryStatistics/CountryStatisticsLandingPage.aspx, 2018. [Online; accessed June 13, 2018].

[8] Ann Ronan Picture Library/Heritage Images. The Calder Hall nuclear power station, Cumbria, England, 1956. https://www.britannica.com/topic/Calder-Hall-reactor/images-videos. [Online; accessed June 14, 2018].

[9] Eidgenössisches Nuklearsicherheitsinspektorat ENSI. Gösgen Nuclear Power Plant. https://www.ensi.ch/en/topic/goesgen-nuclear-power-plant/. [Online; accessed June 14, 2018].

[10] International Atomic Energy Agency. Operational & Long-Term Shutdown Reactors. https://pris.iaea.org/PRIS/WorldStatistics/OperationalReactorsByType.aspx, 2018. [Online; accessed June 14, 2018].

[11] International Atomic Energy Agency. Operational Reactors by Age. https://pris.iaea.org/PRIS/WorldStatistics/OperationalByAge.aspx, 2018. [Online; accessed June 13, 2018].

[12] K. Rehme and G. Trippe. Pressure drop and velocity distribution in rod bundles with spacer grids. *Nuclear Engineering and Design*, 62(1):349 – 359, 1980.

[13] Yao, S. C. and Hochreiter, L. E. and Leech, W. J. Heat-Transfer Augmentation in Rod Bundles Near Grid Spacers. *Journal of Heat Transfer*, Feb 1982.

[14] Yue Fen Shen and Zi Dong Cao and Qing Gang Lu. An investigation of crossflow mixing effect caused by grid spacer with mixing blades in a rod bundle. *Nuclear Engineering and Design*, 125(2):111 – 119, 1991.

[15] Karouta, Z. and GU, Chun-Yuan and Schoelin, B. 3-D flow analyses for design of nuclear fuel spacer. September 1995.

[16] Yang, Sun Kyu and Chung, Moon Ki. Turbulent Flow Through Spacer Grids in Rod Bundles. *Journal of Basic Engineering*, Dec 1998.

[17] Langford, H.M. and Armfield, M.V. and Beasley, Donald and Conner, M.E. Particle image velocimetry of swirling flow in a subchannel of a rod bundle. 2:479–485, 01 2003.

[18] Holloway, Mary V. and Beasley, Donald E. and Conner, Michael E. Investigation of Swirling Flow in Rod Bundle Subchannels Using Computational Fluid Dynamics. *Volume 9: 23rd International Conference on Design Theory and Methodology; 16th Design for Manufacturing and the Life Cycle Conference — IDETC/CIE2011 — Proceedings — ASME DC*, Jan 2006.

[19] Mary V. Holloway and Donald E. Beasley and Michael E. Conner. Single-phase convective heat transfer in rod bundles. *Nuclear Engineering and Design*, 238(4):848 – 858, 2008.

[20] Elvis E. Dominguez-Ontiveros and Yassin A. Hassan. Non-intrusive experimental investigation of flow behavior inside a 5x5 rod bundle with spacer grids using PIV and MIR. *Nuclear Engineering and Design*, 239(5):888 – 898, 2009. Special Edition in honor of the retirement of Professor Neil Todreas.

[21] Diana Caraghiaur and Henryk Anglart and Wiktor Frid. Experimental investigation of turbulent flow through spacer grids in fuel rod bundles. *Nuclear Engineering and Design*, 239(10):2013 – 2021, 2009.

[22] Michael E. Conner and Emilio Baglietto and Abdelaziz M. Elmahdi. CFD methodology and validation for single-phase flow in PWR fuel assemblies. *Nuclear Engineering and Design*, 240(9):2088 – 2095, 2010. Experiments and CFD Code Applications to Nuclear Reactor Safety (XCFD4NRS).

[23] C.C. Liu and Y.M. Ferng. Numerically simulating the thermal–hydraulic characteristics within the fuel rod bundle using CFD methodology. *Nuclear Engineering and Design*, 240(10):3078 – 3086, 2010. 4th International Topical Meeting on High Temperature Reactor Technology (HTR 2008), with Regular Papers.

[24] Á. Horváth and B. Dressel. Numerical simulations of square arrayed rod bundles. *Nuclear Engineering and Design*, 247:168 – 182, 2012.

[25] Smith, B.L. and Song, C.H. and Chang, S.K. and Lee, J.R. and Kim, J.W. Report of the OECD/NEA-KAERI rod bundle CFD benchmark exercise. 5:4–124, 01 2013.

[26] Jae Ryong Lee and Jungwoo Kim and Chul-Hwa Song. Synthesis of the turbulent mixing in a rod bundle with vaned spacer grids based on the OECD-KAERI CFD benchmark exercise. *Nuclear Engineering and Design*, 279:3 – 18, 2014. SI : CFD4NRS-4.

[27] Xiaochang Li and Ye Gao. Methods of simulating large-scale rod bundle and application to a 17x17 fuel assembly with mixing vane spacer grid. *Nuclear Engineering and Design*, 267:10 – 22, 2014.

[28] Ulrich Bieder and François Falk and Gauthier Fauchet. CFD analysis of the flow in the near wake of a generic PWR mixing grid. *Annals of Nuclear Energy*, 82:169 – 178, 2015. Joint International Conference on Supercomputing in Nuclear Applications and Monte Carlo 2013, SNA + MC 2013. Pluri- and Trans-disciplinarity, Towards New Modeling and Numerical Simulation Paradigms.

[29] W.P Jones and B.E Launder. The prediction of laminarization with a two-equation model of turbulence. *International Journal of Heat and Mass Transfer*, 15(2):301 – 314, 1972.

[30] D.C. Wilcox. Multiscale model for turbulent flows. *AIAA 24th Aerospace Sciences Meeting*, 26(11):1311–1320, 1988.

[31] Heather L. McClusky, Mary V. Holloway, Timothy Conover, Donald Beasley, Michael E. Conner, and L David Smith. Mapping of the lateral flow field in typical subchannels of a support grid with vanes. 125, 11 2003.